UNIVERSIDAD
NACIONAL
DE COLOMBIA

On the structure of the lower crust to mantle transition beneath an accretionary inherited Andean margin, northwestern Andes

David Santiago Avellaneda Jiménez

Universidad Nacional de Colombia

Facultad de Minas, Departamento de Materiales

Medellín, Colombia

2022

On the structure of the lower crust to mantle transition beneath an accretionary inherited Andean margin, northwestern Andes

David Santiago Avellaneda Jiménez

Thesis or research work submitted as a partial requirement for the degree of:

Ph.D. in Engineering - Materials Science and Technology

Advisor:

Ph.D. Gaspar Monsalve Mejía

Field of research:

Tectonophysics

Universidad Nacional de Colombia

Facultad de Minas, Departamento de Materiales

Medellín, Colombia

2022

Dedicatory

To my parents for their support and inspiration, and to my closest colleagues for the constant discussion that keeps me motivated in doing research.

Declaración de obra original

Yo declaro lo siguiente:

He leído el Acuerdo 035 de 2003 del Consejo Académico de la Universidad Nacional. «Reglamento sobre propiedad intelectual» y la Normatividad Nacional relacionada al respeto de los derechos de autor. Esta disertación representa mi trabajo original, excepto donde he reconocido las ideas, las palabras, o materiales de otros autores.

Cuando se han presentado ideas o palabras de otros autores en esta disertación, he realizado su respectivo reconocimiento aplicando correctamente los esquemas de citas y referencias bibliográficas en el estilo requerido.

He obtenido el permiso del autor o editor para incluir cualquier material con derechos de autor (por ejemplo, tablas, figuras, instrumentos de encuesta o grandes porciones de texto).

Por último, he sometido esta disertación a la herramienta de integridad académica, definida por la universidad.

David Santiago Avellaneda Jiménez___________

Nombre

21/05/2022

Fecha

Acknowledgments

Thanks to my advisor Gaspar M., and to those colleagues with whom the daily discussion keeps me improving and thinking about new research goals. Special thanks to Santiago L., Gustavo P., Lara W., Carlos V., Jhon J. S., Thorsten B., Angela G., Rocío B., and Steve R., for the fruitful discussions about the applied methods and interpretations, and suggestions on the submitted manuscripts.

Abstract

On the structure of the lower crust to mantle transition beneath an accretionary inherited Andean margin, northwestern Andes

The crust-mantle transition beneath the northwestern Andes is expected to be complex given its accretionary tectonic history. Considering that research on this matter remains scarce, especially in the Colombian region, this thesis presents new insights into the structure and nature of the crust-mantle transition in several parts of the orogen. Four chapters are presented, discussing: (1) variations in Moho depth along the orogen using inversion of gravity data; (2) latitudinal heterogeneity and anisotropy in the uppermost mantle beneath the modern arc using Pn and Sn wave speed estimates, and thermo-compositional modeling; (3) the nature of the arc root beneath the modern arc by means of a receiver function analysis; and (4) intra-continental deformation beneath the Eastern Cordillera plateau from a joint inversion of arrival times of local earthquakes and gravity data.

Integrated results suggest three main features associated with a thickened crust: along the northwestern foreland region (influenced by the adjacent thickened Eastern Cordillera), along the axis of the Eastern Cordillera (related to its shortening history and magmatic additions), and in the southern part of the modern arc, in the Andes of southern Colombia and northern Ecuador (likely a combined result of mafic addition to the base of the crust, foundering tectonics, and lateral displacement of the lower crust).

Investigations on the upper mantle beneath the modern arc suggest a well-developed anisotropy, showing a latitudinal dissimilarity in wave speeds and temperature. The northern part (north of 4°N; <75 km wide arc) is seismically slower, and has a higher degree of anisotropy, suggesting warmer conditions. The southern part (south of 2°N; >120 km wide arc) is faster, less anisotropic, and consistent with a colder state. Beneath the volcanic gap region (2°-4°N), seismic speeds are similar to those in the north, yet a colder thermal state is suggested. The controlling factor of the anisotropy is the preferred orientation of olivine and pyroxene. Latitudinal anisotropy and temperature dissimilarities are likely influenced by the Caldas tear to the north, prompting hot mantle influx, and the Carnegie ridge interaction to the south, prompting shallower subduction.

Additional investigations on the arc domain, using the teleseismic receiver function technique, which looks for P to S phase conversions, indicate that the crustal root beneath the arc is characterized by high velocities and a latitudinally variable thickness, which coupled with documented xenoliths supports an arclogite nature. This high-velocity and high-density arc root suggest an offset between the seismic Moho and the crust-mantle boundary of around 8.5-14 km.

Finally, beneath the Eastern Cordillera plateau, a well-imaged anomaly is identified at depths of 40-60 km beneath the western flank of the plateau, at a latitude of ~5.7°N. The slow velocity anomaly is interpreted as crustal materials eastwardly underthrusting beneath the western flank. This process is thought to be prompting the abrupt change in topography between the adjacent low-elevated basin and the orogenic plateau.

This thesis shows how the crust-mantle transition along the northwestern Andes follows the idea that a heterogenous Moho vicinity is the rule rather than the exception for Andean-type orogens.

Keywords: Northern Andes; crustal thickening; mantle anisotropy; arclogite arc-root; intra-continental underthrusting; multi-technique geophysics.

Resumen

Sobre la estructura de la transición corteza baja al manto en un margen andino con herencia de acreción, Andes noroccidentales

La transición corteza-manto bajo los Andes noroccidentales se espera que sea compleja, dada su historia tectónica que involucra la acreción de bloques. Teniendo en cuenta que la investigación sobre este tema sigue siendo escasa, especialmente en la región colombiana, esta tesis presenta nuevos conocimientos sobre la estructura y la naturaleza de la transición corteza-manto en varias partes del orógeno. Se presentan cuatro capítulos, en los que se analizan: (1) las variaciones en la profundidad del Moho a lo largo del orógeno mediante la inversión de datos de gravedad; (2) la heterogeneidad latitudinal en el manto superior bajo el arco moderno mediante estimaciones de velocidad de las ondas Pn y Sn, anisotropía y modelamiento termo-composicional; (3) la naturaleza de la raíz del arco debajo el arco moderno mediante el análisis de la función receptora; y (4) la deformación intra-continental bajo la meseta de la Cordillera Oriental a partir de la inversión conjunta de tiempos de llegada de terremotos locales y datos de gravedad.

Los resultados integrados sugieren tres rasgos principales de engrosamiento de la corteza a lo largo del orógeno: en la región noroccidental del antepaís (influenciada por la adyacente Cordillera Oriental con corteza engrosada), a lo largo del eje de la Cordillera Oriental (relacionado con su historia de acortamiento y adición magmática), y en la parte sur del arco moderno, en los Andes al sur de Colombia y norte de Ecuador (probablemente el resultado combinado de adición magmática a la base de la corteza, la tectónica de hundimiento/delaminación, y del desplazamiento lateral de la corteza inferior).

Investigaciones en el manto superior bajo el arco moderno sugiere que es anisotrópico, mostrando una disimilitud latitudinal en las velocidades de ondas sísmicas y la temperatura. La parte norte (al norte de 4°N; arco <75 km de ancho) es sísmicamente más lenta, tiene una mayor anisotropía y sugiere condiciones más cálidas. La parte sur (al sur de 2°N; arco >120 km de ancho) es más rápida, menos anisotrópica y sugiere condiciones más frías. Por debajo de la región con ausencia magmática (2°-4°N), las velocidades sísmicas son similares a las del norte, pero se sugiere un estado térmico más frío. El factor que controla la anisotropía es la orientación preferente del olivino y el piroxeno. La anisotropía latitudinal y las disimilitudes de temperatura están probablemente influenciadas por el desgarro litosférico de Caldas al norte, que provoca la entrada de manto caliente, y la interacción de la dorsal de Carnegie al sur, que permite una subducción menos profunda.

Adicionalmente, investigaciones sobre la región del arco, utilizando la técnica de función de receptora telesísmica, que busca conversiones de fase P a S, sugiere que la raíz cortical bajo el arco moderno muestra altas velocidades con un grosor variable en latitud, que, junto con xenolitos documentados, apoyan una naturaleza arclogítica. Esta capa de alta velocidad y densidad sugiere un desfase entre el Moho sísmico y el límite corteza-manto de unos 8.5-14 km.

Por último, debajo de la meseta de la Cordillera Oriental, se identifica una anomalía bien constreñida a profundidades de 40-60 km bajo el flanco occidental de la meseta, a una latitud de ~5.7°N. La anomalía de velocidad lenta se interpreta como una inyección de materiales corticales hacia el este por debajo del flanco occidental. Este proceso provoca un cambio abrupto en la topografía entre la cuenca adyacente de baja elevación y la meseta orogénica.

Esta tesis muestra cómo la transición corteza-manto a lo largo de los Andes noroccidentales es una región heterogénea y compleja en orógenos de tipo andino.

Palabras claves: Andes del Norte; engrosamiento cortical; anisotropía del manto; raíz cortical arclogítica; deformación intra-continental; geofísica multitécnica.

Table of contents

Pag.

Figures

Pag.

Tables

Pág.

1. Introduction, research strategy, and objectives

1.1 Introduction

Understanding the structure of the lower crust to mantle transition (Moho vicinity), in terms of its physical properties and origin, is crucial for the improvement of our knowledge about the formation, deformation, and destruction of the lithosphere (Cook et al., 2010; Lee, 2014; Wang et al., 2013). At these depths, an inherent complexity is linked to the petrologic contrast between crustal and mantle materials; to the lateral dissimilarities in composition, density, and temperature across this boundary; to the existence of tectonic or magmatic underplating processes affecting the Moho vicinity; to the dynamics of deep underthrusting and lower crustal flow affecting majorly the lowermost crust; and to the delaminating or foundering tectonics; all together affecting the isostatic equilibrium as well as the rheological response of the overlying crust and the underlying uppermost mantle (Aitken et al., 2013; Beck and Zandt, 2002; Clark et al., 2005; Furlong and Fountain, 1986; Lee, 2014; Riesner et al., 2018a; Shi et al., 2020; Sobolev et al., 2006; Spada et al., 2013; Thybo and Artemieva, 2013; Vietor and Oncken, 2005; Xuan et al., 2020).

The complexity along the Moho vicinity can be further augmented, under a scenario of an accretionary inherited active margin, such as the northwestern Andes (study region). The latter is due to its evolution involving multiple tectonic processes that have occurred especially during the Cenozoic. These major processes include: (1) the installation of different magmatic arcs during the Paleogene, currently juxtaposed by accretionary tectonics (Cardona et al., 2018; Montes et al., 2019); (2) the development of an Oligo-Miocene to recent magmatic arc installed above an accretionary orogen (Marín-Cerón et al., 2019; Monsalve-Bustamante, 2020); (3) the subduction zone migration of two different oceanic plates (Caribbean and Farallon) during the Cretaceous to Paleogene, and the subsequent splitting of the Farallon plate into Nazca and Cocos around 23 Ma (Lonsdale, 2005); (4) the collision of the Panama-Chocó arc and the consequent lithospheric deformation, which initiated during the early-middle Miocene (León et al., 2018; Montes et al., 2019); (5) the collision of the Carnegie ridge since Miocene times (Gutscher et al., 1999); and (6) the establishment of a complex convergence structure, with two subducting plates: the Caribbean plate to the north and the Nazca plate to the west. These two slabs show variations in the subduction angle along-strike, contain lithospheric tears, and possibly overlap proposing the Nazca slab to be underneath the Caribbean plate (Chiarabba et al., 2015; Cortés and Angelier, 2005; Idárraga-García et al., 2016; Sun et al., 2022; Syracuse et al., 2016; Vargas, 2020; Vargas and Mann, 2013; Wagner et al., 2017).

Moreover, as has been shown by receiver functions and petrologic constraints, the presence in multiple regions below the cordilleran belt of, high-density crustal materials composing the lowermost crust, crustal thicknesses above 55 km in multiple regions, high Vp/Vs ratios spatially corresponding with volcanic centers, and fast seismic velocities at the crust-mantle transition, are likely the expression of mafic underplating and foundering tectonics within the Colombian Andes (Bloch et al., 2017; Monsalve et al., 2019; Poveda et al., 2015). Such mechanisms are expected to drive important modifications in the mantle structure, and across/along the Moho (Beck and Zandt, 2002; Lee, 2014; Thybo and Artemieva, 2013; Wang et al., 2013). This makes the study of the Moho vicinity a topic of major interest to improve our understanding of the evolution and the dynamic processes shaping the northwestern Andes.

Considering the previously mentioned tectonic evolution and the current configuration of the study region, assuming a crust-mantle transition as being homogeneous beneath the northwestern Andes, seems to be an incorrect perception (e.g. Cook et al., 2010). In consequence, the Moho vicinity must be investigated from different approaches to improve our comprehension of the spatial distribution of the Moho depth and the nature of the crust-mantle transition. This knowledge will allow better interpretations of the relationship between the characteristics of the Moho vicinity and the modern and ancient tectonics. To my current state of knowledge, important discussions within the target region, about the nature of the upper mantle and the lower crust have taken place independently (Bernal-Olaya et al., 2015; Bloch et al., 2017; Meissnar et al., 1976; Monsalve et al., 2019; Porritt et al., 2014; Poveda et al., 2015; Vargas et al., 2019; Weber et al., 2002; among others). Thereby, the nature of the crust-mantle transition beneath the northwestern Andes, remains a poorly explored field of research, and thus, it becomes a topic with major potential to be applied in this area. Therefore, the main interest and target of this thesis is the Moho vicinity beneath different tectonic settings along the northwestern Andes.

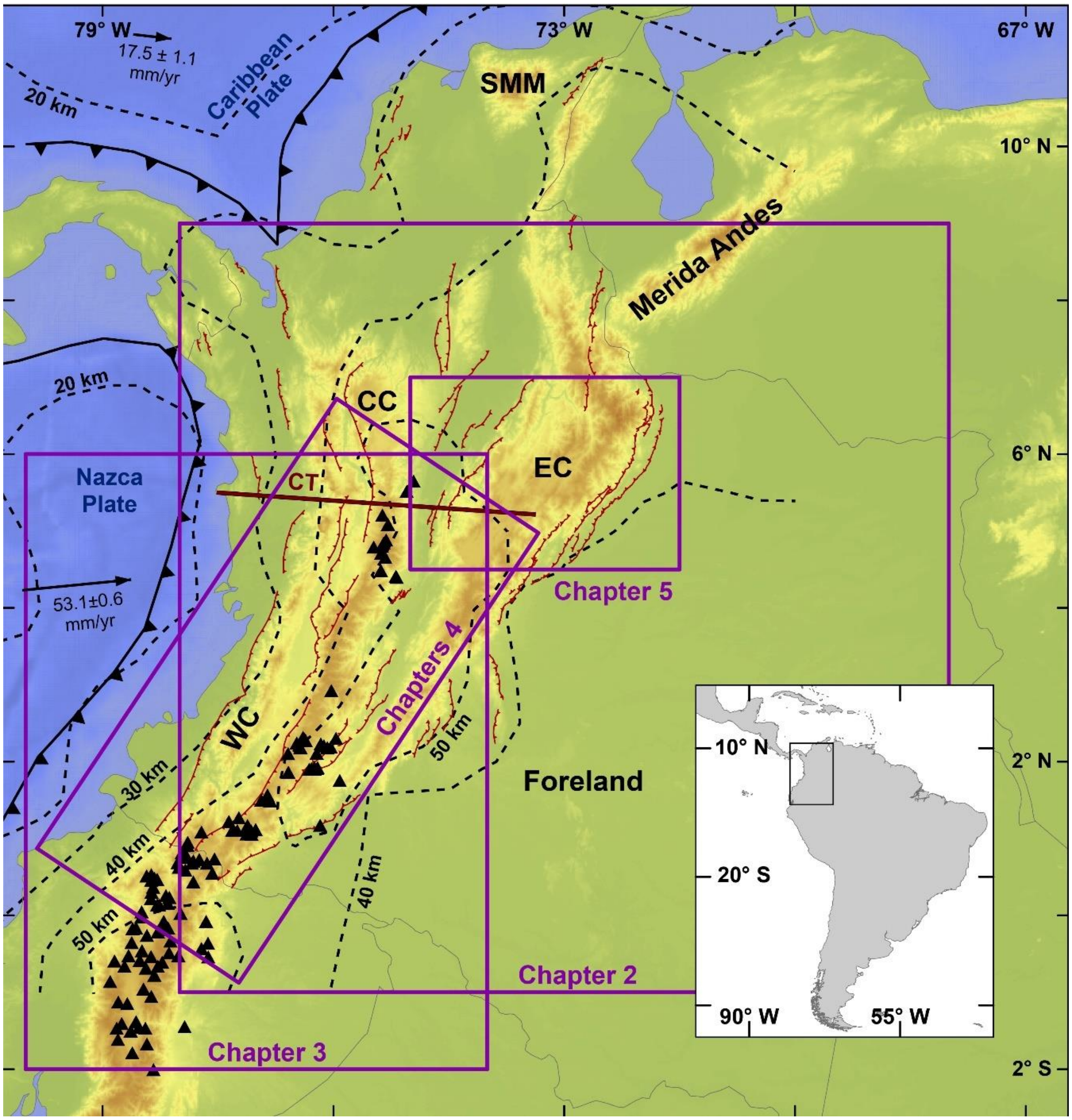

Figure 1-1. Map view of the northwestern Andes with the main tectonic features, and the studied areas discussed in the different chapters of this thesis (purple rectangles). Modern volcanic centers are represented by black triangles (note the latitudinal variation in on-surface volcanism); red lines are active thrusting faults (Veloza et al., 2012), and, dashed black lines are crustal thickness contours based on receiver functions (Poveda et al., 2018). The Caldas tear (CT) is represented by the dark red line after Vargas (2020). The volcanic gap in the central portion (~2°-4°N) shows a reduction in surface volcanism for around 265 km along the arc. See Monsalve-Bustamante (2020) for some spatial considerations about this volcanic gap. WC, CC, EC, and SMM stand for Western, Central, and Eastern

Cordilleras, and Santa Marta Massif, respectively. Convergence rate of the Caribbean and Nazca plate with respect to stable South America after Mora-Páez et al. (2019).

1.2 Research strategy and objectives

Understanding the tectonic evolution and geodynamic setting of the northwestern Andes could be overwhelming at the beginning, because of the different parameters that must be considered when addressing the deep crust and crust-mantle transition. For this reason, I will focus on two main general questions about the Moho vicinity: (1) the spatial distribution of the Moho depth, and (2) the seismic structure (nature) of the deep crust and crust-mantle transition beneath specific areas of interest (see Figure 1-1).

My strategy of research begins with first-order observations using a simple approach for the Moho depth distribution at a broad scale (chapter 2, Figure 1-1), from which the identification of specific areas of interest, will result in detailed research and application of robust approaches to better depict the complexity in the deep crust and its transition to the underlying mantle (chapters 3 to 5, Figure 1-1). This thesis not only aims to provide several geophysical observations using multiple techniques, but also discusses and integrates the accomplished results with previous and available geophysical constraints, and complementary petrologic and on-surface geologic information.

In that sense, a good starting point when researching the crust-mantle boundary, is to depict and understand variations in the Moho depth along the orogen (objective of chapter 2). To overcome the limitation of poor coverage and distribution of seismic stations, I applied the inversion of gravity data, which has been considered a complement and widely used technique showing good correlations with seismic-based estimations (e.g. Aitken et al., 2013; Prasanna et al., 2013; Steffen et al., 2017; Uieda and Barbosa, 2017; van der Meijde et al., 2013; among others). The main advantage of using gravity lies in its wider coverage and data accessibility, which makes it a valuable approach to constraining the structure of the lower crust and uppermost mantle in regions with limited coverage of seismic monitoring. Thus, in chapter 2 the inversion of gravity data is discussed, giving insights into the Moho topography beneath the northwestern Andes.

Using the results derived from such gravity inversion and the respective analysis of the Moho depth distribution along the study region, two main areas of interest were selected to further investigate the deep crust and crust-mantle transition beneath the Northern Andes: the modern magmatic arc domain, and the central-northern Eastern Cordillera in Colombia.

Chapters 3 and 4 focus on the modern magmatic arc domain (Figure 1-1). In this regard, the mantle wedge beneath the magmatic arc is expected to be latitudinally heterogeneous, as suggested by recovered xenoliths (Bloch et al., 2017; Rodriguez-Vargas et al., 2005; Weber, 1998; Weber et al., 2002), seismic tomography (Chiarabba et al., 2015; Syracuse et al., 2016; Vargas et al., 2007), receiver functions (Poveda et al., 2015), and thermal constraints (Vargas et al., 2019). Therefore, in chapter 3, the main objective is to elucidate the seismic structure dissimilarity and the latitudinal thermo-compositional differences in the uppermost mantle. This is addressed through Pn and Sn inter-station wave speed estimates, and a combination of inverse (LSQR algorithm) and forward modeling (phase equilibria) approaches to perform a thermo-compositional analysis.

In addition to the uppermost mantle heterogeneity beneath the modern arc, the crust-mantle transition along this part of the orogen is of great importance since it is the only known active segment along the Andes that contains xenoliths described as arclogites (Ducea et al., 2021b). They are located at the base of continental arcs, and play an important role in defining the crustal structure, since their seismic properties resemble those of the underlying mantle (Ducea et al., 2021b; Erdman et al., 2016). In chapter 4, the main goal is to address the nature of the arc root and its transition to the uppermost mantle beneath the modern arc. The seismic structure is investigated through a teleseismic receiver function analysis conducted at seismic stations on top of the main active volcanoes.

Finally, the northern part of the Eastern Cordillera represents a wide (~200 km) high-elevated (>2.5 km) subduction-related asymmetric plateau (Mora et al., 2015, 2008; Siravo et al., 2021), which is subjected to crustal thickening due to shortening (Bayona et al., 2008; Mora et al., 2013, 2008; Siravo et al., 2018; Tesón et al., 2013; among others) and magmatic underplating (Monsalve et al., 2019). These two processes allow the deep crust to host high-velocity and high-density materials that prompt lower crustal flow, delamination, or foundering tectonics (Beck and Zandt, 2002; Guerri et al., 2015; Lee, 2014; McKenzie and Jackson, 2002; Thybo and Artemieva, 2013; Wang et al., 2013). The main objective of chapter 5, is to image the deep crust and crust-mantle structure beneath the Eastern Cordillera plateau, to evaluate the possibility of intra-continental deformation of the lower crust. The structure of the deep crust and its transition to the underlying mantle is investigated by means of a joint tomographic inversion of arrival times using local earthquakes and gravity data beneath the northern Eastern Cordillera plateau (Figure 1-1).

2. Insights into Moho depth beneath the northwestern Andean region from gravity data inversion

2.1 Summary

The complex Moho topography beneath the northwestern Andes is the result of multiple geodynamic processes during the Cenozoic. To contribute to our understanding of the Moho depth distribution beneath this region, I inverted gravity data from two widely used satellite-derived datasets (EGM2008, EIGEN-6C4) and one regional airborne Bouguer gravity anomaly map (ANH2010). Their inversion allowed choosing the ANH2010, based on lower residual gravity and a higher agreement with seismic estimations, as the most suitable dataset to gain insights into the Moho depth beneath the northwestern Andes and its relationship with previously identified tectonic features. The inverted Moho argues for a ~40 to ~50 km depth beneath the Central and Eastern cordilleras, reaching depths beyond 50 km below the Eastern Cordillera, and shallower depths between ~30-40 km mainly along the foreland region to the east, the Western Cordillera, and the coastal plains. Three main thickened crust features of regional extent were identified: (1) a deep Moho expression with a crustal thickness greater than 40 km in the northwesternmost foreland region, which is considered a direct consequence of the adjacent thickened Eastern Cordillera involving the fold and thrust deformation migration from the range towards the foreland, and the flexural deformation proposed for the eastern foothills; (2) a regional deep Moho expression (~50-60 km) along the axis of the Eastern Cordillera, related to its shortening history including multiple phases of Cenozoic thick-skinned deformation and magmatic underplating; and (3) a Moho deeper than 60 km in a southern latitude (1°S-1°N) beneath the modern magmatic arc, whose interpretation is more complex, likely a combined result of mafic addition to the

base of the crust, foundering tectonics, and lateral displacement of the lower crust prompted by the subducting Carnegie ridge.

2.2 Introduction

The Moho discontinuity is defined as the rheological boundary where seismic velocity sharply increases due to the transition from crustal to mantle materials (Mooney, 2021). This boundary can be complex in terms of depth and geometry along active orogens since it is subjected to physical and chemical processes promoted by the interaction between the base of the crust and the underlying uppermost mantle (Karabulut et al., 2013; Kay et al., 2014; Larkin et al., 1997; Schreiber et al., 2010). In subduction-related orogens, such as the northwestern Andean region, the complexity of the crust-mantle transition depends on its petrologic contrast, lateral compositional and thermal dissimilarity, underplating and/or delaminating processes, and lower crustal flow, affecting the isostatic equilibrium as well as the rheological response of the overlying crust (Aitken et al., 2013; Beck and Zandt, 2002; Shi et al., 2020; Spada et al., 2013; Xuan et al., 2020).

In the case of the northwestern Andes, a complex Moho topography is expected because of multiple tectonic processes that have occurred especially during the Cenozoic. They include the installation of different magmatic arcs during the Paleogene currently juxtaposed by accretionary tectonics (Cardona et al., 2018; Montes et al., 2019), the development of an Oligo-Miocene to recent times magmatic arc installed above an accretionary orogen (Marín-Cerón et al., 2019; Monsalve-Bustamante, 2020), the subduction zone migration of two different oceanic plates (Caribbean and Farallon) during the Cretaceous-Paleogene, and the subsequent fission of the Farallon plate into Nazca and Cocos plate around 23 Ma (Lonsdale, 2005), the collision of the Panama-Chocó arc during the early-middle Miocene (León et al., 2018; Montes et al., 2019), and the subsequent establishment of a subducting Caribbean plate to the north and Nazca plate to the west of the northwestern Andes, with changes in the subduction angle and slab tearing along-strike within those slabs (Chiarabba et al., 2015; Syracuse et al., 2016; Vargas, 2020; Wagner et al., 2017). Moreover, receiver functions and petrologic constraints have suggested the presence, in multiple regions below the cordilleran belt, of crustal thicknesses above 55 km, high Vp/Vs ratios, and fast seismic velocities at the crust-mantle transition, which are interpreted as reflecting mafic underplating and foundering tectonics (Bloch et al., 2017;

Monsalve et al., 2019; Poveda et al., 2015). Such mechanisms are expected to drive important modifications in the mantle structure and along the Moho interface (Beck and Zandt, 2002; Thybo and Artemieva, 2013).

In consequence, Moho topography beneath the northwestern Andes must be investigated from different approaches to improve our understanding of its spatial distribution and the relationship with modern and ancient tectonics. In this sense, the most reliable approach for estimating Moho depth is considered to be seismic imaging, which permits the determination of broad and fine structures along this discontinuity (Mooney, 2021). Nevertheless, the resolution and accuracy of such an approach strongly depend on the coverage and distribution of seismic stations. To overcome this limitation, inversion of gravity data has been widely applied to complement the study of the Moho topography, showing good correlations with seismic-based estimations (Aitken et al., 2013; Prasanna et al., 2013; Sahoo and Pal, 2021; van der Meijde et al., 2013). The advantage of using gravity lies in its wider coverage and data accessibility, which makes it a valuable approach to constraining the structure of the lower crust and uppermost mantle in regions with limited coverage of seismic monitoring, such as the study area. Yet, because different gravity datasets with contrasting spatial resolution and coverage are available, a comparison between obtained inversions must be done before any interpretation is proposed. Previous attempts in this regard have been made on a continental scale (van der Meijde et al., 2013; Uieda and Barbosa, 2017) overlooking particularities of the northwestern Andes because of different scopes.

In this chapter, I contribute to the understanding of the Moho depth beneath the northwestern Andes by initially inverting gravity data from two widely used satellite-derived datasets, i.e. EGM2008 (Pavlis et al., 2012) and EIGEN-6C4 (Förste et al., 2014; Ince et al., 2019), and one regional airborne Bouguer gravity anomaly map built by the National Hydrocarbon Agency of Colombia (Graterol and Vargas, 2010). I followed the computation of a 3D geometry of an interface with a crust-mantle density contrast, through the application of the Parker-Oldenburg iterative approach (Gómez-Ortiz and Agarwal, 2005). I examine their differences in terms of convergence of the applied algorithm, and their discrepancies with respect to global Moho models, i.e. CRUST1.0 (Laske et al., 2013) and GEMMA (Reguzzoni and Sampietro, 2015), and their consistency with seismic constraints. By using an appropriate combination of parameters, after choosing the most suitable dataset based on lower residual gravity and a higher agreement with seismic estimations, insights into Moho depth are discussed focusing on particular regional-extent expressions and their spatial correspondence with identified tectonic features.

2.3 Tectonic setting

The Colombian Andes include three main mountain ranges named Eastern (EC), Central (CC), and Western Cordilleras (WC); the Magdalena Valley lies between EC and CC, and the Cauca-Patía Valley between CC and WC (Figure 2-1). The foreland region lies to the east of the EC bounded by the dextral-reverse East Andean fault zone (Kellogg et al. 2019), composed of several individual thrusting fault systems (Veloza et al., 2012).

Slabs from at least two oceanic plates subduct beneath the Colombian Andes, the Caribbean plate to the north, beneath the Caribbean plains (CP in Figure 2-1), and the Nazca plate to the west, beneath the Pacific plains and WC (Figure 2-1). At 5°-5.5°N the so-called Caldas tear separates a flat-slab setting to the northwest, characterized by the absence of active volcanism, from normal/steep subduction to the south, where the modern magmatic arc is located (Chiarabba et al., 2015; Syracuse et al., 2016; Vargas, 2020; Vargas and Mann, 2013; Wagner et al., 2017).

Lithospheric thickness estimates of ~103 km within the foreland region and ~100-110 km along the Colombian Andes have been obtained from receiver functions, with no major latitudinal variations (Blanco et al., 2017). In terms of crustal thickness, seismic constraints suggest a 22-48 km-thick crust at the eastern foothills and the foreland region, and 20-40 km at the WC (Monsalve et al., 2013; Poveda et al., 2015). A crust thicker than 50 km is suggested beneath the central-northern region of the CC and EC (4°-6°N), and along the southern CC (1°-3°N; Poveda et al., 2015). Below the central EC, the identification of a high seismic velocity layer at the base of the crust has been interpreted as magmatic underplating, which seems to contribute to crustal thickening in this part of the orogen (Monsalve et al., 2019).

In terms of gravity data and modeling, along the CC, EC, and the foreland region, Bouguer gravity anomalies correlate well with a continental-affinity crust (Case et al., 1971; Gómez-García et al., 2021; Kellogg et al., 2019; Vargas and Mann, 2013). The WC is characterized by higher gravity anomalies (e.g. Case et al., 1971) due to the nature of the basement (oceanic crust) mostly associated with fragments of the Caribbean plate (Kerr et al., 1997) accreted during the latest Cretaceous to Paleogene (León et al., 2021; Pardo-Trujillo et al., 2020; Villagómez and Spikings, 2013). Beneath the Caribbean plains, integrated geological, seismic and gravity data suggest the presence of accreted mafic materials related to the Caribbean plate as well (Bernal-Olaya et al., 2015; Cardona et al., 2012; Vargas and Mann, 2013).

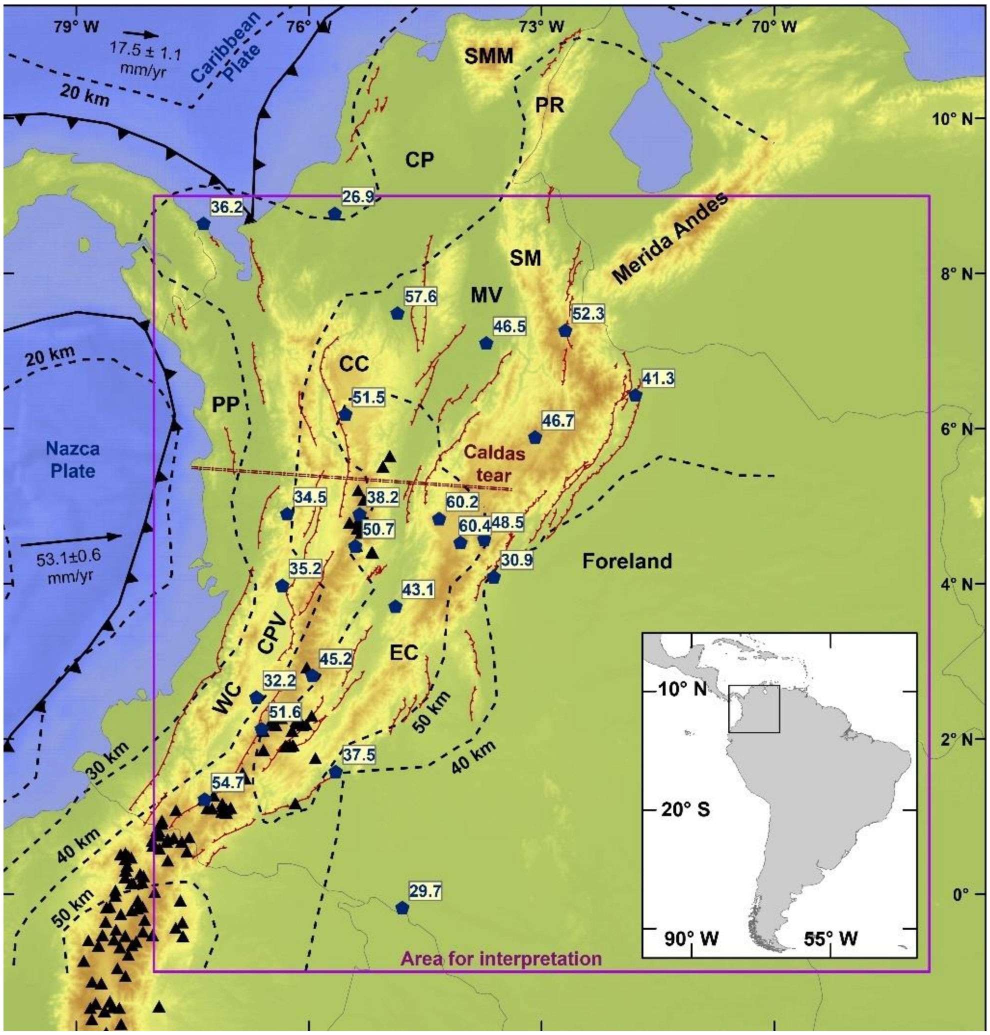

Figure 2-1. Map of the Colombian Andes showing active thrust faults (Veloza et al., 2012), active volcanism (triangles), and the area for interpretation of the gravity inversion. Pentagons depict mean Moho depth (in km) at individual stations from receiver functions (Poveda et al., 2015), whereas dashed lines are crustal thickness contours (Poveda et al., 2018). Geomorphic features are Magdalena Valley (MV), Cauca-Patía Valley (CPV), Caribbean plains (CP), Santa Marta Massif (SMM), Santander Massif (SM), and Pacific plains (PP). Oceanic plate convergence vectors and rates are relative to stable South

America (Mora-Páez et al., 2019). The location of the Caldas tear is taken from Vargas (2020).

2.4 Methodology and analysis

2.4.1 Inversion code and gravity datasets

2.4.1.1 Gravity Moho inversion

To estimate Moho topography by means of gravity data inversion, I initially assume isostatic equilibrium and applied the 3DINVER.M code implemented by Gómez-Ortiz and Agarwal (2005). I consider isostatic equilibrium to be a good assumption since only positive residual topography has been considered for the northern Eastern Cordillera (Yarce et al., 2014; Siravo et al., 2018) with an amount of excess topography that I will show, is within the uncertainty of the applied method. The inversion code is based on the original equation of Parker (1973), who derived the Fourier transform of the gravitational field for an undulated interface in between two layers with different densities. A relative height of the undulating surface (Moho) is calculated with respect to a reference average depth (z_0) and a constant density contrast ($\rho = \rho_{ml} - \rho_c$) across z_0. The density contrast is defined as the difference between the density of the lithospheric mantle (ρ_{ml}) and the overlying crust (ρ_c). The original equation is expressed as:

$$F[\Delta g] = -2\pi G \rho exp\left(-|\vec{k}|z_0\right) \sum_{n=1}^{\infty} \frac{\vec{k}^{n-1}}{n!} F[h(\vec{r})^n] \qquad \text{(Eq. 2-1)}$$

Where G is the gravitational constant, $\vec{k}$ is the wavenumber vector, and $h(\vec{r})$ is the relative-height vector with respect to z_0. Gao and Sun (2019) re-derived the Fourier transform of Eq. 2-1 allowing the z-axis to be positive downwards, obtaining the following expression that describes the undulations at the interface (Moho):

$$F[-h(\vec{r})] = \frac{F[\Delta g] exp\left(|\vec{k}|z_0\right)}{2\pi G \rho} - \sum_{n=2}^{\infty} \frac{\vec{k}^{n-1}}{n!} F\left[(-h(\vec{r}))^n\right] \qquad \text{(Eq. 2-2)}$$

The inversion procedure is based on an iterative process that uses gravity data (Bouguer anomaly) and constant parameters z_0 and ρ until a convergence condition is reached (Oldenburg, 1974). As mentioned by Oldenburg (1974) and Gómez-Ortiz and Agarwal

(2005), Eq. 2-2 can be unstable for high frequencies so a high-cut filter multiplying the right-hand side of the equation is applied for convergence. The low pass filter rejects all frequencies above a higher threshold value referred to as SH, accepts all frequencies up to a low value referred to as WH, and applies a cosine filter over frequencies between these two reference values (Oldenburg, 1974).

2.4.1.2 Gravity data and inverted area

Gravity was obtained from two satellite-derived datasets: EGM2008 with an average 2.5 arc-minute resolution (Pavlis et al., 2012), and EIGEN-6C4 (Förste et al., 2014; Ince et al., 2019) with an equivalent ~18 km topographic wavelength from the spherical harmonic solution up to a degree and order of 2,190 (e.g. Gómez-García et al., 2021; Förste et al., 2014). Moreover, a regional total Bouguer anomaly map built by the National Hydrocarbon Agency of Colombia (ANH in Spanish abbreviation), published as a 5 mGal contour map (Graterol and Vargas, 2010), was also considered. The latter dataset will be hereafter referred to as ANH2010 for simplicity.

In the cases of EGM2008 and EIGEN-6C4, the gridded data were downloaded as available Bouguer gravity anomaly from the International Centre for Global Earth Models (ICGEM) (Ince et al., 2019), for which details about equations and parameters that were used to compute the Bouguer anomaly are given in Barthelmes (2009). A 0.5° grid spacing was used in all datasets given the intended comparison with respect to global Moho models: CRUST1.0 with a resolution of 1° (Laske et al., 2013) and GEMMA with a resolution of 0.5° (Reguzzoni and Sampietro, 2015). These global models were chosen to aim at a comparison with respect to seismic- and gravity-derived estimations.

The inverted area lies between 79.5°-66.5°W and 2.5°S-10.5°N, according to the spatial extent of the ANH2010 dataset. However, considering the edge effects, the implemented code uses a cosine taper window for which I applied the suggested truncation window of 10% of the extended data length (Gómez-Ortiz and Agarwal, 2005). I choose to keep our Moho depth discussions in the region between 78°-68°W and 1°S-9°N (area for interpretation box in Figure 2-1), allowing an area for interpretation not closer than 1.5° from the margins of the input gravity data.

As a limitation of this approach, steep Moho changes using this method can be partly evaluated by modifying the grid spacing of the input gravity data. Diminishing the grid spacing allows more constraints (nodes) per unit area which influences the algorithm to invoke steeper transitions in Moho depth. I evaluated this by using different grid spacing (0.2° and 0.25°) before the final 0.5° grid selection. I did not include this analysis, since the results were more complex and the steep Moho transitions beneath the northwestern Andes were out of the scope of this work. I wanted to depict, therefore, first-order Moho depth distribution and I considered that transitions between different tectono-geologic domains require a more appropriate and detailed methodology than the one used here.

2.4.1.3 The average depth parameter

When using the present approach, gravity inversion has been proven to be strongly influenced by the average depth parameter (z_0) (e.g. Oldenburg, 1974; van der Meijde et al., 2013; Ydri et al., 2020). Because this input parameter (average Moho depth) is a constant value that integrates the whole modeled area, what is recommended is to use the average depth beneath the region, although it might have thicker or thinner parts. The adjustments of thicker and thinner regions are what the inversion process allows to estimate. Therefore, initializing the algorithm with an average depth rather than a depth that might be biased for a particular region of the orogen, is a valid approach.

To select a value of z_0 that allows a proper comparison with the global Moho models, I analyzed the depth distribution of CRUST1.0 and GEMMA models within the inverted area (Figure 2-2). The associated depth histograms for each model suggest that an average depth of 41 km is a reasonable value to compare with CRUST1.0, whereas a 31 km average depth is well suited to compare with GEMMA. The selection of different starting values, when compared to global models, is justified by the fact that within the target region CRUST1.0 and GEMMA models have substantial differences, CRUST1.0 consistently suggesting thicker crust estimates than GEMMA. For the comparison, I made the a-priori assumption that one of those models should be more accurate than the other, without knowing which one. By doing this, I selected the dataset that minimized the differences with both global models, which means, that regardless of which of the global models is more accurate, the chosen dataset for final inversion will be better for the studied area than the other dataset possibilities.

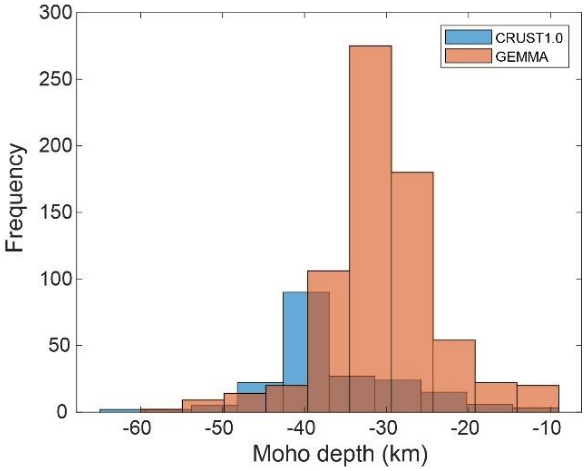

Figure 2-2. Histograms of Moho depth values derived from global models. From these histograms, I selected a reasonable average depth value of 41 and 31 km for comparing the inversions to CRUST1.0 and GEMMA Moho models respectively.

The comparison between the inverted gravity Moho and the seismic constraints was conducted by converting available crustal thickness into Moho depth (referred to as the depth with respect to mean sea level) below 24 seismic stations (Poveda et al., 2015). The conversion was done by subtracting the surface elevation from the crustal thickness at each station (e.g. van der Meijde et al., 2013), using the elevation data from the ETOPO1 model (Amante and Eakins, 2009). The work of Poveda et al. (2015) was considered for such comparison as it contains the best coverage to date along the Colombian region and discusses a comparison between their results and previous gravity and seismic estimates.

To evaluate the convergence of the algorithm, and to select the best parameter combination that minimizes the residual gravity (modeled minus observed data), 5,400 different setups (combinations of parameter values) were inverted using each gravity dataset. The number of different setups resulted from allowing the density contrast (ρ) to vary between 0.25-0.60 g/cm^3 (Sjöberg and Bagherbandi, 2011) with increments of 0.01 g/cm^3, whereas the WH and SH frequencies were taken between 0.005-0.0095 km^{-1} and 0.010-0.017 km^{-1} respectively, with increments of 0.0005 km^{-1}. The lower bound of 0.005 km^{-1}, representing a wavelength of ~200 km, was initially considered after van der Meijde et al. (2013), but the effects of lowering this bound will be discussed when improving the final inversion. For simplicity, I will discuss residual gravity in terms of its mean value and associated standard deviation.

2.4.1.4 Sedimentary basin correction

The applied frequency filter during the inversion allows the removal of short-wavelength sedimentary signals. Yet, the magnitude of the induced mismatch between the inverted Moho depth and the seismic constraints, when not removing the contribution of sedimentary basins with larger wavelength signals, remains debatable when applying this method (e.g. van der Meijde et al., 2013 and reference therein). I consider that sedimentary correction is applicable in areas where basement depth and density variation of the sedimentary units are well constrained (e.g. Gómez-Ortiz et al., 2005); otherwise, basement signals can be removed leading to Moho depth miscalculations.

Considering the complex deformational pattern, together with a strong variation of lateral thickness and sedimentary facies along the EC and the foreland region, where the major sedimentary basins of Colombia have been reported (Bayona et al., 2008; Horton et al., 2020; Mora et al., 2013; Sarmiento-Rojas, 2019), there is a high risk of removing basement gravity signals if the correction is applied. Therefore, I decided not to use this correction before inverting the gravity data and removing short-wavelength sedimentary signals by the applied filter, but being cautious when evaluating the possibility of an overestimated Moho depth in areas where thick sedimentary basins have been proven to exist (e.g. Aitken et al., 2013; Tirel et al., 2004), such as the Eastern Cordillera, the foreland region, and the coastal plains (Figure 2-1).

2.4.2 Choosing the best dataset

2.4.2.1 Comparison between datasets and global models

For comparison between datasets, using inverted depths at nodes in the considered 0.5° grid within the area for interpretation shown in Figure 2-1, I focus on the obtained differences in mean residual gravity and standard deviation. Mean residual gravity is somehow similar for all datasets: ANH2010 ranges between -5 to 7 mGal, whereas EGM2008 and EIGEN-6C4 are between -1 and 6 mGal, when using both average depths of 41 and 31 km, respectively (Figure 2-3). The differences between the datasets were more evident in the standard deviation. When considering a z_0 of 41 km, 529 setups showed a standard deviation of less than 10 mGal using ANH2010, whereas the minimum standard deviation achieved by EGM2008 and EIGEN-6C4 was between ~18-19 mGal (Figure 2-

3A). Similarly, when using a z_0 of 31 km, 1,577 setups showed a standard deviation of less than 10 mGal using ANH2010 data, whereas the minimum standard deviation obtained from EGM2008 and EIGEN-6C4 was ~14 mGal (Figure 2-3B).

When analyzing the inversions, by using both average depths, I observed that a higher number of setups with lower gravity residuals and standard deviation were accomplished when using a shallower average depth of 31 km, particularly with data from the EIGEN-6C4 model. However, under both scenarios, using a 41 or 31 km average depth, only the ANH2010 data provided inversions with a low gravity residual (-5 to 7 mGal) associated with a standard deviation lower than 10 mGal (Figure 2-3). Figure 2-3 illustrates the flexibility of the ANH2010 dataset to yield inversion models with the lowest gravity residual and standard deviation for a wider range of parameter combinations during the inversion. In simple words, this test shows that the best trade-off between convergence and fitness of the applied algorithm is obtained when using the ANH2010 dataset.

Aiming for comparison with global Moho models CRUST1.0 and GEMMA, Moho depth was obtained from each gravity dataset by using the parameter combination that minimizes the residual gravity (Supplementary Material S2-1). Since the datasets used for inversions are of higher spatial resolution in reference to the global models, the comparison can be made in order to detect first-order differences at a regional scale. In Figure 2-4 I show the differences in map view. It can be seen from all datasets, a good agreement for the foreland region, whereas the highest mismatches occur along the cordilleras and coastal plains (Figure 2-4).

Regarding CRUST1.0, all datasets show shallower values, mainly in the central CC and EC, and deeper values in the northern CC, EC, and both the Caribbean and Pacific plains (Figures 2-2 and 2-4A-C). The largest differences are suggested by the satellite-derived datasets in the Santander Massif and the southern cordilleran belt (Figures 2-4B and 2-4C, see also Figure 2-1).

Given the higher spatial resolution of GEMMA, the shallower values concerning the global model along the cordilleras are better depicted; the largest differences are shown by the satellite-derived datasets in central and southern CC and EC (Figures 2-4D-F). Deeper values are mainly shown in northern CC, EC, and coastal plains.

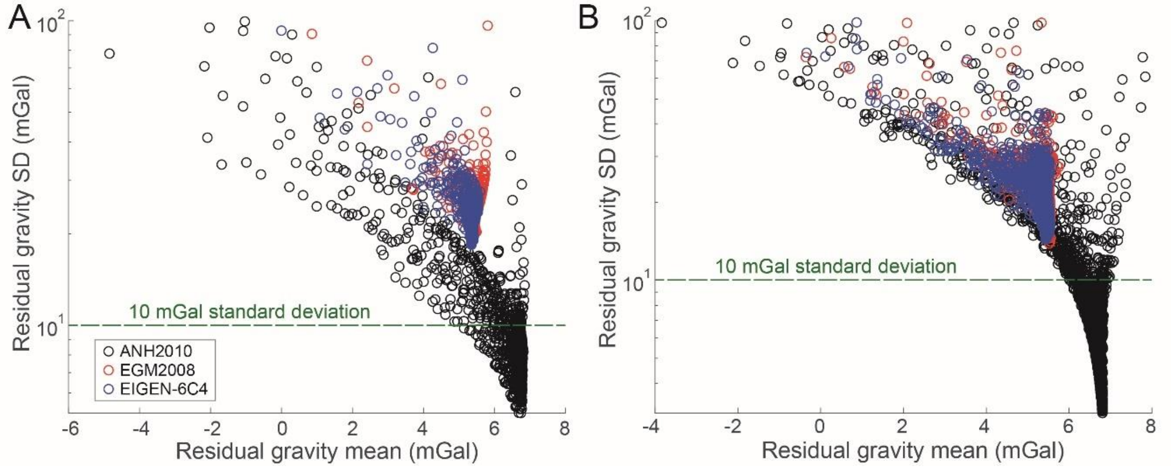

Figure 2-3. Mean residual gravity and standard deviation (SD) for the different gravity datasets, varying ρ, WH, and SH parameters. (A) Using an average depth of 41 km. (B) Using an average depth of 31 km. Only setups with a standard deviation lower than 100 mGal were plotted.

EGM2008 and EIGEN-6C4 suggest larger differences along the central-southern cordilleran belt (Figures 2-4E and 2-4F). Major differences between datasets and global models, especially for the ANH2010, are within the coastal plains, which might be linked to sedimentary basin infill and uncertainties in the continental to oceanic crust transition (e.g. Gómez-García et al., 2021).

Histograms depicting the differences between each inversion and global models are shown in Figure 2-5. The inversion with ANH2010 shows that most of the data differ by ± 5 km when compared with global models, whereas the inversions with EGM2008 and EIGEN-6C4 show that most of the data differ with respect to global models by about ± 10 km (Figure 2-5). Moho depth differences concerning the CRUST1.0 model include, for ANH2010 up to ~15 km shallower and ~23 km deeper values (Figure 2-5A), for EGM2008 up to ~20 km shallower and ~40 km deeper estimates (Figure 2-5B), and for EIGEN-6C4 up to ~20 km shallower and ~42 km deeper Moho depths (Figure 2-5C). The distribution of these differences is bimodal in all datasets, with major peaks at ± 5 km for ANH2010 and ± 10 km for satellite-derived datasets (EGM2008, EIGEN-6C4), as well as a second peak depicting 10-17 km deeper values from ANH2010 data, and 10-20 km deeper estimates from satellite-derived inversions (EGM2008 and EIGEN-6C4) (Figure 2-5).

Regarding the GEMMA model, differences are up to ~20 km shallower and ~15 km deeper values for ANH2010 data (Figure 2-5D), up to ~40 km shallower and ~25 km deeper estimates for EGM2008 (Figure 2-5E), and up to ~32 km shallower and ~20 km deeper Moho depths for EIGEN-6C4 data (Figure 2-5F). Those differences depict a normal distribution in all datasets, with a mean of 0.49 km and a variance of 27.56 km for ANH2010, a mean of 0.31 km, and a large variance of 52.51 km for EGM2008, and a mean of 0.31 km and a variance of 43.30 km for EIGEN-6C4 (Figure 2-5). Correlation coefficients, when compared to CRUST1.0 and GEMMA models respectively, are 0.27 and 0.52 for ANH2010, 0.24 and 0.36 for EGM2008, and 0.25 and 0.40 for EIGEN-6C4 inversion.

2.4.2.2 Consistency with receiver functions estimates

To evaluate the consistency of the Moho inversions from the gravity datasets with respect to seismic constraints (Poveda et al., 2015), I analyzed the Moho depth distribution beneath the northwestern Andean region. The inversions resulting from all datasets, using an average depth of 41 km and associated parameters (Supplementary Material S2-1), show a prevalent Moho depth of 40-50 km, with shallower 30-40 km values in the southern foreland region, beneath WC and southeast of the Merida Andes, and a deeper 50-60 km expression beneath the EC with the deepest anomaly around 1°S-2°N (Figure 2-6A-C, see also Figure 2-1 for geographical locations). Conversely, the inversion with a shallower average depth of 31 km, shows a dominant 30-40 km gravity Moho depth in all datasets (Figure 2-6D-F). As expected, by using a lower average depth, the inversion resulted in a regional-scale shallower Moho (e.g. Ydri et al., 2020), which strongly differs from available receiver functions estimates (see Figure 2-1 for seismic depth estimates).

Because of the better agreement between the inverted Moho depth and seismic constraints, while using the 41 km average depth (Figures 2-1 and 2-6), I used these inversions to compare with depth values derived from the receiver functions. For such comparison, I interpolated the inverted Moho depth at the location of individual stations reported by Poveda et al. (2015). An uncertainty of ± 4 km is suggested for the inverted gravity values, obtained from a variation in the average depth parameter by ± 2 km (e.g. van der Meijde et al., 2013).

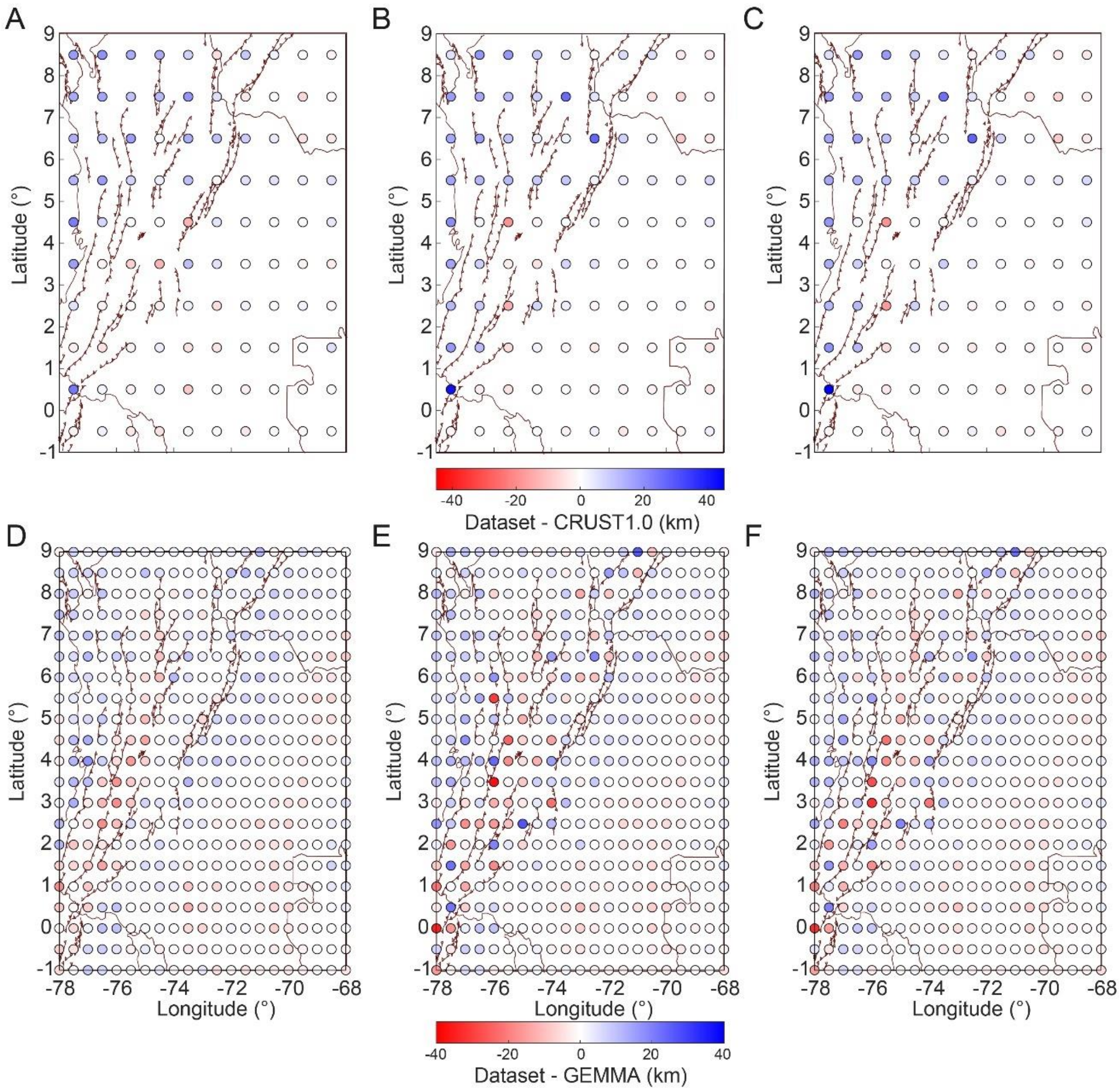

Figure 2-4. Moho depth differences between inversion of datasets and global models using a 41 km average depth: (A) ANH2010 minus CRUST1.0. (B) EGM2008 minus CRUST1.0. (C) EIGEN-6C4 minus CRUST1.0. Using a 31 km average depth: (D) ANH2010 minus GEMMA. (E) EGM2008 minus GEMMA. (F) EIGEN-6C4 minus GEMMA. Extension of the area for comparison as depicted by the area for interpretation box in Figure 2-1. Negative values shown in red represent shallower estimates, and positive values in blue are deeper estimates, with respect to global models. Active thrust faults as in Figure 2-1.

For simplicity, given that seismic constraints are reported in the form ‘A ± B km’, I will refer to the depth ‘A-B km’ as the lower (shallower) seismic bound and ‘A+B km’ as the upper (deeper) seismic bound. Furthermore, because I refer to the seismic station’s abbreviation (e.g. ROSC), I provide a geographical location (e.g. central EC), although the stations are depicted in Figure 2-7.

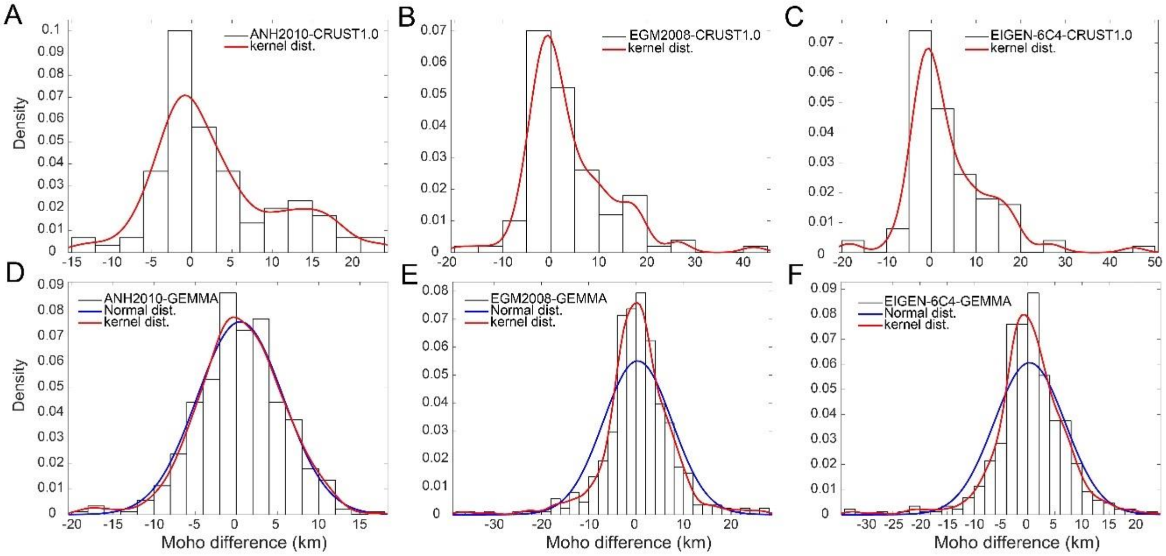

Figure 2-5. Histograms with kernel density estimates and normal density distributions show the differences between inverted gravity Moho and global Moho depth models. (A-C). Datasets minus CRUST1.0 model. (D-F) Datasets minus GEMMA model. A higher number of bins for GEMMA is shown given its higher spatial resolution (see Figure 2-4).

In this regard, shallower values (Figure 2-7) were suggested by the inversion with ANH2010 data for 2 stations, with a mismatch in-depth above 4 km (uncertainty) regarding the lower seismic bounds (Supplementary Material S2-1). Those stations are ROSC (central EC) and ZAR (transition from CC to the Caribbean plains), where differences between the maximum estimate (inverted depth plus 4 km) and the lower seismic bound, are ~0.5 and ~10.8 km respectively (Figure 2-7A, Supplementary Material S2-1). EGM2008 and EIGEN-6C4 suggest for 7 stations, shallower values with a mismatch in-depth above 4 km compared with the lower seismic bounds. The differences between the maximum estimate (inverted depth plus 4 km) and lower seismic bound, range 2.6-10.6 km at ANIL, HEL, and ZAR stations (northern CC and transition to Caribbean plains), between 1.2-11.8 km at BOCO, ROSC, and RUS (central-northern EC), and <1 km at PAM station (Santander Massif) (Figure 2-7B-C, Supplementary Material S2-1).

In terms of deeper estimates (Figure 2-7), the inversion with ANH2010 data suggests, for 8 stations, greater Moho depths with a mismatch above 4 km (uncertainty) compared with the upper seismic bounds (Figure 2-7A, Supplementary Material S2-1). Differences between the minimum estimate (inverted depth minus 4 km) and upper seismic bound, range 0.2-9 km at CAP2 and MON stations in the Caribbean plains, station PAL on the Western Cordillera, stations POP2 and RREF along the Central Cordillera, station PRA and VIL along the Eastern Cordillera, and station PTLC within the foreland region (Figure 2-7A). Inversions from EGM2008 and EIGEN-6C4 suggest deeper estimates with depth mismatching above 4 km at 6 stations (Figure 2-7B-C), including, MON station in the Caribbean plains, station YOT at the Western Cordillera, stations PCON, POP2, and RREF along the Central Cordillera, and station VIL on the Eastern Cordillera. Differences between the minimum estimate (inversion depth minus 4 km) and the upper seismic bound, range between 2.9 and 12.7 km at the mentioned stations for inverted satellite-derived datasets (Supplementary Material S2-1). The largest mismatch between the datasets and the upper seismic bound is depicted at the VIL station (eastern foothills of EC), yielding differences of ~9 km using the ANH2010 inversion, and between 11.6 and 12.7 km in the inversion from satellite-derived datasets (Figure 2-7). A correlation coefficient between the inverted values and the mean seismic depths yields 0.60 for ANH2010, 0.16 for EGM2008, and 0.17 for EIGEN-6C4 (Supplementary Material S2-1).

In summary, the ANH2010 inversion results in a higher number of matching stations in terms of Moho depth, in fewer stations differing in more than 4 km in depth with respect to seismic bounds, and in a higher correlation coefficient when compared to mean seismic estimations (Figure 2-7). The latter, coupled with the ability shown by this dataset to achieve a higher number of setups with low residual gravity and standard deviation lower than 10 mGal (Figure 2-3), reflects its potential to be used for the northwestern Andes and surroundings. Therefore, I choose this dataset to obtain the final Moho inversion.

2.5 Results: Improved inversion and overview of the northwestern Andean Moho topography

To improve the ANH2010 inversion, I further investigated the parameter values that minimize the differences with seismic constraints while yielding a standard deviation <10 mGal (minimizing residual gravity). For this, the WH range was incremented (0.001-0.0095 km^{-1}) to filter lower frequencies for evaluating the sensitivity of deeper sources.

Furthermore, the average depth parameter varied between 31 and 41 km with a 0.25 km step increment.

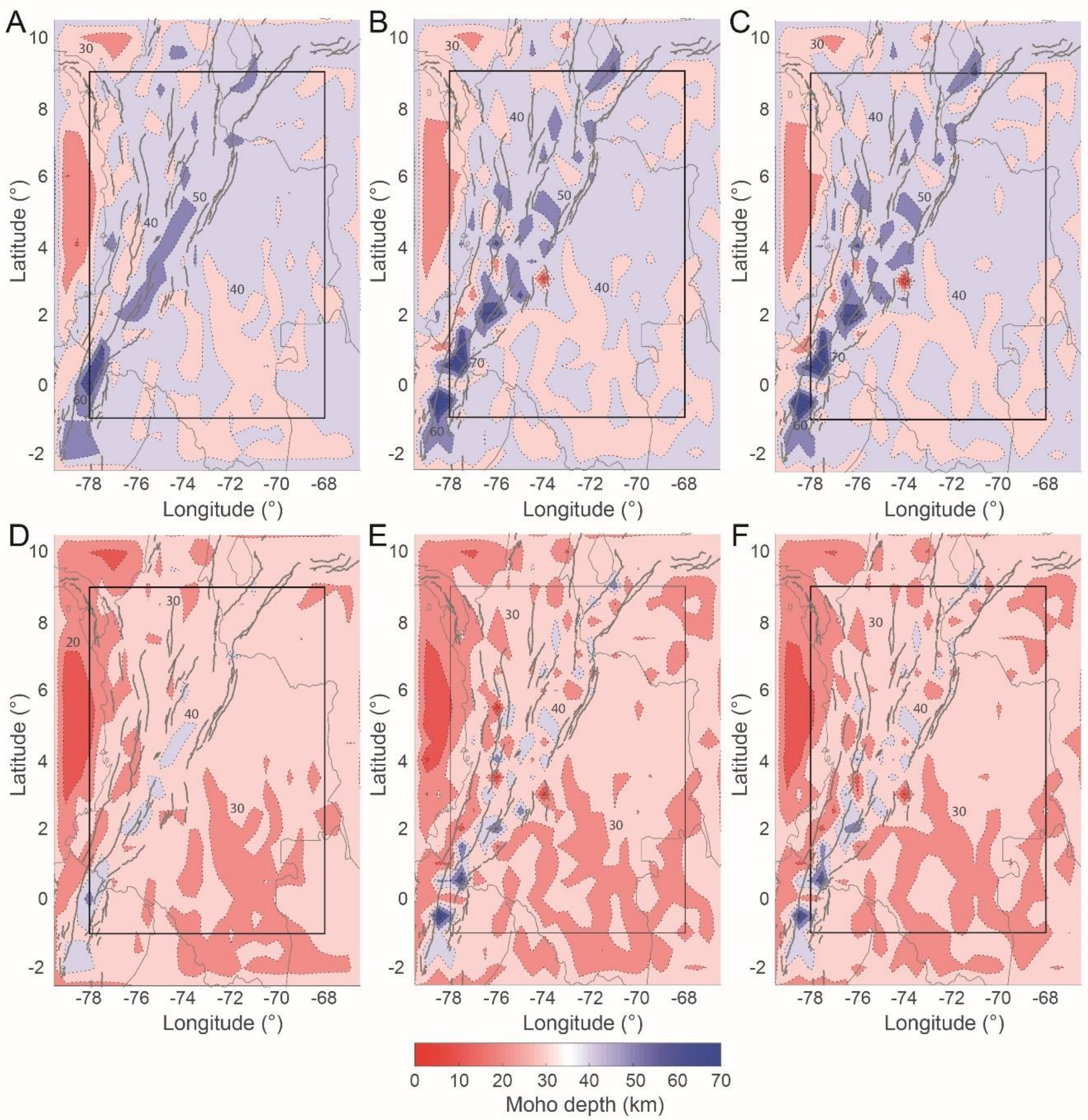

Figure 2-6. Inversion using a z_0 of 41 km, from different datasets: (A) ANH2010. (B) EGM2008. (C) EIGEN-6C4. Inversion using a z_0 of 31 km: (D) ANH2010. (E) EGM2008. (F) EIGEN-6C4. Active thrust faults as in Figure 2-1. The black box depicts the area for interpretation shown in Figure 2-1. A smooth interpolation was not applied at this stage. When reducing the average depth parameter from 41 to 31 km, a regional shallower Moho depth inversion is obtained. Aiming an easy view, the colorbar was set to depict in red, Moho depths shallower than 35 km, whereas in blue, depths deeper than 35 km.

The best combination of parameters minimizing the differences regarding mean Moho depth values from receiver functions was: an average depth of 37 km, a density contrast of 0.35 g/cm^3, and lower (WH) and upper (SH) cut-off frequencies of 0.001 and 0.0155 km^{-1}, respectively. The improved Moho inversion is shown in Figure 2-8 depicting a broad depth distribution for which uncertainty of ± 4 km is also considered as previously mentioned. It is worth noting that expanding the range of the lower cut-off frequency increased the agreement with respect to seismic constraints and allowed using a lower density contrast for the inversion.

This setup yields a mean residual gravity of 6.7 mGal and a standard deviation of 9.9 mGal, with a correlation coefficient with respect to mean seismic values of 0.63 (Supplementary Material S2-1). In a broad view, the inverted Moho depicts a ~40 to 50 km depth beneath the cordilleran belt reaching depths beyond 50 km below the Eastern Cordillera, and shallower depths between ~30-40 km mainly along the foreland region, the Western Cordillera, and the coastal plains (Figure 2-8A). Within the foreland region, residual gravity shows small patches up to 10 mGal where shallow anomalies are also depicted (<30 km), which are considered inversion artifacts; the rest of the foreland region agrees with a Moho between ~30-40 km, although a deeper expression (>40 km) is shown in the northwesternmost foreland and the northeastern foothills of the EC (Figure 2-8A). Small anomalies of ~40 km depth in the inner foreland are also considered inversion artifacts. The obtained ~30-40 km Moho depth beneath the foreland region agrees well with the ~35 km depth (Figure 2-9) obtained by Uieda and Barbosa (2017) from gravity inversion using the spherical harmonic model GOCO5S but considering a more complex inversion approach.

Beneath the Central and Eastern cordilleras, the Santander Massif, and the Merida Andes (see Figure 2-1), the gravity Moho shows a ~40-60 km depth (Figure 2-8A). Higher values between ~50-60 km are shown beneath the EC trend in an irregular pattern between 2°-6°N, and a deeper expression (>60 km) is depicted at a southern position below the modern magmatic arc (1°S-1°N). Within the EC and the Santander Massif, residual gravity shows only small patches of 10 mGal and up to 20 mGal in the southern cordilleran belt, arguing in favor of some degree of volcano-sedimentary basin residual gravity to the south. For the northern and central Eastern Cordillera (TAM, RUS, ROSC, CHI, BOCO stations) the gravity Moho (40.5-53.8 km) agrees well with seismic constraints (34.9-69.0 km), although for stations PRA and VIL the inversion suggests deeper values (Figure 2-8C;

Supplementary Material S2-1). For the Santander Massif, seismic constraints at the PAM station suggest a 48.1-56.5 km Moho depth, for which the gravity inversion agrees well, yielding 45.3 ± 4 km. Our inversion differs in this part of the orogen with respect to the estimates presented by Uieda and Barbosa (2017) (Figure 2-9) mainly because as they discussed, their method does not fully recover deeper Moho expressions within the Andean region.

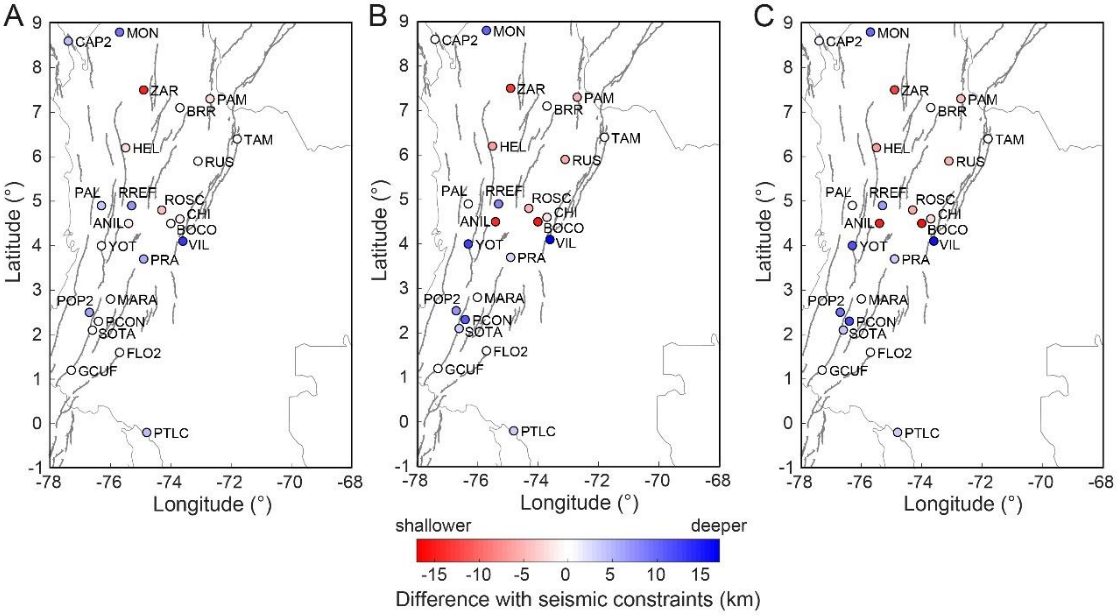

Figure 2-7. Depth comparison between inverted Moho and seismic constraints when using a 41 km average depth. (A) ANH2010. (B) EGM2008. (C) EIGEN-6C4. Zero represents inverted values in the range of seismic constraints, shallower values (red) and deeper values (blue) are with respect to seismic bounds (see Supplementary Material S2-1).

In the CC, a Moho depth between ~40-50 km is shown with a positive residual gravity of around 10 mGal. Beneath the RREF station (see Figure 2-8C), located at ~4.6°N at the Nevado del Ruiz active volcano, the suggested gravity Moho depth yields 45.3 ± 4 km which is slightly deeper than the depth suggested by seismic constraints (37.1-39.3 km). However, the Moho determination beneath this station is of higher complexity than that at ANIL station at the Cerro Machín volcano (see Figure 2-8C), which in fact, yields a Moho depth between 47.4-54.1 km being located ~60 km to the south of RREF station. At the RREF station, the compiled receiver functions show a larger azimuthal variation in delay times for the Moho determination, which implies a non-simple crust-mantle transition allowing a wider expression of the P to s converted phase arrival in the receiver functions, and thus, a higher uncertainty in the reported Moho depth. Higher delay times for the RREF station are observed for back-azimuths between 153°-282°, whereas at ANIL station the delay time for the converted phase (Ps) is better constrained, and therefore the Moho depth provides a lower uncertainty (Poveda, 2013). At ANIL station our inversion suggests 44.2 ± 4 km, which together with the previous value at RREF station, correlates well with seismic constraints.

For the southern CC, seismic estimates argue in favor of a 40.3-57.1 km Moho depth beneath MARA, PCON, and SOTA stations, which are similar to values of 47.7-51.5 km estimated at those sites from our inversion (Figure 2-8C). The deepest Moho (>60 km) lies in a southern latitude beneath the Central Cordillera (1°S-1°N), suggesting a spatial correspondence with the central-southern volcanic segment (Figure 2-8A). At station GCUF, our inversion suggests 51.6 ± 4 km depth, matching the seismic constraints that indicate 54.7 ± 8.2 km Moho depth. The CC claims a thinner crust compared to the EC; our inversion agrees well, in that sense, with the estimations presented by Uieda and Barbosa (2017), although they present slightly shallower values beneath the northernmost Central Cordillera (Figure 2-9).

Along the Western Cordillera, where residual gravity yields 0 to 10 mGal, a ~30 to ~40 km gravity Moho depth is estimated, which agrees well with seismic constraints, arguing for a ~31-40 km depth (Monsalve et al., 2013; Poveda et al., 2015). A deeper Moho (>40 km) is depicted beneath the Pacific plains between 3°-5°N; the nature of this anomaly is not well understood but it might be reflecting an overestimated depth caused by the overlooked effect of a thick sedimentary infill (Case et al., 1971). Hence, the Moho in this anomalous region could be shallower than suggested from our inversion. Except for such presumable overestimation, a general agreement with the Moho depths estimated by Uieda and Barbosa (2017) is achieved (Figure 2-9).

Seismic estimations in the Caribbean plains suggest 23.2-30.6 km Moho depth at MON station, whereas gravity inversion suggests a slightly deeper Moho of 35.9 ± 4 km. The latter may reflect the contribution of sedimentary units to some degree, which in fact, have been constrained in the order of ~4-6 km-thick in several parts of this region (Bernal-Olaya et al., 2015; Poveda et al., 2018). However, as shown in Figure 2-8A, the Caribbean plains show a broad ~30-40 km Moho depth which is in good agreement with estimations based on integrated seismic and gravity data (Bernal-Olaya et al., 2015). In this region though, a large mismatch at ZAR station is obtained: while seismic constraints suggest a depth of 57.6 ± 2.9 km, our gravity inversion yields 36.7 ± 4 km; taking into account the location of the station within the southern Caribbean plains and to the north of the termination of the high topography of Central Cordillera (see Figure 2-1), I consider our inverted value not to be highly mistaken, especially when considering similar values obtained from integrated seismic and gravity data along this region (Bernal-Olaya et al., 2015).

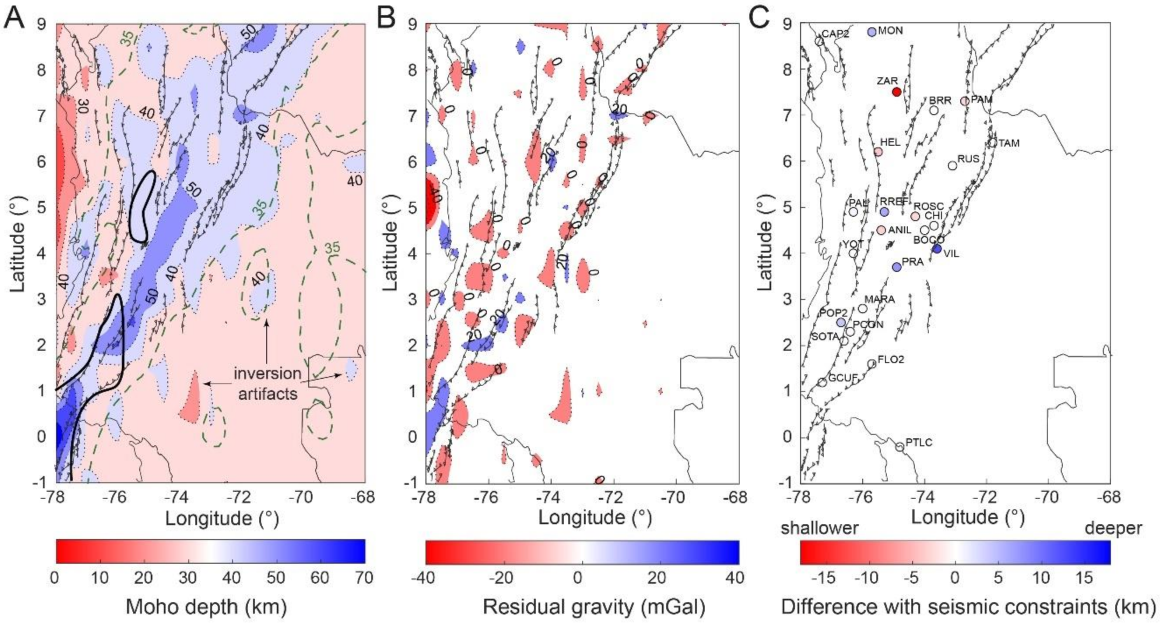

Figure 2-8. Results of gravity inversion after selecting the best setup for the ANH2010 dataset (see Supplementary Material S2-1). (A) Gravity Moho depth with dotted contours. For comparison the 35 km Moho depth contour from Uieda and Barbosa (2017) is shown in dashed green lines. Regions of active volcanism are represented by thick solid black polygons (see also Figure 2-1). (B) Gravity residual associated with the inversion. (C) Inverted depth compared with respect to seismic constraints (Poveda et al., 2015). Thrust faults in all panels as in Figure 2-1.

2.6 Discussion

A general tendency of a relatively deep continental Moho beneath the three cordilleras of the northwestern Andes is observed, with higher values beneath the EC and lower values beneath the WC (Figure 2-9). A moderately shallow Moho is depicted along the foreland region, while the lowest values were obtained within the coastal plains (Figure 2-9). In a broad sense, the inverted Moho shows some consistency with isostatic equilibrium, and although residual topography has been argued within the orogen, especially in northern Eastern Cordillera (Siravo et al., 2019; Yarce et al., 2014), the magnitude of such positive residual topography of less than 2 km lies within our depth uncertainty (± 4 km). Because some influence of sedimentary basins along the coastal plains might be affecting the inversion, overestimating to some degree the Moho depth, our tectonic interpretation will be mostly focused beneath the cordilleran belts.

Several interesting features are shown by the obtained gravity Moho distribution. In a first instance, a deep expression of the Moho (>40 km) in the northwesternmost foreland and the northeastern foothills of the Eastern Cordillera (Figure 2-9), is located to the east of the EC in a region where the mountain range is wider, shows its highest elevations, and where a thickened crust, even above 60 km, have been constrained by receiver functions (Monsalve et al., 2019; Poveda et al., 2015). Under the assumption of a gentle shallowing of the Moho, I consider that the expression of the northwestern foreland can be explained as a direct consequence of the adjacent thickened EC involving the fold and thrust deformation migration from the range towards the foreland, and the flexural deformation constrained in the eastern foothills and adjacent foreland region (Bayona et al., 2008; Parra et al., 2012; Siravo et al., 2018b). The wider and thicker expression of the EC in the central-northern part of the cordillera where thick-skin deformation has been constrained (Mora et al., 2013; Parra et al., 2012; Siravo et al., 2018b), allows for a higher load which can trigger a flexural deformation in the eastern foothills (see Bayona et al., 2008), resulting in a deepening of the Moho beneath the westernmost foreland adjacent to the cordilleran belt, as it has been proposed for the Central Andes (e.g. Whitman, 1994).

For the northern and central Eastern Cordillera, the gravity Moho agrees well with seismic constraints, although it suggests deeper values beneath the eastern foothills (Figure 2-8C). I consider the deep expression of the Moho beneath this part of the orogen to be related to the thickening history of the range, especially during the Cenozoic when thick-skinned deformation took place, as constrained along different segments of the cordillera (Bayona et al., 2008; Mora-Páez et al., 2016; Mora et al., 2013; Saeid et al., 2017; Siravo et al., 2018b). This shortening history is somehow represented in the inversion, by the spatial correspondence between deeper values along the EC and active thrust faults (Figure 2-9A). Furthermore, the tectonic shortening resulting in the thickening of the crust will allow higher topographic expressions associated with an isostatic response. This is the case of the Eastern Cordillera, where the highest topographic features are depicted above the thicker crustal regions, as shown by receiver functions (Poveda et al., 2015), and although there have been some suggestions of positive residual topography in the range (Yarce et al., 2014; Siravo et al., 2018), as previously mentioned, the amount of excess in topography (<2 km) is within the inversion uncertainty (± 4 km).

For the central section, a contribution of magmatic underplating has also been interpreted more clearly beneath the RUS station (Figure 2-8C; Monsalve et al., 2019). I speculate that localized magmatic underplating at the base of the crust in this part of the orogen allows a deeper Moho expression beneath the central part of the EC and shallower depths towards the north of the range and the Santander Massif.

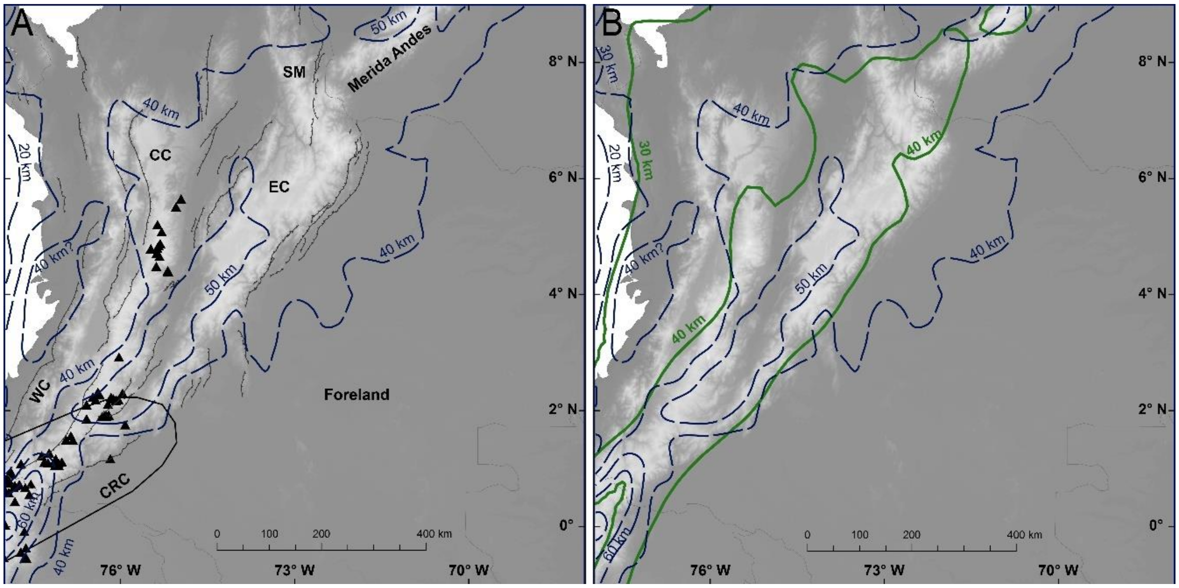

Figure 2-9. (A) Suggested Moho distribution beneath the northwestern Andes and foreland region not showing contours of inversion artifacts and likely overestimations in some regions. The thick expression in the Pacific region enclosed by the 40 km contour with a question mark (40 km?), might reflect an overestimated Moho due to sedimentary infill. Black triangles are active volcanoes, CRC stands for Carnegie ridge continuation (Gutscher et al., 1999), and thrust faults are presented as in Figure 2-1. (B) Comparison between regional-scale Moho depth estimates: dashed blue lines are depths obtained by our inversion, whereas solid green lines are from Uieda and Barbosa (2017).

The relationship between the volcanically active segments of the hinterland and the Moho depth is not easy to envision. The northern segment of the modern volcanic arc does not seem to be correlated with a distinctive geometry of the Moho depth. Conversely, the southern portion of the arc lies above the deepest Moho expression within the inverted area (>60 km at 1°S-1°N) (Figure 2-9). For this region, lower crustal xenoliths brought to the surface by Plio-Pleistocene volcanism, argue for a much thicker crust (up to 80 km) than available seismic constraints and our inversion estimates (e.g. Bloch et al., 2017). However, the thickening history of this part of the orogen is still poorly constrained. Poveda et al. (2015) discussed high Vp/Vs ratios beneath the volcanic centers, claiming the potential presence of mafic materials at the base of the crust, which might be contributing to its thick structure. Because the considered approach is not robust enough to discuss in more detail the magmatic underplating hypothesis, I consider it as one of the possibilities to explain the thicker expression at this latitude. On the other hand, Bloch et al. (2017), based on depth and density estimations from recovered xenoliths, interpreted a gravitationally unstable lower crust for which they claimed foundering tectonics. Again, the implemented approach is not able to discern between these two feasible mechanisms and are thus, included as possibilities.

Furthermore, I include an extra possibility for thickening this part of the orogen based on the work presented by Bishop et al. (2017) in the Central Andes, where the increase in crustal thickness is associated with the Nazca ridge; this can be a good example to compare with, since it is proposed, for a segment of the Andes associated with a ridge that resembles the Carnegie setting interacting obliquely with the margin. The projection of the subducted part of the Carnegie ridge in the study area (Figure 2-9A) allows me to hypothesize that it might be affecting the upper plate structure, particularly along the southern part of the area where the inversion yields a thick crust; yet, little is known about the role of this buoyant entity in the deformation pattern in this part of the orogen. I speculate that the subduction of this element could be causing crustal thinning in the overriding South-American plate, localized along the trajectory of the ridge, and prompting local thickening in the surrounding areas by lateral lower crust displacement, as suggested for the central Andes due to the subduction of the Nazca ridge (Bishop et al., 2017). As shown in Figure 2-1, the thinning of the overriding plate agrees well with receiver functions (Poveda et al., 2018, 2015) suggesting a disrupted thickened crust along the Colombian-Ecuador border (see also Koch et al., 2021), where the continuation of the Carnegie ridge subduction has been proposed (Gutscher et al., 1999). Additionally, xenolithic data indicating a much thicker crust compared to seismic constraints in the Colombian region, coupled with the short-wavelength pattern shown by the inversion in this area, allowed me to favor a local thickening during the advance of the ridge subduction rather than a regional crustal shortening mechanism.

2.7 Conclusions

Through a comparison of multiple gravity datasets, the regional airborne Bouguer gravity anomaly map, built by the National Hydrocarbon Agency of Colombia (Graterol and Vargas, 2010), was selected as the most suitable dataset to gain insights into the Moho depth beneath the northwestern Andes. A general tendency of a Moho depth between ~30-60 km beneath the three cordilleras in the Colombian Andes is observed, with deep values found beneath the Eastern Cordillera (~50-60 km), relatively shallow values beneath the Western Cordillera (~30-40 km), and an anomalously deep Moho in the southern cordilleran belt beneath the modern magmatic arc (>60 km). A moderately shallow Moho (~30-40 km) is obtained along the foreland region and the coastal plains; in the latter region, some influence of the sedimentary basins is likely causing an overestimation of the Moho depth.

Three main expressions of regional extent were detected from the inversion: (1) a deep expression (>40 km) in the northwesternmost foreland, interpreted as a direct consequence of a gentle shallowing of the Moho from the adjacent thickened Eastern Cordillera involving the fold and thrust deformation migration from the range towards the foreland, and the flexural deformation constrained in the eastern foothills and adjacent foreland region (Bayona et al., 2008; Parra et al., 2012; Siravo et al., 2018b), (2) a regional deep expression (~50-60 km) along the Eastern Cordillera trend, interpreted as a combination of its shortening history involving multiple Cenozoic thick-skinned deformational events (Bayona et al., 2008; Mora et al., 2013), and magmatic underplating (Monsalve et al., 2019), and (3) a deep anomaly (>60 km) in a southern latitude beneath the modern magmatic arc (1°S-1°N), which can be interpreted as a combined result of the potential presence of mafic materials at the base of the crust (Poveda et al., 2015), a gravitationally unstable lower crust experiencing foundering tectonics (Bloch et al., 2017), and lateral lower crust displacement triggered by the subducting Carnegie ridge.

2.8 Publication or submission

This paper has been published in Geophysical Journal International.

Avellaneda-Jiménez, D.S., Monsalve, G., León, S., Gómez-García, A.M., 2022. Insights into Moho depth beneath the northwestern Andean region from gravity data inversion. Geophysical Journal International, Vol. 229, Issue 3, June 2022, Pages 1964–1977, https://doi.org/https://doi.org/10.1093/gji/ggac041.

2.9 Acknowledgments

Thanks to G. Posada and L. Ramírez-Hoyos for their help in gathering the ANH data in a useful format, and T. Becker for fruitful discussions, which allowed us to improve the quality of our manuscript. Comments and suggestions from editors B. Vermeersen and F. Storey, as well as those from R. Bernal and two anonymous reviewers substantially improved the quality of this work. This work was supported by the Fundación para la Promoción de la Investigación y la Tecnología (Project 4.634).

3. Seismic and thermo-compositional insights into the uppermost mantle beneath the Northern Andes magmatic arc

3.1 Summary

The mantle wedge beneath the Northern Andes magmatic arc is expected to be latitudinally heterogeneous as suggested by the highly variable composition of recovered xenoliths, a discontinuous pattern of low seismic velocity zones, and unusually high Vp/Vs ratios below volcanic centers. Such heterogeneity might be controlling the development of the modern arc which currently shows a narrow northern volcanic segment between ~4°-6°N (<75 km wide), a volcanic gap of hundreds of km in its central portion (~2°-4°N), and a wider southern volcanic expression between ~2°S-2°N (>120 km wide). Through an analysis of Pn and Sn inter-station wave speed estimates, the seismic structure dissimilarity and latitudinal thermo-compositional insights were constrained within the uppermost mantle beneath the arc. Results, integrating wave speed estimates, anisotropy, and thermo-compositional inferences obtained by wave velocity comparison using physical properties of minerals and phase equilibria modeling, suggest a seismically slower structure, higher anisotropy, and warmer conditions beneath the northern region (>4°N), whereas a faster, less anisotropic, and colder mantle towards the south (<2°N). I interpret the warmer and higher degree of anisotropy in the northern uppermost mantle as influenced by the Caldas tear, prompting hot mantle influx. Beneath the gap region, seismic speeds are similar to those in the north, yet a colder thermal state is suggested. I interpret the colder temperatures and the abrupt reduction in surface volcanism as reflecting an absence, or a reduced amount of magma pounding within the Moho vicinity. The southern upper mantle is seismically faster and colder compared to the northern portions of the arc. I interpret the

fast velocities, and a wider volcanic expression on the surface, as influenced by the Carnegie ridge interaction prompting shallower subduction with respect to the north. The wave speed estimate and thermo-compositional inferences draw an increase in temperature and seismic anisotropy in the uppermost mantle from south to north along the Northern Andes magmatic arc. The main controlling factor of the general anisotropy below the entire arc seems to be the preferred orientation of olivine and pyroxene rather than an aligned melt fabric.

3.2 Introduction

The upper mantle beneath continental magmatic arcs is strongly influenced by trench-parallel dissimilarities of the subduction configuration (subduction angle, convergence rate, slab age, thermal structure), prompting a heterogeneous seismic structure within the mantle wedge (Ferrari et al., 2012; Marot et al., 2014; Wagner et al., 2005). The seismic inhomogeneity is commonly attributed to variations in composition, temperature, and/or fluid content (Christensen, 2004; Manea and Manea, 2011; Wagner et al., 2008). However, other aspects like melt fraction, material underplating, restitic peridotite evolution, and mantle anisotropy can also play an important role in the uppermost mantle seismic structure (Afonso and Schutt, 2012; Delph et al., 2017; Hacker and Abers, 2012; Hyndman and Peacock, 2003). Understanding the nature of the heterogeneity within the mantle wedge is of major importance since it strongly influences the magmatic expression in the upper plate and the dynamic response of the latter to current tectonics.

Both the morphologically intricate nature of the northern Nazca plate, as well as the complex subduction-related geodynamics along the northwestern Andes, since at least the latest Oligocene to middle Miocene, have been documented and discussed (Lonsdale, 2005; Montes et al., 2019). The northern Nazca plate morphology is described by a trench-parallel variation of its subduction angle, seemingly the result of multiple events of slab flattening, steepening, and tearing during the past 14 Ma (Chiarabba et al., 2015; Kellogg et al., 2019; Vargas and Mann, 2013; Wagner et al., 2017) (Figure 3-1). This geometry, coupled with the presence of lithospheric weaknesses, barriers, and buoyant elements within the subducting slab, such as the Sandra and Malpelo rifts, and Malpelo and Carnegie ridges (Figure 3-1), caused mantle wedge heterogeneities that remain poorly understood, especially beneath the active volcanic region (Vargas et al., 2019, 2007).

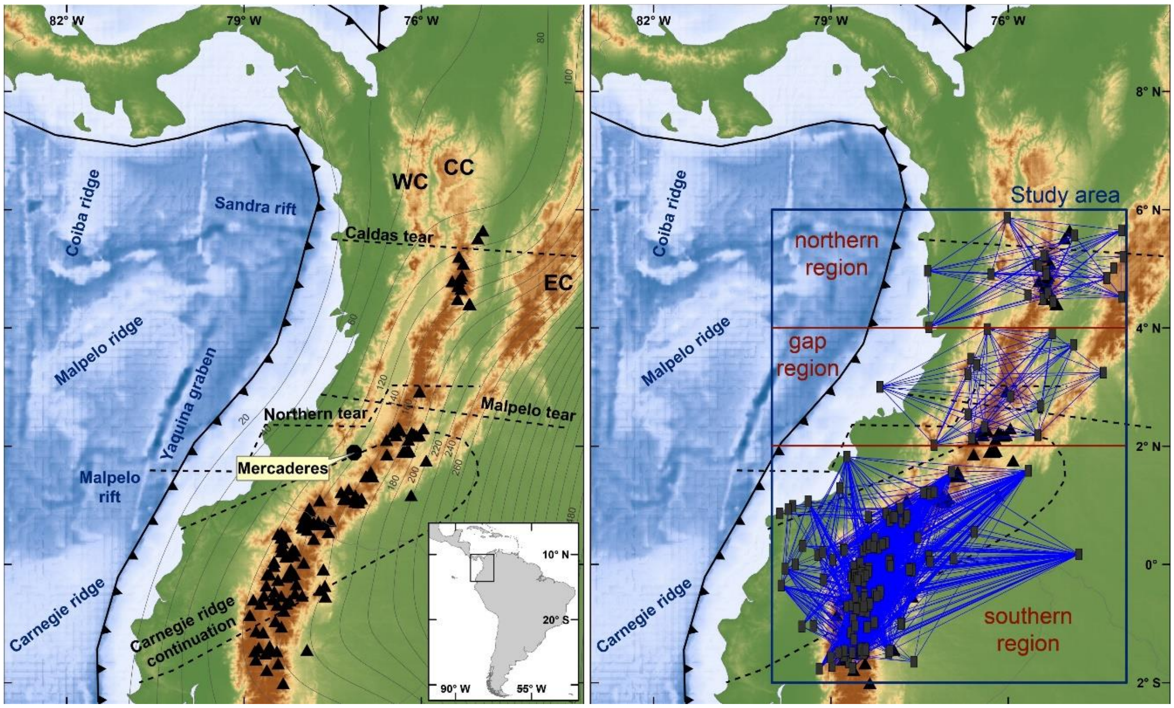

Figure 3-1. Simplified map of the northern Andes showing the distribution of current volcanism (black triangles), and the different hypothesized Nazca slab tears and their buoyant and weakness features (Malpelo and Sandra rifts, Yaquina graben, Carnegie and Malpelo ridges). Dark-blue rectangle delimits the study area, whereas blue lines are ray paths from the computed velocity estimates in the northern, central, and southern regions. Grey rectangles within the study area are the considered stations for the velocity estimates. Caldas tear from Vargas (2020), Malpelo tear from Idárraga-García et al. (2016), Northern tear and Carnegie ridge continuation from Gutscher et al. (1999), and subduction slab contours after Hayes et al. (2018). EC: Eastern Cordillera; CC: Central Cordillera; WC: Western Cordillera. Mercaderes is the locality at which mantle xenoliths have been documented (Rodriguez-Vargas et al., 2005; Weber, 1998).

Pieces of evidence supporting the inhomogeneity of the mantle wedge include the highly variable composition of recovered mantle xenoliths that were brought to the surface during Plio-Pleistocene volcanism (Rodriguez-Vargas et al., 2005; Weber, 1998), the discontinuous pattern of low seismic velocity zones beneath the modern volcanic regions (Chiarabba et al., 2015; Syracuse et al., 2016; Vargas et al., 2007), and unusually high Vp/Vs ratios mainly below volcanic centers (Koch et al., 2021; Poveda et al., 2015). The current volcanism also agrees well with the idea of a heterogeneous mantle, describing a trench-parallel segmented arc with a ~265 km gap in its central portion (Monsalve-Bustamante, 2020; Monsalve-Bustamante et al., 2020), which is consistent with an uneven distribution in the mantle wedge fertility, or an along-arc variability in temperature or hydration conditions. Moreover, a thermo-compositional dissimilarity of the mantle wedge is also depicted by the dominance of mafic products with alkaline affinity in a rear-arc position, especially to the south, and a discrete appearance of adakite-like rocks in different regions of the arc (Chiaradia et al., 2009; Marín-Cerón et al., 2019; Monsalve-Bustamante et al., 2020).

In this chapter, I present geophysical evidence supporting the idea of latitudinal seismic inhomogeneity of the mantle wedge beneath the active northwestern Andes magmatic arc, by means of Pn and Sn velocity variation. I discuss the dissimilarity in seismic wave speeds for the active northern segment of the volcanic arc, an extended volcanism-free region, and the currently active southern region of the Northern Andes arc, arguing about feasible controlling factors such as the thermo-compositional structure and uppermost mantle anisotropy.

3.3 Tectonic setting

The subduction beneath the Northern Andes comprises a broad flattened northwestern segment to the north of ~5°-5.5°N, and a southern portion with a normal/steep angle (Hayes et al., 2018; Syracuse et al., 2016; Vargas, 2020). Yet in the vicinity of the Carnegie ridge, at latitudes to the south of 2°N, the subduction angle decreases again (Gutscher et al., 1999). To the northwest, the shallow-dipping subduction system includes the buoyant Caribbean plate, the underthrusting Panama arc, and a possible fragment of the Nazca plate (Chiarabba et al., 2015; Syracuse et al., 2016; Vargas and Mann, 2013). Between 5° and 5.5°N, the proposed Caldas tear bounds the northwestern flattened subduction (Figure 3-1); this feature marks the northern limit of the active volcanism (Vargas and Mann, 2013; Wagner et al., 2017). To the south of the tear, the subducting system is defined by the Nazca plate, formed during the Farallon lithospheric rupture into Cocos and Nazca portions around 23 Ma (Lonsdale, 2005). Currently, the Nazca plate is youngest (9-12 Ma) near the now extinct Sandra rift (Lonsdale, 2005), for which its collinearity with the proposed Caldas tear suggests a stripe of lithospheric weakness (Vargas & Mann, 2013).

The trench-parallel variation of the dipping Nazca slab includes in southern Colombia and northern Ecuador, a flattened geometry that has been related to the current subduction of the Carnegie ridge, and a slab tear bounding this segment to the north, referred to as Northern tear by Gutscher et al. (1999), or Malpelo tear by Borrero & Castillo (2006) and

Idárraga-García et al. (2016) (Figure 3-1). Associated adakite-like rocks and alkaline basalts in the central segment of the modern arc have been interpreted as hot asthenospheric upwelling and slab edge melting associated with such tear (Borrero and Castillo, 2006; Monsalve-Bustamante et al., 2020; Monsalve et al., 2015).

In between the Caldas and Malpelo tears, the geometry of the Nazca slab exhibits apparent complexities. On one side, a steep ESE dipping slab with a subduction angle between 30° and 40° has been proposed (Gutscher et al., 1999; Pennington, 1981), whereas Pedraza-Garcia et al. (2007) claim that the slab geometry in this region shows initial shallow subduction with a 17° dip angle changing to 45° at depths below 100 km.

The subduction of the Nazca plate has been responsible for the formation of the Northern Andes modern arc, which based on its volcanic expression, can be subdivided into three regions (Figure 3-1). The northern segment (north of 4°N) shows a relatively narrow volcanic expression (<75 km wide), being located ~300 km from the trench. Between ~2°-4°N there is a ~265 km long volcanic gap (Monsalve-Bustamante, 2020), located 270-280 km from the trench. The southern region shows a wider expression of arc volcanism (>120 km wide) being located 240-250 km from the trench (Monsalve-Bustamante et al., 2020). Evidently, the distance between the arc and the trench increases towards the north. In a rear-arc position, although more common for the southern region, a series of mafic products have been documented, being much greater in volume and geochemically enriched (alkaline affinity) to the south (Monsalve-Bustamante et al., 2020). For simplicity, I will refer to the regions north of 4°N, between 2°-4°N, and south of 2°N, as the northern, gap, and southern regions, respectively.

3.4 Methods

3.4.1 Pn and Sn velocity estimations

To study the seismic velocity variation within the uppermost mantle, I use Pn and Sn waves, which are considered to travel just beneath the Moho and are critically refracted at the mantle-crust boundary (Storchak et al., 2003). Arrival times associated with these waves were obtained from the International Seismological Centre (ISC) database, using records between 2010 and 2020 for all stations located between 6°N and 2°S and 80° to 74°W (study area in Figure 3-1). The stations and their records were then subdivided into three datasets to independently compute the seismic speeds within each region along the arc (Figure 3-1).

To estimate the mantle velocity I applied the two-station approach, aiming to minimize the effects of hypocenter location uncertainties and crustal heterogeneity at the source (Beghoul and Barazangi, 1989). The method consists of calculating the arrival time difference of the Pn (Sn) wave at two different stations (station pair) from a given seismic event, and estimating a representative velocity along the inter-station distance by using the arrival time difference. Since the stations are on the surface while the Pn (Sn) waves are traveling below the Moho, a correction factor multiplying the inter-station distance can be determined under the assumption of a spherical Earth. I considered the correction factor as $(Er - ct)/Er$, where Er is the Earth's radius and ct is the crustal thickness. Using an Er of 6,371 km (e.g. Shearer, 2009), crustal thicknesses of 40, 45, or 50 km, which are reasonable values for the target area (chapter 2; Poveda et al., 2015), yielded correction factors of 0.994, 0.993, and 0.992 respectively, from which I used 0.993 in this work. I preferred to use a 45 km thick crust as a representative value instead of considering a variation in thickness along the arc. This decision was made based on the fact that possible values for crustal thickness in several parts of the arc, are a matter of current and active discussion (Bloch et al., 2017; Poveda et al., 2015). For example, the average values from Poveda et al. (2015) based on receiver functions, might be underestimated beneath the southern and northern regions, as other constraints have suggested (chapter 2; Bloch et al., 2017). To avoid these complications, I considered an average crustal thickness, which is a reasonable assumption given the obtained correction factors and their variations.

To implement the two-station approach, a seismic event must fulfill the following conditions (see Beghoul & Barazangi, 1989): (1) a maximum residual travel time of ± 3 s, calculated with respect to a reference seismic velocity model; (2) epicentral distance greater than 2° and less than 16° with respect to the nearest station; (3) the epicenter must not be located between the considered station pair; (4) the earthquake must be located at an angle not greater than 6° with respect to the line that connects the two stations (inter-station azimuth); and (5) the earthquake magnitude should be greater than 3.

For a given station pair, each event fulfilling the previous conditions can provide a velocity estimate. I selected the data to consider velocities in the range 6.5-8.5 km/s for Pn and 3.5-

5.0 km/s for Sn, for those station pairs separated at least 100 km (inter-station distance threshold) (e.g. Collins and Molnar, 2014). Supplementary Material S3-1 lists the final velocity estimates presented in this work (11,566 Pn and 746 Sn speed estimates).

	Northern region (>4°N)			Gap region (2°-4°N)			Southern region (<2°N)		
Mag.	≥3	≥4	≥5	≥3	≥4	≥5	≥3	≥4	≥5
A (Pn)	7.68	7.69	7.59	7.66	7.64	7.65	7.79	7.80	7.81
B (Pn)	0.14	-0.23	0.32	0.29	0.27	0.15	0.18	0.08	0.26
C (Pn)	0.72	-1.08	0.73	0.70	0.73	0.44	0.84	10.22	0.35
Anis. (Pn)	3.77	6.08	8.36	7.49	7.13	3.86	4.67	2.04	6.54
A (Sn)	4.41	-	-	4.39	-	-	4.37	-	-
B (Sn)	0.07	-	-	0.09	-	-	-0.44	-	-
C (Sn)	0.49	-	-	0.60	-	-	1.08	-	-
Anis. (Sn)	3.21	-	-	3.94	-	-	-	-	-

Table 3-1. Coefficients associated with the cosine function (Eq. 3-1) describing the anisotropy in each region. Different magnitude (Mag.) thresholds were used and plotted in Figures 3-2 to 3-4. Anisotropy percentage (Anis.) is calculated using Eq. 3-2.

3.4.2 Anisotropy

As it will be discussed, the mantle beneath all regions along the arc shows variations in seismic speeds with the inter-station azimuth (Figures 3-2 to 3-4). To evaluate mantle anisotropy and better compare the differences between the three regions, I adjusted the velocity estimates to a cosine function (Collins and Molnar, 2014):

$$V = A + Bcos\left(2(Iaz - C)\right) \qquad \text{(Eq. 3-1)}$$

Where V represents the mean Pn (Sn) velocity estimate for 10° inter-station azimuth bins using the two-station approach, Iaz is the middle inter-station azimuth from the respective 10° bin, and A, B, and C, a set of coefficients that are estimated to fit the data to the equation. Coefficient A represents the average velocity, C is related to the fast/slow axes orientations, and B is related to the anisotropy percentage (e.g. Collins and Molnar, 2014):

$$anisotropy(\%) = 2 * \frac{B}{A} * 100 \qquad \text{(Eq. 3-2)}$$

For the fitting process, I used the Curve Fitter Matlab^{MT} app. For each region I analyzed the effect of earthquake magnitude into the equation fitting, by using all the data (speeds based on earthquakes with magnitudes $\geq$3), and using only the velocity estimates based on earthquakes with magnitudes greater than 4 and 5, respectively (Figures 3-2 to 3-4). Coefficients and anisotropy percentages are presented in Table 3-1.

3.4.3 Thermo-compositional inferences

Given the likely different architecture of the subduction system in the three defined regions, I suspect that there are differences in seismic speeds between them. To test for a thermo-compositional controlling factor, I used two different approaches, inversion, and forward modeling, to envision possible temperature and compositional variations based on Pn and Sn estimates along the arc.

Given the anisotropy that is present in the three regions, I selected the data in each dataset to gather those earthquakes yielding a Pn velocity estimate within less than ± 0.2 km/s with respect to the average speed in each region (A coefficient in Table 3-1). The latter means that those estimates yielding faster and slower velocities than 0.2 km/s with respect to the average speed, were not used for the thermo-compositional analysis. I used as the average speed, the one obtained from using all earthquakes with magnitudes $\geq$3, since they describe better the anisotropy due to their larger coverage in the inter-station azimuth (Figure 3-2). Average Pn speeds were set to 7.68, 7.66, and 7.79 km/s for the northern, gap, and southern regions respectively (Table 3-1).

Those earthquakes were then selected to use the ones for which an Sn velocity calculation was computed (Figure 3-5). From the final set of events, the velocity residuals were computed as the difference between the Pn and Sn estimates given for each earthquake (two-station approach), and the velocities obtained from the inverse and forward modeling. I consider as a feasible setup (in this work used to refer to a combination of temperature and mineral content) for explaining the wave speeds associated with each event, those yielding velocity residuals lower than 0.01 km/s in both waves, meaning: the Pn (Sn) from the two-station approach minus the Vp (Vs) from each modeling approach.

Results are presented in Supplementary Material S3-2. Although a more complete mineral assemblage is presented in the supplementary tables for both types of modeling, I kept the analysis simple by considering just pyroxene and amphibole proportions. I consider that their relative amounts can be used to draw differences in the hydrated conditions.

Moreover, a limitation of our approach is that I did not include any constraints on anelasticity and attenuation, given that these parameters are well-calibrated only for a few minerals, such as olivine (Abers and Hacker, 2016). Thus, results from this analysis are used to address qualitative differences between the regions, and should be taken with caution when compared to other mantle domains.

3.4.3.1 LSQR approach (inverse modeling)

Using the dataset of Abers & Hacker (2016), I test feasible mineral compositions that can reflect the estimated Pn and Sn speeds. I considered a relatively simple mantle composition including olivine (Forsterite-Fo, Fayalite-Fa), pyroxenes (Enstatite-En, Ferrosilite-Fs, Diopside-Di), Al-phase (Pyrope-Py, Spinel-Sp), and amphibole (Hbl). This composition is suitable for the uppermost lithospheric mantle (Griffin et al., 2009; Lee, 2003).

For each earthquake associated with a given station pair with both Pn and Sn velocity estimates, a feasible mineral proportion X was calculated using the LSQR algorithm (Paige and Saunders, 1982) in Matlab™ (least-squares method). The compositional problem was set in algebraic form as:

$$\begin{bmatrix} Vp^{Fo} & Vp^{Fa} & Vp^{En} & Vp^{Fs} & Vp^{Di} & Vp^{Py} & Vp^{Sp} & Vp^{Hbl} \\ Vs^{Fo} & Vs^{Fa} & Vs^{En} & Vs^{Fs} & Vs^{Di} & Vs^{Py} & Vs^{Sp} & Vs^{Hbl} \\ 1-Mg\#^{Ol} & -Mg\#^{Ol} & 0 & 0 & 0 & 0 & 0 & 0 \\ 0 & 0 & 1-Mg\#^{Opx} & -Mg\#^{Opx} & 0 & 0 & 0 & 0 \\ 0 & 0 & 0 & 0 & 0 & 0 & 1 & 0 \end{bmatrix} * \begin{bmatrix} X_{Fo} \\ X_{Fa} \\ X_{En} \\ X_{Fs} \\ X_{Di} \\ X_{Py} \\ X_{Sp} \\ X_{Hbl} \end{bmatrix} = \begin{bmatrix} VPn \\ VSn \\ 0 \\ 0 \\ Sp^{*} \end{bmatrix}$$

Where, Vp^i and Vs^i represent the P- and S-wave velocity for the mineral endmember i respectively; $Mg\#^{Ol}$ and $Mg\#^{Opx}$ are a set of constant values for the Mg# in olivine and orthopyroxene, evaluated as $Fo/(Fo+Fa)$ and $En/(En+Fs)$, respectively; VPn and VSn are the estimated speeds based on the two-station approach; Sp^* is a constant proportion of spinel. The latter was included in the compositional problem because small amounts of spinel are expected in mantle assemblages (Jennings and Holland, 2015; Lee, 2003).

The solution vector X was calculated by setting the compositional problem at a constant temperature and a pressure of 2 GPa. The code was set to solve for vector X at temperatures that are iteratively increased within the range 600° to 1,000°C (steps of 5°C increase). At each temperature-pressure condition, the solution vector was compositionally constrained to yield Mg# for olivine in the range 88 to 94 (Lee, 2003), the Mg# for orthopyroxene between 85 and 93 (e.g. Hacker & Abers, 2012), and the spinel proportion (Sp^*) lower than 8%, as suggested by xenolith data (Rodriguez-Vargas et al., 2005). Because the matrix of the compositional problem accepts constant values for Mg# and the spinel proportion, I set the code to iteratively try all possible combinations of given values for Mg# in olivine between 0.88 and 0.94 with steps of 0.02, Mg# for orthopyroxene between 0.85 and 0.93 with steps of 0.02, and spinel proportion between 0.00 and 0.08 with steps of 0.02.

The solution vector was then normalized to allow the sum of mineral proportions in vector X to yield 1. I consider a feasible setup for each event (endmember assemblage and temperature), those with a solution model (vector X) in which the proportion of garnet (Py) was not higher than 0.6 based on xenolith data (60%; Rodriguez-Vargas et al., 2005; Weber, 1998), the Mg# for olivine and orthopyroxene were within the previously mentioned ranges, and the differences in seismic speeds were lower than a given threshold in both waves, meaning: the absolute difference between the Pn and Sn velocity estimates from the two-station approach minus the VPn and VSn calculated by the Voight-Reuss-Hill average (e.g. Hacker et al., 2003). After trial and error, two thresholds were finally selected, 0.01 and 0.05 km/s. The low-value threshold (0.01 km/s) resembles with higher similarity the wave speed estimates from the two-station approach, yet the number of possible setups was very limited in the three regions. Consequently, a higher threshold (0.05 km/s) was also included in the analysis, which provided a higher number of setups in each region, yet with a higher residual with respect to the speed estimates from the two-station approach. The considered setups in this work are presented in Supplementary Material S3-2.

3.4.3.2 Phase equilibria approach (forward modeling)

For this approach, I used available bulk chemistry analysis from 17 documented mantle xenoliths brought to the surface by Plio-Pleistocene volcanism (Rodriguez-Vargas et al., 2005; Weber, 1998). For each available composition, I implemented a phase equilibria modeling in the Na_2O-CaO-MnO-FeO-MgO-Al_2O_3-SiO_2-H_2O system using the Perple_X software version 6.9.1 (Connolly, 2005). The considered thermodynamic dataset is that from Holland and Powell (1998) augmented with elastic moduli from Abers and Hacker

(2016). Solution models include, olivine, orthopyroxene, clinopyroxene, garnet, and spinel after Jennings and Holland (2015), and amphibole after Green et al. (2016). I run the models at a constant pressure of 2 GPa and varied the temperature and water content between 600°-1,000°C and 0.0-0.5 wt.% respectively (influencing amphibole stability).

Modal proportions of minerals and whole-rock seismic properties (Vp, Vs) were then extracted using the same software. Taking advantage of the fact that at each condition of temperature and water content the mineral assemblage is in equilibrium, the data was extracted in incremental steps of ~1°C and 0.01 wt.%. This resulted in a total of 340,000 different setups (mineral assemblage, water content, temperature, and seismic speeds) to compare.

I compared each of the Pn and Sn velocity estimates (two-station approach) with all possible setups obtained from the phase equilibria modeling. I consider a feasible setup for each event, those in which the absolute differences in seismic speeds were lower than 0.01 km/s in both waves, meaning: the Pn and Sn velocity estimates from the two-station approach minus the Vp and Vs from the phase equilibria modeling. The setups are presented in Supplementary Material S3-2.

3.5 Results

3.5.1 Pn and Sn velocity estimation

A total of 11,566 Pn velocity calculations were finally obtained, including 1,659, 1,541, and 8,366 estimates for the northern, gap, and southern regions respectively; they show a good inter-station azimuth coverage (Figure 3-2; Supplementary Material S3-1). Conversely, for Sn estimates a total of 746 calculations were finally obtained, including 485, 243, and 18 estimates for the northern, gap, and southern regions respectively (Figure 3-5; Supplementary Material S3-1). Something that draws attention is the reduced number of S-wave speed estimates for the southern region, which is linked to a reduced number of reported Sn picks in the ISC catalog. For example, for the northern region, a total of 12,455 Sn picks resulted in 485 Sn speed estimates; whereas for the southern region, available Sn picks were only 2,535. Consequently, the limited amount of Sn data restricts the analysis of velocities associated with this wave; nonetheless, since some information could be obtained, I included the data in this work.

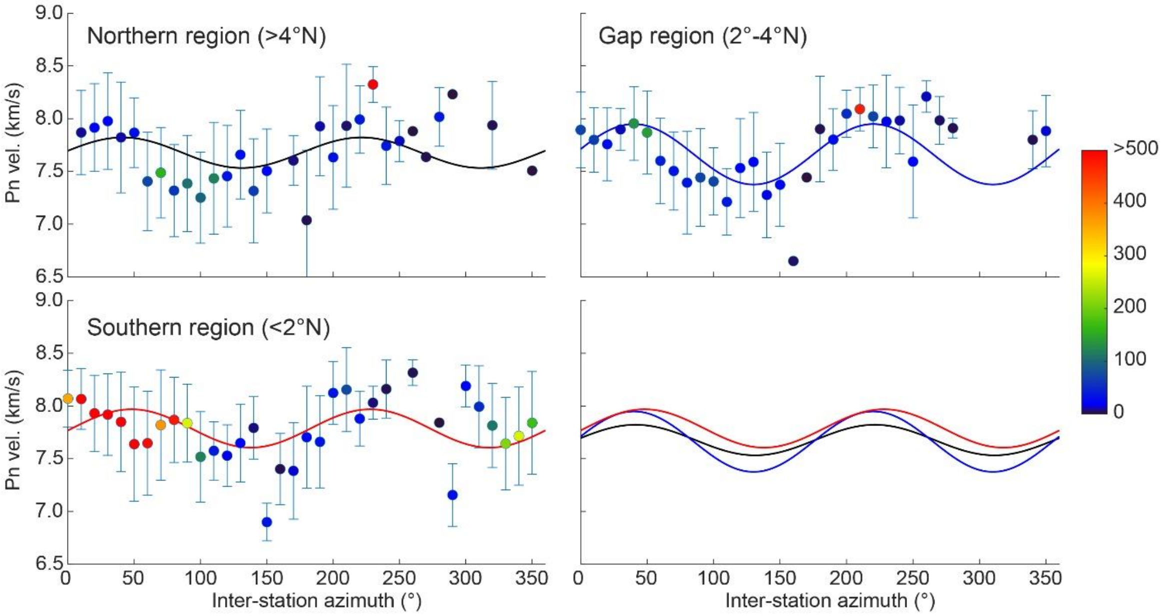

Figure 3-2. Pn velocity estimates variation with inter-station azimuth. Data includes all earthquakes with magnitudes >3. Each circle represents the mean Pn speed for a 10° bin in the inter-station azimuth; circles are colored according to the number of inter-station trajectories per azimuthal bin; error bars represent one standard deviation. Color lines are the fitted cosine function for each segment: Black for the northern region, blue for the gap, and red for the southern region.

Pn velocity estimates for the northern region vary between 6.51-8.49 km/s; for the gap, they vary between 6.52-8.48 km/s; and for the southern region between 6.50-8.50 km/s (Figure 3-2). When considering all the data (earthquakes with magnitudes >3), the distribution of inter-station azimuths suggests good coverage for all regions, lacking information for 310°, 330°-340°, and 360° in the northern region, for 290°-340° in the gap region, and 250° and 270° in the southern region (Figure 3-2). While using other magnitude thresholds (>4 and >5), the western azimuths (220°-330°) are the most affected by the reduction in the data (Figures 3-3 and 3-4).

As shown in Figure 3-2, the estimates describe a variation of Pn speeds with respect to the inter-station azimuth, suggesting an anisotropic uppermost mantle beneath all regions. The fast axis orientation (higher peaks in the fitted cosine function) seems to be similar for all domains, showing a NE-SW trend (trench-parallel orientation) (Figure 3-1).

To better depict the anisotropy of the mantle beneath the different regions, I cull the datasets by magnitude as described in the Methods section (Figures 3-2 to 3-4). When fitting the cosine function (Eq. 3-1), the different magnitude thresholds resulted in a small variation in the average speed (A coefficient), but larger differences in the coefficient related to the percentage of anisotropy (B coefficient) (Table 3-1). In this regard, the suggested average speeds from the fitted function are: 7.59-7.69, 7.64-7.66, and 7.79-7.81 km/s for the northern, gap, and southern regions (Table 3-1). These values suggest a mean velocity of 7.65 ± 0.04, 7.65 ± 0.01, and 7.80 ± 0.01 km/s, for each region correspondingly. Absolute values of B coefficients are between: 0.14-0.32, 0.15-0.29, and 0.08-0.26 for the northern, gap, and southern regions, suggesting an anisotropy percentage between 3.77-8.36%, 3.86-7.49%, and 2.04-6.54%, for each region (Table 3-1). A mean anisotropy percentage from these data yields: 6.07 ± 2.29%, 6.17 ± 1.33%, and 4.42 ± 2.13% for each of the mentioned regions correspondingly.

In terms of Sn velocity estimates, for the northern region, they vary between 3.79-4.99 km/s, for the gap between 3.75-4.97 km/s, and the southern region between 3.71-4.96 km/s (Figure 3-5). The inter-station azimuth for this wave is much more limited in all regions, lacking data mainly for 280°-360° azimuths in the northern region, whereas 0°-30° and 280°-360° are ill-sampled azimuths in the gap region. The southern region lacks several estimates comparable to the northern domains, and thus, a very restricted inter-station azimuth coverage is achieved with a very scattered pattern (Figure 3-5). Although the data associated with the southern region prevents a good analysis of the Sn velocity variation with the inter-station azimuth, the other regions (northern and gap) show a well-depicted change in the Sn speed with the varying azimuth (Figure 3-5). This is consistent with the anisotropic nature of the uppermost mantle suggested by Pn velocity estimates (Figures 3-2 to 3-4).

From the fitted cosine function, an average Sn velocity of ~4.41 km/s is suggested for the northern region, ~4.39 km/s for the gap region, and ~4.37 km/s for the southern region (Table 3-1). The last value includes a lot of uncertainty based on the strongly limited inter-station azimuth coverage (Figure 3-5). Anisotropy percentages using Eq. 3-2, suggest for the northern and gap regions values of ~3.21% and ~3.94% respectively (Table 3-1). For the southern region, the lack of azimuthal coverage prevents a reliable estimate of this parameter.

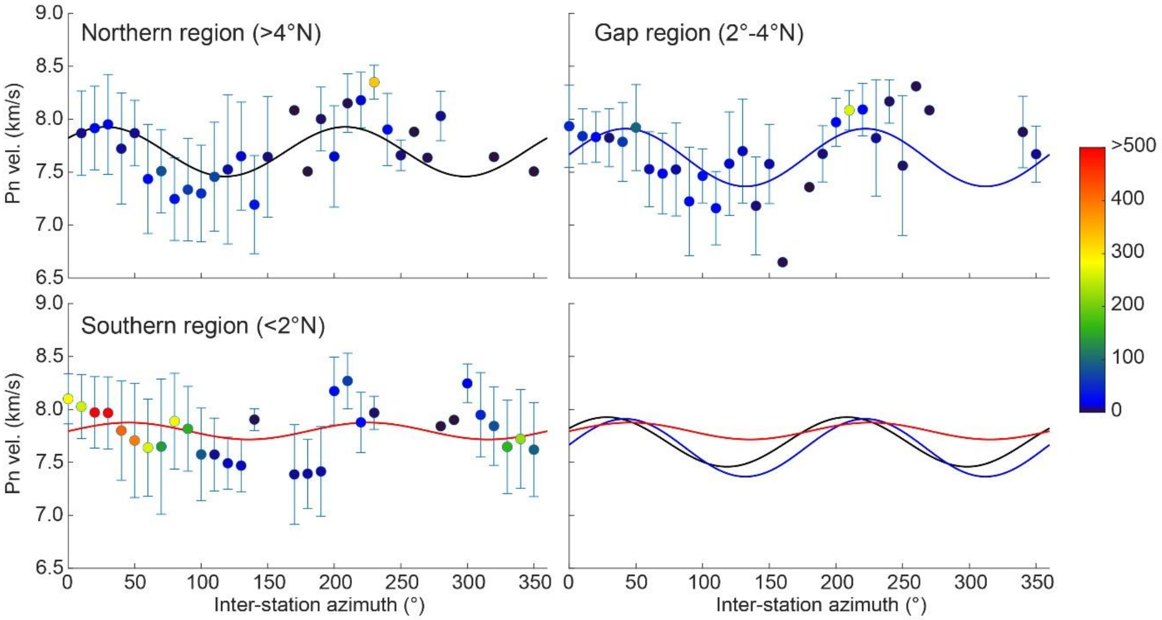

Figure 3-3. Pn velocity estimates variation with inter-station azimuth. Data includes all earthquakes with magnitudes $\geq$4. Other features as in Figure 3-2.

3.5.2 Thermo-compositional insights

In this section, I present some thermo-compositional inferences based on average speeds describing the uppermost mantle beneath the three regions of the arc, north of 4°N, the volcanic gap between 2°-4°N, and south of 2°N, respectively. A total of 60, 14, and 29 earthquakes were selected for the northern, gap, and southern regions, using criteria in section 3.4.3. Results include modeled seismic speeds resembling those obtained from the two-station approach, in the range 7.54-7.85 km/s for the P-wave and 4.35-4.58 km/s for the S-wave (Supplementary Material S3-2).

From the LSQR approach, a total of 14, 80, and 238 possible setups (combinations of temperature and endmember proportions) were considered feasible for the northern, gap, and southern regions, using the 0.01 km/s threshold (see sub-section 3.4.3.1 in the methods). Moreover, a total of 2,035, 2,475, and 3,522 plausible setups were obtained for the three regions when using the 0.05 km/s threshold (Supplementary Material S3-2). From the phase equilibria approach, a total of 13,864, 7,438, and 1,892 possible setups (temperature and mineral assemblage) were considered feasible for the northern, gap, and southern regions, respectively (Supplementary Material S3-2).

Using the LSQR approach, the two considered thresholds suggest a 25-75th percentile range between 965°-990°C (0.01 km/s threshold) and 800°-960°C (0.05 km/s threshold) for the northern region, with a median value of 975° and 875°C respectively (Figure 3-6). For those thresholds in the gap region, the percentile range shows values between 920°-975°C and 920°-980°C, with median values of 950° and 955°C correspondingly. For the southern region, values in the 25-75th percentile range are between 885°-965°C and 880°-965°C, with a 930° and 925°C median temperature for the respective thresholds (Figure 3-6). Conversely, using the phase equilibria approach, the 25-75th percentile range for the northern region is between 816°-936°C, with a median of 889°; for the gap region, the percentile range is between 694°-766°C, with a median of 721°C; and for the southern region, the range is between 627°-779°C, and a median of 753°C (Figure 3-6).

Compositionally, the LSQR approach suggests, based on the 25-75th percentile range, 83-88% (0.01 km/s threshold) and 82-89% (0.05 km/s threshold) of pyroxene for the northern region, between 53-58% and 54-91% of pyroxene (respective thresholds) for the gap region, while 68-74% and 61-71% of pyroxene (respective thresholds) for the southern region. The phase equilibria modeling suggests a 25-75th percentile range of pyroxene between 79-91%, 72-82%, and 34-79% for the northern, gap, and southern regions in that order (Figure 3-6). Regarding the amphibole content, the 75th percentile shows values of <1%, ~11%, and ~8% for the northern, gap, and southern regions using the LSQR approach (both thresholds), whereas ~15%, ~16%, and ~4% respectively, when using the phase equilibria modeling (Figure 3-6).

3.6 Discussion

From the results, two important constraints in the upper mantle wedge beneath the modern Northern Andes arc are well described: an anisotropic nature for the uppermost mantle, and lateral heterogeneity in wave speed and degree of anisotropy along the arc. Furthermore, these latitudinal differences in mantle properties seem to be related to some degree to a thermal controlling factor.

By using the coefficients from the function describing the variation in Pn speeds beneath the arc, dissimilarity in the average wave speed depicts the southern region as the fastest mantle beneath the arc (7.80 ± 0.01 km/s), whereas the northern (7.65 ± 0.04 km/s) and gap regions (7.65 ± 0.01 km/s) show slower mean velocities, yet similar values between those two (Figures 3-2 to 3-4; Table 3-1). Conversely, the percentage of anisotropy is higher in the northern (6.07 ± 2.29%) and gap regions (6.17 ± 1.33%), whereas lower for the southern region (4.42 ± 2.13%) (Table 3-1). I interpret these features as depicting a northward increase in anisotropy beneath the arc. Although the northern and gap regions show similar average percentages in anisotropy, the Pn velocity structure beneath the northern segment seems to be the most complex as suggested by a larger variation in the average Pn velocity (± 0.04 km/s) and anisotropy percentage (± 2.29 %) with respect to the gap region (± 0.01 km/s, ± 1.33%) (Table 3-1). The Sn speed estimates suggest no major differences along the arc (~4.37-4.41 km/s), yet caution must be taken given the large uncertainty in the mean estimate for the southern region (Figure 3-5).

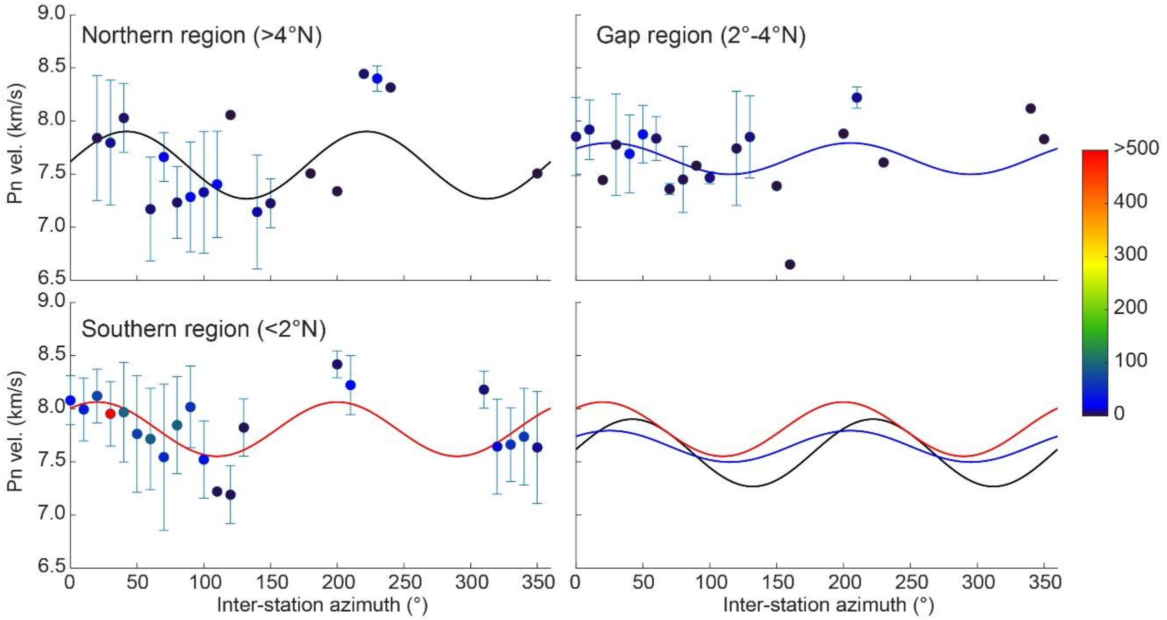

Figure 3-4. Pn velocity estimates variation with inter-station azimuth. Data includes all earthquakes with magnitudes ≥5. Other features as in Figure 3-2.

Regarding the fast axis orientation in the uppermost mantle beneath the arc (higher peaks in Figures 3-2 to 3-4), it is deemed similar for all regions, showing a NE-SW trend which is a trench-parallel orientation (Figure 3-1). This azimuth agrees well with the upper plate motion of the arc domain, which suggests a NE movement relative to stable South America (Mora-Páez et al., 2019). I consider it plausible that the agreement between the fast axis orientation based on Pn velocity estimates and the upper plate motion, which strongly involves strike-slip tectonics (Cortés and Angelier, 2005; Veloza et al., 2012), speaks in favor of a crystal-preferred orientation of mantle minerals that develop the observed anisotropic pattern (Collins and Molnar, 2014; Vauchez et al., 2012). As shown by the compositional modeling (Figure 3-6), pyroxene seems to be playing a major role in the composition of the layer through which the waves travel. Thus, the crystal preferred orientation might be a consequence of both, olivine, and pyroxene alignment (Bernard et al., 2021; Mainprice, 2015).

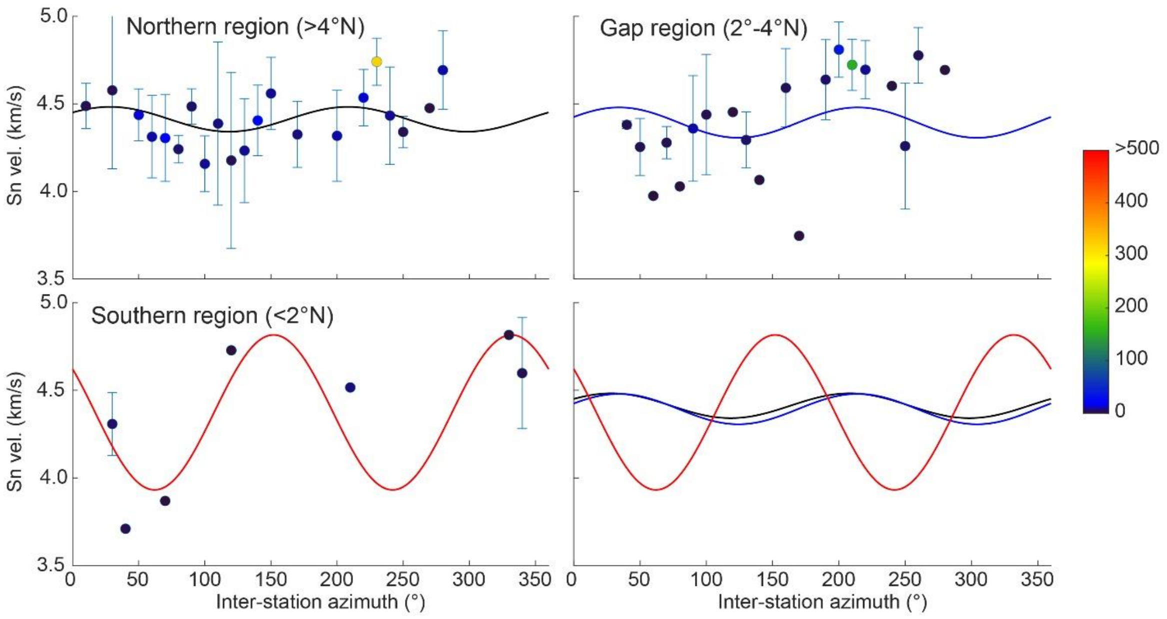

Figure 3-5. Sn velocity estimates variation with inter-station azimuth. Data includes all earthquakes with magnitudes >3. Other features as in Figure 3-2.

Another source of anisotropy could be the presence of preferential alignment of melt (Hammond et al., 2014; Mainprice, 2015), which is a feasible factor for the study region. However, as shown by the Sn average velocities of 4.37-4.41 km/s (Table 3-1), they agree with mantle speeds (>4.3 km/s; Mooney, 2021) rather than showing a strong reduction, as expected when considering the presence of melt (Hammond and Humphreys, 2000). Thus, I do not neglect a possible contribution of aligned melt to the anisotropy, but I favor the preferred orientation of olivine and pyroxene as the main controlling factor. Further research is needed in this regard, to better understand the mineral-anisotropy relationship of the uppermost mantle beneath the Northern Andes arc.

From the thermo-compositional modeling, the LSQR approach seems to be biased towards higher temperatures, failing to detect substantial differences between the regions (Figure 3-6). On the other hand, when considering the possible temperatures from the phase equilibria modeling, which I consider more reliable than LSQR since it uses mineral proportions at equilibrium based on bulk chemistry from documented xenoliths, it can be seen that the mantle beneath the northern region is suggested as the warmest (816-936°C; Figure 3-6). Therefore, I interpret that there should be a thermal contribution to lowering the uppermost mantle wave speeds and augmenting the anisotropy beneath the northern region.

Temperature estimates for the upper mantle beneath the volcanic gap (694°-766°C) and southern region (627°-779°C) from the phase equilibria modeling, suggest lower values with respect to the northern region. The gap and southern regions show a similar 25-75th percentile temperature range which makes it difficult to discern any difference between them (Figure 3-6). If one considers, for instance, the faster speeds obtained for the southern region, it might be a consequence of a colder thermal state compared to the gap region, yet this is speculative and further research is required to prove this hypothesis. Thus, from a general perspective, I suggest an increase in the mantle temperature from the southern and gap regions towards the north, based on the higher temperatures obtained for the region north of 4°N.

In terms of composition, major differences in the pyroxene content along the arc are not well-depicted by any of the considered approaches (Figure 3-6). However, both methods suggest that pyroxene plays a major role in the mineral assemblage, describing the uppermost mantle as pyroxene-rich with possible proportions between 53-91% based on LSQR, and 34-91% on phase equilibria (Figure 3-6). Furthermore, as evidenced by the proportions obtained for amphibole, both approaches show the involvement of a hydrous phase within the uppermost mantle for all the regions. From LSQR and phase equilibria, amounts of amphibole might be between 0-16% (Figure 3-6), which I interpret as a hydrated uppermost mantle below the entire arc (including the gap region).

High pyroxene content coupled with amphibole-bearing assemblages is consistent with recovered mantle xenoliths brought to the surface by modern arc products, showing a high proportion of websterites (Rodriguez-Vargas et al., 2005; Weber, 1998). I consider this feature as related to the interaction between hydrous primitive arc melts with the uppermost mantle, in which high-pressure fractionation (cumulates) can take place and results in the formation of high-MgO pyroxenites (Lee et al., 2006). The development of a layer composed of high-MgO pyroxenites in the vicinity of the Moho (crust-mantle transition) is an important feature in the structure of continental arcs (Ducea et al., 2021b; Erdman et al., 2016; Lee et al., 2006). I propose that the Pn and Sn waves are majorly traveling through this layer of websterites (high-MgO pyroxenites).

3.6.1 Tectonic implications

The results of the velocity estimates and thermo-compositional approach, agree with an increase in temperature and anisotropy from south to north. If correct, this pattern should be connected with the tectonic setting of the arc. Limiting the northern arc expression lies the Caldas tear, through which a flux of hot buoyant sub-slab asthenosphere can be prompted (Abratis and Wörner, 2001; Castellanos et al., 2018). Such a scenario can explain to some degree the warmest thermal structure and the stronger anisotropy beneath the northern region, in which both parameters are strongly influenced by the incoming material through the tear (see also Porritt et al., 2014).

Conversely, the southern region shows a spatial correspondence with the continuation of the still subducting Carnegie ridge that has been considered as the cause for a flattened slab architecture in this part of the orogen (Gutscher et al., 1999). If one considers the shallowing of the slab as a process that enhances the cooling of the upper plate (Gutscher et al., 2000; Wagner et al., 2005), the inferred lower temperature of the southern mantle with respect to the northern region, might be related to this mechanism. Lowering the temperature in the lowermost crust and uppermost mantle can therefore prompt faster wave speeds, such as those obtained for the southern region (Figure 3-2). Therefore, I suggest an intimate relationship between the subduction of the Carnegie ridge and the lower temperatures and faster upper mantle seismic speeds at this location. Moreover, under this setting of relatively shallow subduction, one would expect the volcanic expression on the surface to become wider (Gutscher et al., 2000, 1999), as observed in the southern region showing a >120 km-wide-arc with respect to a <75-km-wide expression to the north (Figure 3-1).

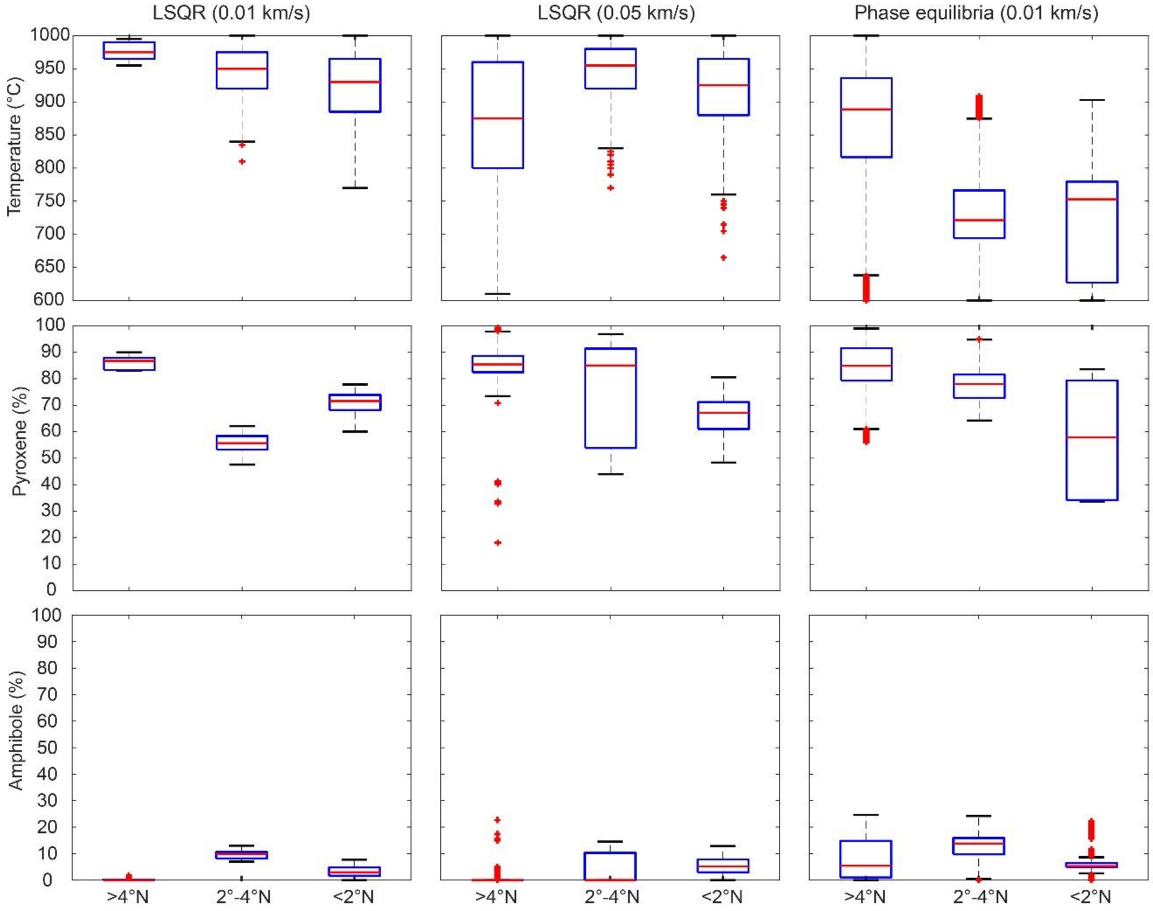

Figure 3-6. Boxplots of temperature (upper panel) and composition representing pyroxene (middle panel) and amphibole content (lower panel) beneath the modern arc: the northern region (>4°N), the volcanic gap (2°-4°N), and the southern region (<2°N). These calculations integrate all the plausible setups (temperature, mineral content) determined from individual earthquakes, using the LSQR and phase equilibria approaches with the residual thresholds given in parenthesis (see Supplementary Material S3-2). The red line within each box represents the median, while the extent of the boxes is bounded by the 25-75th percentiles. The length of whiskers was specified as 1.5 times the interquartile range, and the outliers are represented by red crosses.

The volcanic gap, on the other hand, shows an intermediate state between the northern and southern regions. It shows similar seismic speeds and anisotropy to the northern mantle, yet similar inferred temperatures when compared to the southern region. If one considers the possibility of the proposed Malpelo (Idárraga-García et al., 2016) or Northern tear (Gutscher et al., 1999) to be affecting the volcanic gap, the anisotropy obtained for the gap region can be explained by hot material influx. However, under this scenario one would expect higher temperatures rather than a cold state; the lower temperatures suggested for this region complicates this interpretation. Consequently, if we assume the presence of the tear as correct, some contribution to anisotropy might be obtained from a small amount of material influx; this allows the generation of fabric, and therefore anisotropy, yet its temperature and the volume of the incoming material should be insufficient to strongly modify the thermal state in the mantle wedge.

Something that draws attention, however, is the abrupt reduction of surface volcanism within this region. For explaining this feature, as well as the lower temperature with respect to the north, I think that it might be related to the absence of magmatic pounding at the base of the arc. If correct, one can speculate about the possibility of magmatic accumulation at the base of the crust in a position shifted from the arc axis. This scenario can be prompted by a thermal cooling of the fore-arc mantle that reduces the ‘pinch zone’ in a similar manner as that suggested for the Denali volcanic gap (e.g. Rondenay et al., 2010). This process triggers a drop in mantle temperature, which is consistent with the lower temperatures yielded for the gap region in reference to the north. Although a cool mantle setting is feasible beneath the volcanic gap, detailed seismic approaches must be taken to confirm this hypothesis.

3.7 Conclusions

The segmented arc in the Northern Andes shows a narrow northern volcanic segment (<75 km wide) between 4°-6°N, a volcanic gap in its central region ~265 km long between 2°-4°N, and a southern wider arc expression (>120 km) between 2°S-2°N, which are likely related to the underlying mantle wedge heterogeneity. Calculated uppermost mantle Pn and Sn wave speeds beneath the arc, suggest a dissimilar seismic structure, with a slower, more anisotropic, and warmer mantle beneath the northern region, and a faster and colder mantle beneath the southern region. The mantle beneath the northern region is the most complex, as suggested by a larger variation in average wave speeds and percentage of anisotropy; this is possibly influenced by the Caldas tear, which might be triggering hot mantle influx that explains to some degree the higher temperatures. The signal from the volcanic gap supports a colder thermal structure yet a similar anisotropy percentage compared to the northern region. I interpret a lack or a limited amount of magma pounding at the Moho vicinity beneath this region, as the main cause for the strong reduction in surface volcanism and low temperatures in the uppermost mantle. For the anisotropy, I do not neglect a possible influence by mantle influx through the Malpelo-Northern tear, yet it should be limited in volume to keep a colder thermal state compared to the north. The mantle beneath the southern region is the fastest, consistent with lower temperatures and anisotropy with respect to the north. I interpret these features to be influenced by the subduction of the Carnegie ridge, which triggers a shallow subduction setting that cools the upper plate, increases the seismic speeds, and widens the volcanic expression.

The wave speed estimates, and thermo-compositional approach draw a broad increase in temperature and anisotropy coupled with lower seismic speeds, from south to north along the Northern Andes magmatic arc. Such heterogeneity seems to be controlled by tectonic features affecting the different regions along strike, including the presence of multiple slab tears to the north, and the still subducting Carnegie ridge to the south. Although I do not neglect the contribution of aligned melt, I favor the preferred orientation of olivine and pyroxene as the main controlling factor of the anisotropy, which might be associated with the strike-slip tectonics of the region as well. The observed NE-SW fast axis below the entire arc agrees well with the sense of plate motion, suggesting an additional mechanism contributing to the anisotropic fabric; the latter points towards a possible linkage between the crustal deformation and the underlying mantle anisotropy that requires further research.

3.8 Publication or submission

This paper is under review in the *Journal of South American Earth Sciences*. Co-authors in this paper are: Monsalve, G. and Sánchez, J. J.

3.9 Acknowledgments

I thank S. León and G. Posada for discussions about the Northern magmatic arc, its evolution, and available geophysical and geological constraints within the area. Comments and suggestions by editor C. Montes and two anonymous reviewers for an earlier version improved this work. This work was supported by the Fundación para la Promoción de la Investigación y la Tecnología (Project 4.634).

4. Arclogite nature of the Colombian Andes magmatic arc root: A receiver-function approach

4.1 Summary

Arclogites are an important part of the continental arc root architecture. When overlooked, the crustal structure could be misinterpreted, assuming that the seismically defined Moho necessarily coincides with the crust-mantle boundary. Evaluating the possible presence of lower crustal rocks below the seismic Moho with physical properties resembling those of the underlying mantle, is, therefore, of major importance. Through a multi-approach receiver function assessment, which includes shear wave velocity inversion, and determination of plausible crustal seismic velocity distributions from forward modeling, I present new constraints on the seismic structure of the arc root beneath the Colombian Andes magmatic arc. Results suggest a high-velocity arc root with a latitudinal variable thickness, from 13.5 to 20 km. The arc root is composed of a 4 to 6 km thick upper domain with seismic wave speeds 5% slower, and 8.5 to 14 km thick lower domain 5% faster, relative to the underlying uppermost mantle. This lower crustal structure, coupled with documented garnet pyroxenitic xenoliths, supports an arclogite nature for the Colombian Andes arc root.

4.2 Introduction

Magmatic arc roots can contain a major amount of garnet pyroxenites that represent the deep ultramafic material that complements the shallower granitoid batholiths and andesitic to dacitic volcanic rocks (Ducea et al., 2021b; Lee and Anderson, 2015). These pyroxenites referred to as arclogites, are formed as residues from partially melted restites and/or magmatic cumulates, which equilibrate at high-pressure conditions at the base of continental arcs (Anderson, 2005; Ducea et al., 2021a, 2021b; Lee and Anderson, 2015).

From a seismological perspective, they play an important role in defining the crustal structure, since their seismic properties resemble those of the underlying mantle, resulting in an offset between the seismic Moho and the crust-mantle boundary (Ducea et al., 2021b; Erdman et al., 2016). Therefore, when arclogites are overlooked, the lower crustal structure could be easily misinterpreted, with a sharp seismic Moho that coincides with the crust-mantle boundary. Instead, it could be a transitional structure that includes the presence of lower crustal rocks below the seismic Moho, characterized by faster seismic speeds relative to the underlying mantle (Bowman et al., 2021; Cook et al., 2010; Ducea et al., 2021a; Erdman et al., 2016; Mahan et al., 2012).

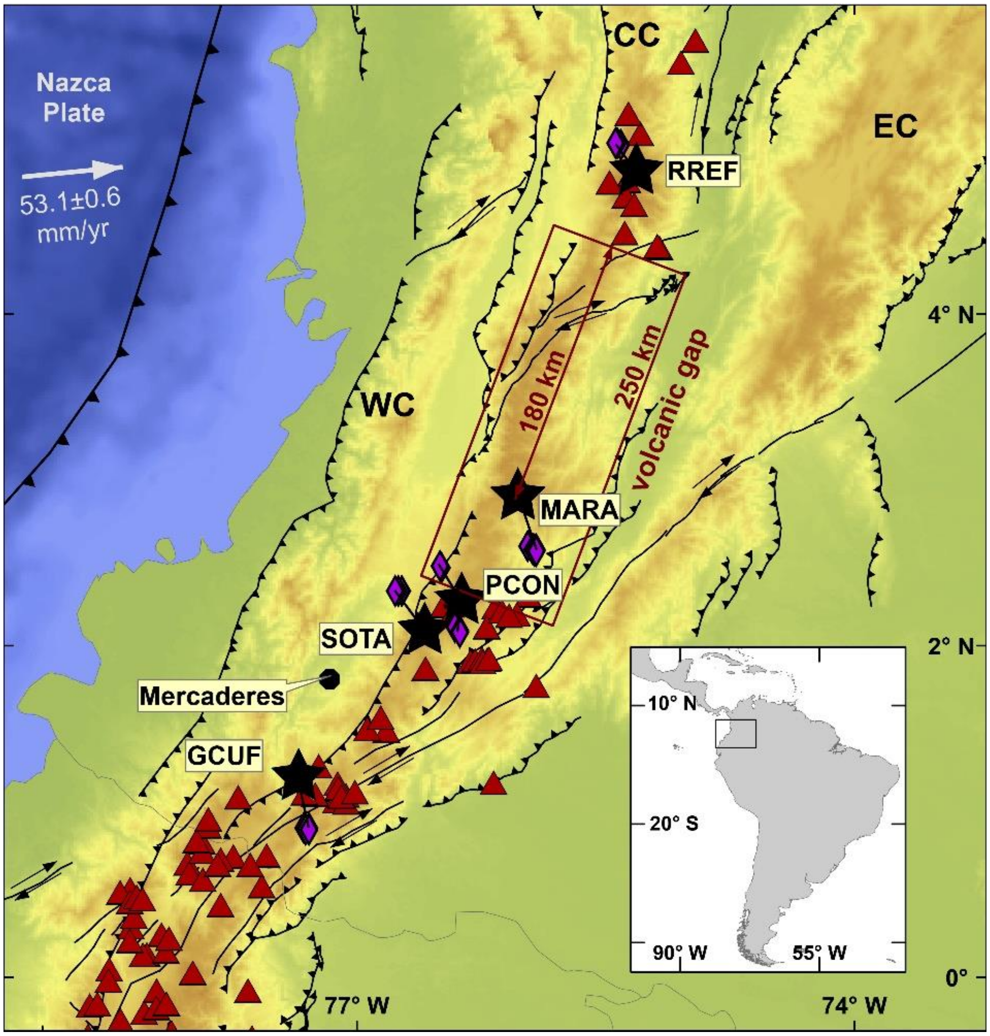

Figure 4-1. Map view of the study area with the main tectonic features. Northwestern Andes modern volcanic centers are represented by red triangles and seismic stations are depicted by black stars on top of five of the main active volcanoes: Nevado del Ruiz (RREF), Nevado

del Huila (MARA), Puracé (PCON), Sotará (SOTA), and Galeras (GCUF). Piercing points from the azimuthally restricted analysis are shown as purple diamonds. The volcanic gap in the central portion shows a reduction in surface volcanism for around 250-265 km along the arc; see Monsalve-Bustamante (2020) for some spatial considerations about this gap. Mercaderes locality is shown since lower crustal xenoliths classified as true arclogites have been documented at this site (Bloch et al., 2017; Ducea et al., 2021b; Weber et al., 2002). WC, CC, and EC stand for Western, Central, and Eastern Cordillera, respectively. Convergence rate of the Nazca plate with respect to stable South America after Mora-Páez et al. (2019).

From a geodynamic standpoint, the mineral assemblage of arclogites allows them to become denser than the surrounding mantle. This density contrast may trigger a tectonic cycle that includes crustal thickening, lithospheric foundering, arc root delamination, vertical crustal motion, and subsequent crustal structure and topography readjustments (Lee, 2014). The seismic structure of the lower crust to mantle transition, is consequently, of major importance to properly define lithospheric structure, geochemical and tectonic evolution, and topographic responses in continental arcs (Currie et al., 2015; Ducea et al., 2021a; Lee and Anderson, 2015; Tang et al., 2019).

In this regard, the crust-mantle transition along the Colombian magmatic arc is of great importance since it is the only known active segment along the Andes that contains a xenolith locality (Figure 4-1), with garnet pyroxenites that are properly defined as arclogites (Ducea et al., 2021b). Notwithstanding, research on this transition remains poorly explored. Some insights have been provided from petrochemical and density modeling of recovered lower crustal xenoliths (Bloch et al., 2017; Rodriguez-Vargas et al., 2005; Weber et al., 2002); from along strike Moho depth variations from receiver function analysis (Poveda et al., 2015) and from gravity inversion (chapter 2); from constraints on the seismic structure within the uppermost mantle from Pn and Sn waves (chapter 3); and estimates of temperature distribution beneath the arc (chapter 3; Vargas et al., 2019). Even though xenoliths have been documented in only one locality (Mercaderes, Figure 4-1), they suggest the presence of a mafic lower crust composed of variable mineral assemblages, including a large proportion of high-density rocks (garnet pyroxenites) (Bloch et al., 2017; Weber et al., 2002). On the other hand, the analysis of receiver functions and gravity data inversion, for recovering the Moho depth, has shown a latitudinal variable crustal thickness along the arc with an average between 45-55 km (chapter 2; Poveda et al., 2015). To the south of our study region (Figure 4-1), values of ~60 km or more have been suggested as plausible (chapter 2; Poveda et al., 2015). The thicker crust towards the south is in agreement with receiver function constraints in the Ecuadorian modern arc, depicting crustal thicknesses up to 55-65 km (Koch et al., 2021). Although these approaches provide some clues on the lithospheric architecture, the nature of the arc root and its transition to the uppermost mantle has not yet been properly addressed.

In this chapter, I present new constraints on the seismic structure of the arc root and the underlying crust-mantle boundary along the Colombian Andes. I used receiver functions from five seismic stations on top of the main active volcanoes within the arc. A multi-method approach, including azimuthal analysis, shear wave velocity inversion, S-wave velocity modeling using available bulk chemistry from xenoliths, and determination of crustal structure from forward modeling, support the existence of a high-velocity arc root with a latitudinal variable thickness. Forward modeling is consistent with a ~13.5 to 20 km thick arc root composed of a 4 to 6 km thick upper domain with seismic wave speeds 5% slower, and 8.5 to 14 km thick lower domain 5% faster, relative to the underlying uppermost mantle. This lower crustal architecture, coupled with documented garnet pyroxenitic xenoliths, supports an arclogite nature for the Colombian Andes arc root and a depth mismatch between the seismic Moho and the crust-mantle boundary of about 8.5-14 km.

4.3 Data and Methods

4.3.1 Teleseismic receiver-function calculations

Data was obtained from the Colombian Geological Survey (In Spanish *Servicio Geológico Colombiano*), and includes seismograms recorded by the National Seismological Network of Colombia and different volcano observatories (Observatorio Vulcanológico y Sismológico de Popoyán; Observatorio Vulcanológico y Sismológico de Pasto; Observatorio Vulcanológico y Sismológico de Manizales). Teleseismic events were analyzed for five stations on top of the main active volcanoes in the Colombian Andes magmatic arc, using records between 2008 and 2015. From north to south (Figure 4-1) the stations are: RREF at Nevado del Ruiz (4.90°N, 75.35°W), MARA at Nevado del Huila (2.82°N, 75.95°W), PCON at Puracé volcano (2.33°N, 76.40°W), SOTA at Sotará volcano (2.14°N, 76.61°W), and GCUF at Galeras volcano (1.23°N, 77.35°W). Seismic events were chosen with magnitudes higher than 5.5 and epicentral distances between 30°-90°.

Individual seismic waveforms were inspected to guarantee high-quality traces with a well-depicted P-wave arrival and high signal-to-noise ratios.

Since I focus on the deep crust, seismic Moho, and crust-mantle boundary structure, P to S radial receiver functions were computed (Owens and Zandt, 1985; Schulte-Pelkum and Mahan, 2014). The original waveforms were cut 10 s prior to and 35 s after the initial P-wave arrival; the receiver functions were computed through the iterative time-domain deconvolution technique (Ligorría and Ammon, 1999) using the Computer Programs in Seismology package (Herrmann, 2013). A bandwidth factor of 5.0 was used (Gaussian parameter 'a' in the deconvolution terminology), which corresponds to a low-pass filter with a frequency of 2.4 Hz (e.g. Monsalve et al., 2019). After the computation of radial receiver functions, the traces were inspected for quality control (Schulte-Pelkum and Mahan, 2014), rejecting those with a non-positive first arrival. Azimuthal stacking (10° bins) was applied after a move-out correction that equalized the traces to a slowness of 0.06 s/km.

The number of receiver functions finally considered in this work at stations RREF, MARA, PCON, SOTA, and GCUF are 63, 24, 34, 46, and 31, respectively. The stacking diagrams of those traces are presented in two ways: as a plot considering all traces, and as a plot removing stacks with only one trace (Figure 4-2); this facilitated the identification of major interfaces. Regarding the Pms interface (seismic Moho), it was manually picked at what I considered the best delay time representing the "alignment" of the positive polarities between 5-8 s in the entire back-azimuth range.

As it will be discussed, a shallow interface was inferred beneath stations at delay times ranging from 0.7 to 1.0 s, and negative polarity is depicted at ~1.6 to 2.6 s (Figure 4-2). To make sure that later P to S conversions are not confused with reverberations in the layers associated with these upper crustal conversions, I computed synthetic receiver functions using the Computer Programs in Seismology package (Herrmann, 2013). Crustal structure in synthetic tests considered a constant thickness of 50 km above a half-space mantle, which is a reasonable average thickness estimate for the Colombian volcanic arc (chapter 2; Poveda et al., 2015). Seismic velocities for eight different crustal setups, which are presented in Table 4-1, were based on Ojeda and Havskov (2001) and Brocher (2005).

For the computation of synthetic receiver functions, I preferred to use a 50 km thick crust as a representative value for the arc, instead of considering an individual thickness for each station. This decision was made based on the fact that there is a range of possible values for each site that can be evaluated based on available estimates (chapter 2; Bloch et al., 2017; Poveda et al., 2015); if I consider an average receiver function crustal thickness estimate beneath a station, one will find that the average h-k stacking estimate differs from the average Wadati diagram estimate (Poveda et al., 2015). Additionally, the average values from Poveda et al. (2015) might be underestimated beneath some of the used stations, as other constraints have suggested (chapter 2; Bloch et al., 2017).

4.3.2 Shear wave velocity inversion

Shear wave velocity profiles beneath a seismic station can be inverted for a given mean receiver function with a given ray parameter. Using a mean receiver function from an azimuthally restricted analysis (described below) guarantees a robust signal since I am considering mutually correlated traces that represent very constrained ray paths, due to restrictions imposed on back-azimuths and ray parameters. Because the inversion uses a restricted range of data for each station, the influence of anisotropy or dipping interfaces cannot be examined (Fontaine et al., 2013; Tkalčić et al., 2011), and consequently, those effects are not addressed in this work.

4.3.2.1 Azimuthally restricted analysis

To obtain a mean receiver function that can be used to invert velocity models, I applied a methodology based on Fontaine et al. (2013), which considers only mutually correlated radial receiver functions showing a similar ray parameter and back-azimuth. The method consists of four main steps: (1) extracting only traces from the azimuthal quadrant with the highest number of receiver functions, (2) estimating the median ray parameter from those traces, (3) selecting receiver functions with ray parameters similar to the median; I used a ray parameter range of ± 0.006 s/km around the median after analyzing the dataset, and (4) stacking the best traces from the previous step. The best traces are selected after a cross-correlation analysis; a detailed description is given in Fontaine et al. (2013) and Tkalčić et al. (2011).

To systematically select the traces, I normalized to unity the amplitude of the receiver functions obtained from step three (3) before conducting the cross-correlation. A receiver function was selected when yielding a correlation coefficient equal to or greater than 0.70

with at least three different traces. Normalized receiver functions with amplitudes higher than 0.5 times the amplitude of the first P-wave arrival were not included in the final computed mean receiver function to minimize crustal complexity. This approach can be thought of as computing a mean receiver function that depicts the seismic structure beneath a station through a restricted ray path. I applied such analysis to the two back-azimuth quadrants with the highest number of traces in all stations (NW and SE quadrants, see Figure 4-2). Only the PCON station provided mutually correlated traces for the two quadrants, but at least one quadrant was accomplished for each station (Figure 4-6). Piercing points (approximate intersections between seismic rays and the Moho) associated with the mutually correlated traces are shown in Figure 4-1; I used the TauP software (Crotwell et al., 1999) and the IASP91 model (Kennett and Engdahl, 1991) for these calculations.

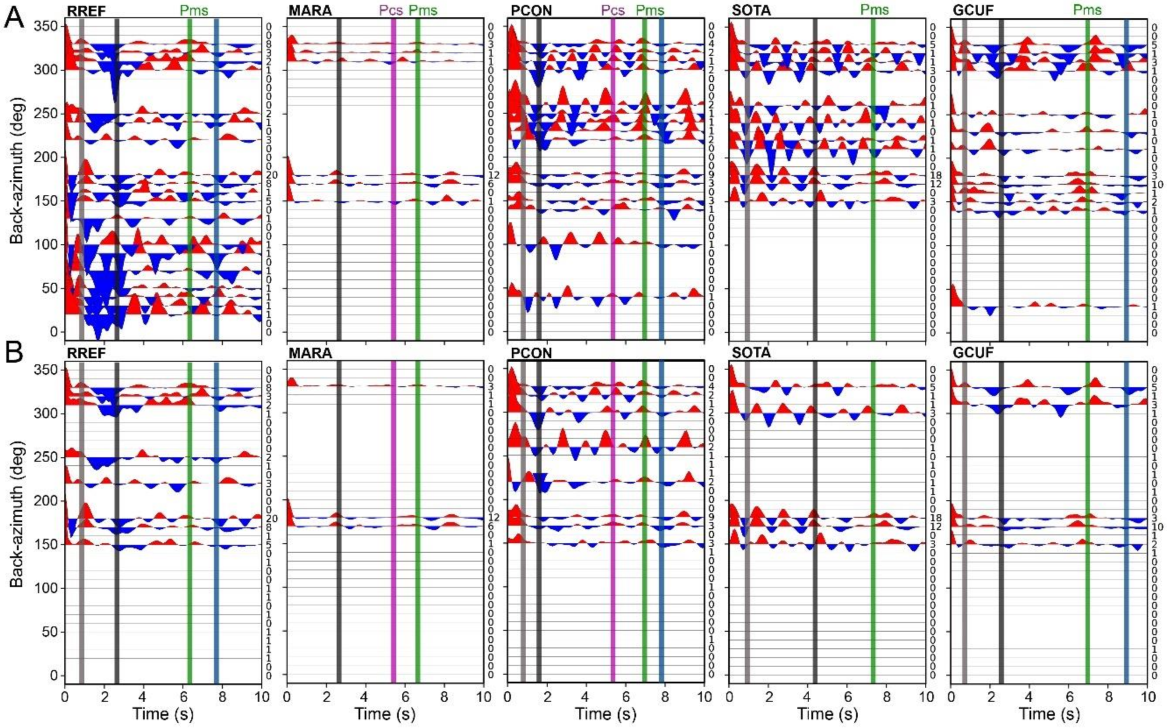

Figure 4-2. Receiver functions beneath the 5 analyzed seismic stations, stacked by back-azimuth with 10° bins. The number of stacked receiver functions is shown to the right of each diagram. The upper panel shows all stacks (A); the lower panel shows only those stacks that have more than one trace (B). Possible major discontinuities depicted in colors: grey lines for two interfaces in the upper-mid crust, magenta lines for an intra-crustal discontinuity (referred to in the text as Pcs), green lines for the seismic Moho (Pms) based on receiver functions and guided by arrival times given in Poveda (2013), and blue lines for a negative polarity interface at larger delay times with respect to Pms. Notice that Pcs

(magenta lines) are only constrained below MARA and PCON stations, whereas the interface corresponding to the negative polarity (blue lines) is only clearly suggested beneath RREF, PCON, and GCUF.

4.3.2.2 Inversion of velocity models

For inversion of the mean receiver functions computed from the previous approach, I used the *rftn96* program from the Computer Programs in Seismology package (Herrmann, 2013). It uses a linearized iterative approach in the time domain yielding shear wave velocity for layers with a fixed thickness (Ammon et al., 1990). The damping factor, controlling the trade-off between receiver function fitness and velocity structure smoothness, was set to 0.5 after trying multiple values (Ammon et al., 1990; Motaghi et al., 2017).

An important issue in the time domain inversion is the initial crustal model, which needs to be as close as possible to the true velocity model; thus, a-priori information must always be included (Ammon et al., 1990). I used the shear wave velocity structure from the available ambient noise tomography beneath the arc (Poveda et al., 2018) as the starting model. Inverting the receiver function from an initial reference model based on surface waves has been considered a good approach for the linearized inversion scheme (Feng et al., 2017). As suggested by Feng et al. (2017), inversion of receiver functions using surface wave constraints as the initial model yields better results than a joint inversion of receiver functions and surface wave dispersion. Even though this consideration might be debatable (e.g. Julià et al., 2000), I followed this approach and invert the receiver functions using surface wave data as a priori information (described below). This procedure overcomes the limitation inherent in surface wave data extracted from ambient noise, discussed by Poveda et al. (2018), which is reliable for the first 35-40 km of the crust.

Because the code uses a finite number of layers with fixed thicknesses composing the lithosphere, I tried different constant thickness values of 10, 5, 2.5, and 2 km. After trial and error, the final lithospheric configuration beneath all stations was set to a 2.5 km thick shallowest layer, a 40 km thick upper-middle crust composed of 8 layers with a thickness of 5 km each, a 40 km thick lower crust and uppermost mantle composed of 8 layers with a thickness of 5 km each, and a half-space mantle underlying the stratified model. S-wave velocity structure for the starting models of the upper and middle crust (first 42.5 km) was set to values from the ambient noise tomographic model of Poveda et al. (2018), whereas the associated P-wave velocity was estimated from available Vp/Vs ratios associated with the stations based on local seismic data using Wadati diagrams (Poveda et al., 2015). Taking into account that the tomographic model used as the initial velocity structure (Poveda et al, 2018) lacks information for the lower crust, seismic speeds at layers representing the lower crust and uppermost mantle were set to constant values resembling only mantle properties, to prevent a biased lower crust resulting model. More than 2,500 different starting values were tried at each station, by considering the possible combinations of an S-wave velocity ranging 4.3-5.0 km/s, a P-wave velocity between 7.8-9.0 km/s, and step increments of 0.02 km/s in both cases.

The resulting models were then filtered to only consider the ones showing a fit percentage higher than 60%, using the residual between the observed and predicted receiver functions, and such that the S-wave speeds in the shallowest 10 km of the mantle are as close as possible to a range of Sn speed estimates derived from chapter 3. Taking into account the non-uniqueness of the inversion approach (Ammon et al., 1990), for each station, I plot the 10 models with the best receiver function fit (blue lines in Figure 4-7), and the 10 models with the best “crustal fit” (upper-middle crust with the lowest velocity residual with respect to the tomographic model; green lines in Figure 4-7). The “crustal fit” models were incorporated since the tomography from Poveda et al. (2018) lacks information on the velocity structure beneath 40 km depth. Thus, these “crustal fit” models include the upper and mid-crustal structure that agrees best with the tomography estimates, and different possibilities for the lower crust. From these 20 models, an average velocity structure was constructed by merging layers with similar velocities, which resulted in fewer and thicker layers describing the upper lithosphere beneath each station. The velocity in each resulting layer was set to the average of seismic speeds from the merged layers. A simplified model (red lines in Figure 4-7) was then computed by a second inversion using the layers that resulted from this average velocity structure as the initial setup, aiming to reduce the over-parametrization due to the number of layers. All models, which include the 10 best receiver function fit models, the 10 best “crustal fit” models, and the simplified model, were used to define a velocity range within a given depth interval for the first 70 km of the lithosphere (Figure 4-7).

4.3.1 Phase equilibria modeling of xenoliths

As it will be discussed, fast velocities are suggested for the lowermost part of the crust beneath the modern arc. To envision a feasible S-wave velocity for the arclogites documented in the xenolith locality (Figure 4-1), I used the bulk chemistry from 10 garnet pyroxenite xenoliths reported by Bloch et al. (2017) and Weber et al. (2002), in order to model the S-wave speeds using the Perple_X software version 6.9.1 (Connolly, 2005). Phase equilibria modeling was conducted in the Na_2O-CaO-MnO-FeO-MgO-Al_2O_3-SiO_2 system, considering the thermodynamic dataset of Holland and Powell (1998), augmented with elastic moduli from Abers and Hacker (2016). Solution models include, garnet and orthopyroxene after White et al. (2014), clinopyroxene after Green et al. (2007), amphibole after Green et al. (2016), and feldspar after Holland and Powell (2003). The modeling was conducted at a constant pressure of 2 GPa and temperatures between 650°-1,200°C (Bloch et al., 2017; Bowman et al., 2021; Weber et al., 2002). The S-wave speed estimates and the composition of the used xenolith samples are presented in Supplementary Material S4-1.

4.4 Results

4.4.1 Teleseismic receiver functions

In this section, I describe major horizontal interfaces that are well-depicted by receiver functions using stacked traces from all back-azimuths (Figure 4-2). Although the major goal is the deep crust and uppermost mantle, I report possible discontinuities within the upper-middle crust as well. Descriptions are addressed from the surface downwards.

Two interfaces are observed within the upper-mid crust beneath all stations (gray lines in Figure 4-2); the shallowest interface (light gray lines in Figure 4-2) shows delay times between 0.7-1.0 s with respect to the first P-wave arrival, and shows positive polarity beneath RREF, PCON, and GCUF, whereas a negative polarity at SOTA station (see Figure 4-1 for station locations). MARA receiver functions do not clearly show this shallow discontinuity, although the poor back-azimuth coverage limits this observation.

The second interface is constrained at all sites but with differences in the delay times beneath each station (dark gray lines in Figure 4-2). At RREF, MARA, and GCUF, the possible discontinuity is detected at around 2.6 s, beneath PCON is at around 1.6 s, and beneath SOTA at around 4.4 s. The polarity of this discontinuity also varies among stations: beneath RREF, PCON, and GCUF it is negative, whereas below MARA and SOTA it is positive.

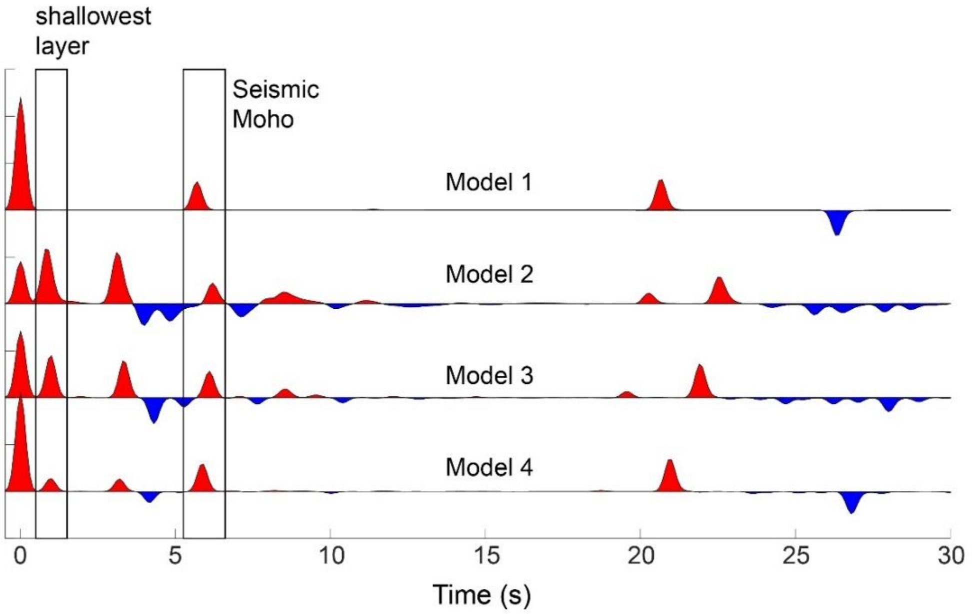

Figure 4-3. Reverberation in the shallowest layer considering different crustal structures described in Table 4-1. Model 1 represents a reference model with no shallow crustal layer.

The deep crust shows a well-depicted interface at a delay time of 5.4 s beneath MARA and PCON, hereafter referred to as Pcs (magenta lines in Figure 4-2). P**c**s is used to refer to a P to S conversion at a discontinuity located within the **crust**. This interface is of positive polarity with higher amplitudes below PCON. The seismic Moho beneath the stations, hereafter referred to as P**m**s (**Moho** interface), shows larger delay times with respect to Pcs and depicts an increase in delay time from north to south (green lines in Figure 4-2). At stations RREF and MARA (northern stations), delay times are 6.3 and 6.6 s, whereas, at PCON, SOTA, and GCUF (southern stations) they are 7.0, 7.3, and 7.0 s respectively. Arrivals at those stations reported by Poveda (2013) are 5.2, 6.0, 5.83, 7.5, and 6.6 s, respectively (see also Poveda et al., 2015). At higher delay times, beneath RREF, PCON, and GCUF, a well-defined interface with negative polarity is located at 7.9, 7.8, and 8.6 s respectively (blue lines in Figure 4-2).

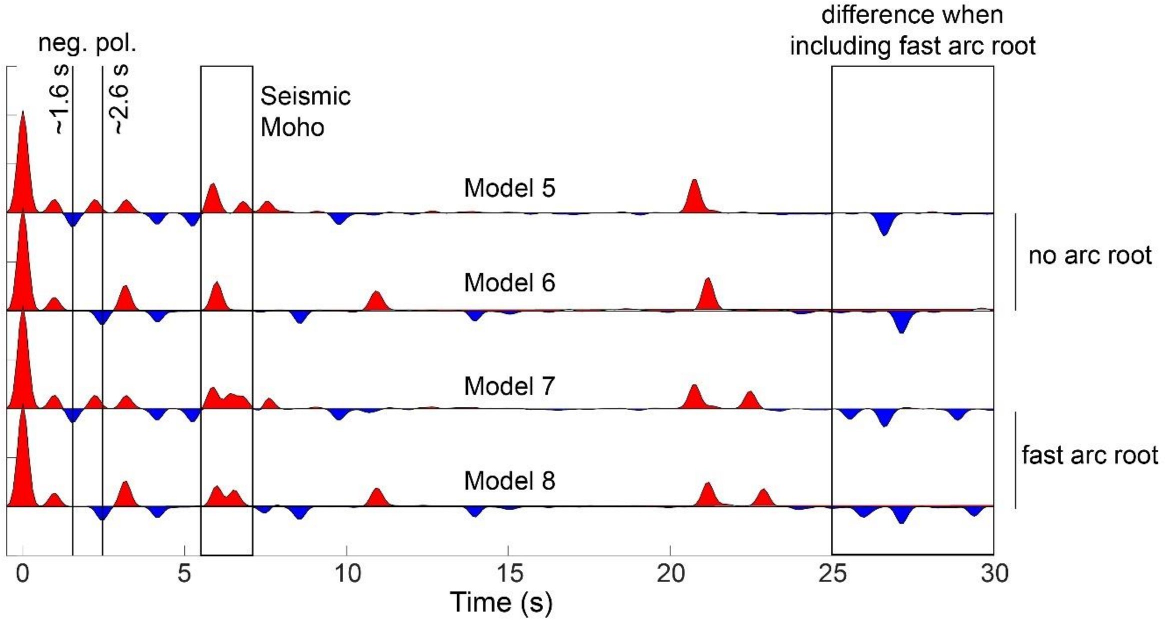

Figure 4-4. Reverberation associated with the negative polarity at ~1.6-2.6 s using different crustal structures described in Table 4-1. Models 7 and 8 further include the presence of a fast arc-root using the "composed arc root structure" (two layers).

4.4.1.1 Reverberations in the shallowest layer

Reverberations in the receiver functions associated with the shallowest layer can mislead the judgment in the detection of deeper discontinuities; to guarantee the robustness of the deeper interfaces within the crust I present the delay times of those reverberations for different crustal structures (Figure 4-3, see Table 4-1 for crustal structures).

A model considering a 3 km thick uppermost layer (model 2 in Figure 4-3 and Table 4-1) with wave speeds resembling unconsolidated sediments (Brocher, 2005), shows a Pms delay time of 6.2 s, and two peaks with positive polarity at 3.1 and 8.5 s. A model considering a 5 km thick uppermost layer (model 3 in Figure 4-3 and Table 4-1) with seismic velocities resembling sedimentary rocks (Brocher, 2005), shows a Pms delay time of 6.1 s and two peaks with positive polarity at 3.3 and 8.6 s. These two models show a double-negative polarity pattern between the crustal positive polarity pulses (3.1-3.3 s) and the Pms arrivals (6.1-6.2 s), and negative polarity in between the Pms arrival and the deeper positive peaks corresponding to reverberations (8.5-8.6 s). A final model considering a 7 km thick layer (model 4 in Figure 4-3 and Table 4-1) with seismic speeds used to represent intermediate crystalline rocks (Brocher, 2005), shows a Pms arrival at 5.8 s, a positive peak at 3.2 s, and a pulse with negative polarity at 4.2 s.

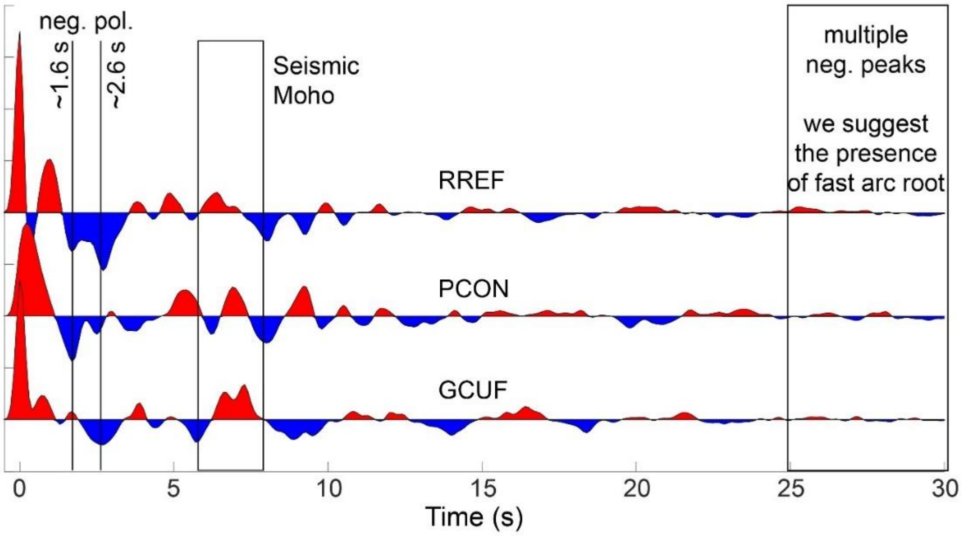

Figure 4-5. Mean receiver function (data) at stations RREF, PCON, and GCUF.

These synthetics suggest that the expected reverberations from different thicknesses and seismic speeds of the uppermost layer do not match the delay times of the inferred interfaces in Figure 4-2. The second shallowest interface beneath the stations shows delay times ranging from 1.6 to 2.6 s beneath RREF, PCON, and GCUF (Figure 4-2) while the reverberation would show a peak between 3.1 and 3.3 s (Figure 4-3). Beneath SOTA, this interface is at 4.4 s, but it is of positive polarity, clearly differing from the negative polarities at such delay times that reverberations suggest (Figure 4-3). Finally, a reverberation of positive polarity between 8.5-8.6 s also mismatches the negative polarity between 7.8-8.6 s below RREF, PCON, and GCUF (Figure 4-2). Thus, I hypothesize that the inferred boundaries in Figure 4-2 correspond to major lithospheric discontinuities.

4.4.1.2 Reverberations associated with the negative polarity at ~1.6-2.6 s

As shown in Figure 4-2 in the main text, negative polarity is observed beneath RREF and GCUF at ~2.6 s, and beneath PCON at ~1.6 s. At these three stations, negative polarity is also observed at delay times just after the Pms arrival between 7.8-8.6 s, which is considered an important feature in the discussion and interpretation of the arc root structure beneath those stations.

To better visualize the reverberations associated with this shallow crustal layer and the influence in the negative polarity defined at 7.8-8.6 s, I considered 4 crustal structures (models 5 to 8 in Figure 4-4 and Table 4-1) and analyzed the reverberation at higher times up to 30 s. Including a 5 km thick “low-velocity” layer between 12-17 km depth (model 5) and between 20-25 km depth (model 6) results in a negative polarity at ~1.6 and 2.6 s, respectively (Figures 4-4 and 4-5, see Table 4-1). These models show different reverberations between 7 and 30 s, with a positive peak and a slight negative peak near the seismic Moho when considering a negative polarity at ~1.6 and ~2.6 s, respectively. At higher delay times, a single negative peak is depicted between 25-30 s.

Models 7 and 8 represent a modified crustal structure based on models 5 and 6 respectively (see Table 4-1). They include a “composed arc root” made of a 5 km thick upper domain with seismic wave speeds 5% slower, and a 10 km thick lower domain 5% faster, relative to the underlying mantle. These models show a pattern of “double-positive-peak” at the seismic Moho followed by a slight negative peak associated with ~1.6 s negative polarity, and a larger-amplitude negative peak for the case of the ~2.6 s peak (Figures 4-4 and 4-5). Furthermore, the major differences with the models that do not consider a fast arc root (models 5 and 6) are observed in the multiple negative peak patterns shown at delay times between 25-30 s (Figures 4-4 and 4-5).

Figure 4-5 shows the mean receiver functions up to 30 s at RREF, PCON, and GCUF stations, where the negative polarity at 7.8-8.6 s is better observed (Figure 4-2). Analyzing the patterns between 25-30 s, I noticed that beneath all stations a multiple negative peak pattern is shown rather than a single negative peak. Although the amplitude of these negative peaks is short, they are well-defined, and thus, I suggest that they are better explained by a crustal structure that includes a fast arc root with a composed model (two layers).

4.4.1 Azimuthally restricted analysis

In this section, I describe the mean receiver function from the mutually correlated traces at each station (Figure 4-6). The number of obtained mutually correlated traces was four (4) at RREF, four (4) at PCON, and five (5) at SOTA from the NW back-azimuth quadrant; similarly, from the SE back-azimuth quadrant I obtained fifteen (15) mutually correlated traces at MARA, three (3) at PCON, and seven (7) at GCUF. As mentioned in the methods section, only the PCON station provided mutually correlated traces for two quadrants.

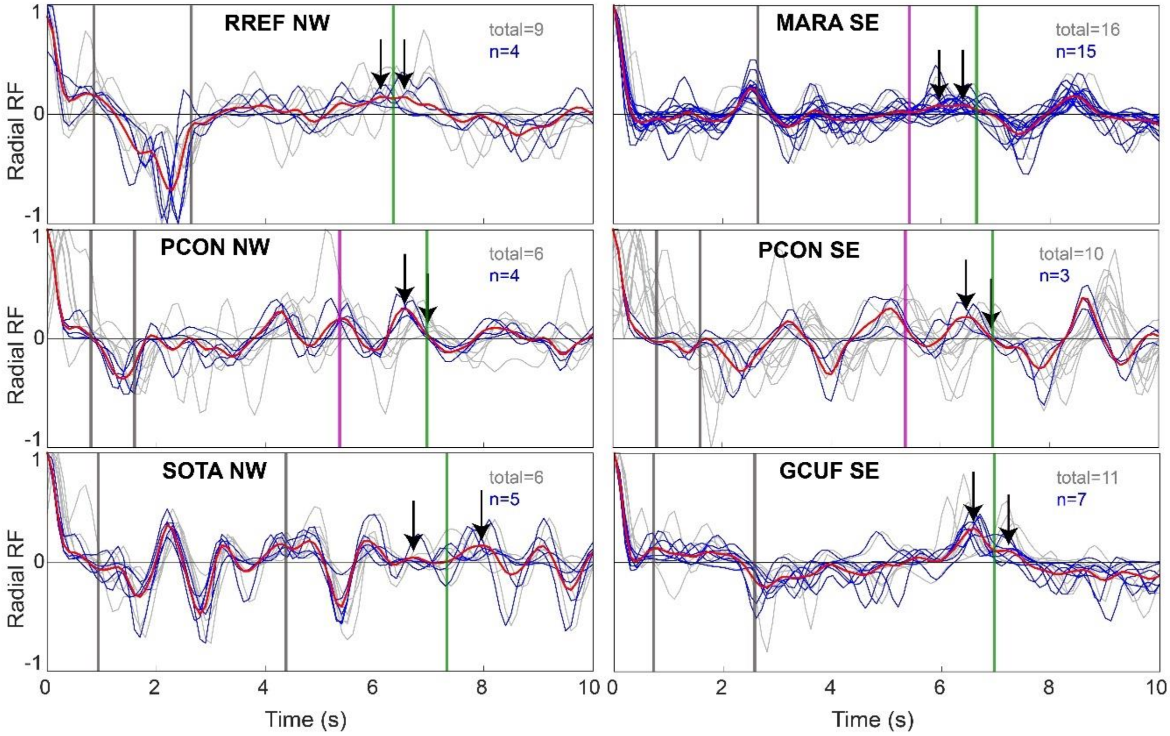

Figure 4-6. Azimuthally restricted receiver functions for each station. Grey receiver functions are traces with similar ray parameters within a back-azimuth quadrant, blue lines represent the mutually well-correlated traces, and the red curve is the mean receiver function computed from averaging blue curves. Black arrows depict a “double peak” in the vicinity of the seismic Moho (Pms). Possible major interfaces are shown as in Figure 4-2; see text for discussion.

The two upper-mid crustal interfaces are well depicted at RREF, PCON, SOTA, and GCUF, although the shallowest interface at PCON is only seen in the NW back-azimuth (Figure 4-6). At MARA, the positive polarity upper-mid crustal interface is also well-depicted. The mid-crust Pcs interface is well-defined beneath MARA and PCON; at PCON it is observed in both quadrants with a slightly earlier arrival time from the SE back-azimuth (Figure 4-6).

Below the PCON station, a complex pattern is observed between 2 and 5 s, showing a larger positive amplitude at 4.2 s in the NW quadrant, and 3.2 s in the SE quadrant (Figure

4-6). These positive polarities are seen in Figure 4-2 as well, yet they are not seen in most of the back-azimuths, thus not enough, to properly define an interface.

	Thickness (km)	**Vp (km/s)**	**Vs (km/s)**
Model 1	50.0	6.2	3.7
	0.0	8.0	4.5
Model 2	3.0	2.6	1.5
	47.0	6.2	3.7
	0.0	8.0	4.5
Model 3	5.0	4.1	2.3
	45.0	6.2	3.7
	0.0	8.0	4.5
Model 4	7.0	5.9	3.3
	43.0	6.2	3.7
	0.0	8.0	4.5
Model 5	7.0	5.9	3.3
	5.0	6.2	3.7
	5.0	5.9	3.3
	32.0	6.2	3.7
	0.0	8.0	4.5
Model 6	7.0	5.9	3.3
	13.0	6.2	3.7
	5.0	5.9	3.3
	25.0	6.2	3.7
	0.0	8.0	4.5
Model 7	7.0	5.9	3.3
	5.0	6.2	3.7
	5.0	5.9	3.3
	32.0	6.2	3.7
	5.0	7.6	4.3
	10.0	8.4	4.7
	0.0	8.0	4.5
Model 8	7.0	5.9	3.3
	13.0	6.2	3.7
	5.0	5.9	3.3
	25.0	6.2	3.7
	5.0	7.6	4.3
	10.0	8.4	4.7
	0.0	8.0	4.5

Table 4-1. Velocity structures used for reverberation analysis plotted in Figures 4-3 and 4-4.

At the vicinity of the Pms, a stretched positive peak is observed beneath RREF and MARA, which is seemingly the result of two individual peaks at 6.1 and 6.6 s below RREF, and at 6.0 and 6.4 s beneath MARA (black arrows in Figure 4-6). At PCON, both quadrants show an earlier well-defined asymmetrical peak at 6.5-6.6 s, with a small shoulder (smaller peak at slightly larger delay times) matching the delay time of Pms in Figure 4-2 of 7.0 s (Figure 4-6). At SOTA and GCUF, two well-defined peaks are observed in the vicinity of the Pms arrival. Beneath SOTA, the first peak with a small amplitude is observed at 6.7 s, whereas the second one is at 8.0 s. Beneath GCUF, the first peak with the highest amplitude is shown at 6.6 s, whereas the second one is observed as a shoulder (smaller peak with a shorter amplitude and at a slightly larger delay time) at 7.2 s (Figure 4-6). At larger delay times with respect to the Pms conversion, a positive amplitude is shown at 8.7 s in the SE back-azimuth below PCON; this corresponds to a back-azimuth restricted (140°-260°) positive polarity around 9.1 s in Figure 4-6.

In summary, this analysis shows that the mean receiver functions obtained from restricted ray paths, contain the signals corresponding to the major interfaces depicted in Figure 4-6 from integrating all back-azimuths, and more importantly, it draws attention to a particular pattern of a double-peak positive polarity in the vicinity of the seismic Moho (around the Pms). The nature of this “double-peak Moho” will be addressed in the discussion section.

4.4.2 Shear wave velocity inversion

For the description of the inverted velocity models beneath the stations, I will use the term arc root (AR) as an informal name to refer to a crustal layer above the Pms interface, showing a high-velocity value (Vs $\geq$ 4.3 km/s) at the base of the crust (see Figure 4-7).

Beneath the RREF station, the crustal structure suggests a 2.9-3.0 km/s velocity for the shallowest layer (2.5 km thick) above a 15 km thick upper crust with a 3.5-3.9 km/s velocity. The middle crust is around 15 km thick and shows slower velocities between 2.6-3.4 km/s. The lower crust is 10 km thick and shows a similar velocity to the upper crust (3.5-3.9 km/s). Materials associated with the arc root (AR in Figure 4-7) show velocities of 4.3-4.7 km/s, resembling those of the underlying mantle constrained by Sn estimates in the range 4.4-4.7 km/s (chapter 3). Below 52.5 km the speeds are between 4.9 and 5.4 km/s. These extreme values are interpreted to be a consequence of a signal contribution by an interface associated with the negative polarity at ~2.6 s (Figures 4-3 and 4-4), and/or they might also respond to upper mantle anisotropy (chapter 3; Porritt et al., 2014). I consider that the high amplitude associated with the Pms conversion implies a strong velocity contrast between materials above and below the interface. The yielded extreme velocity is then considered as an overestimation, due to an enlargement in the amplitude by the multiple contributions.

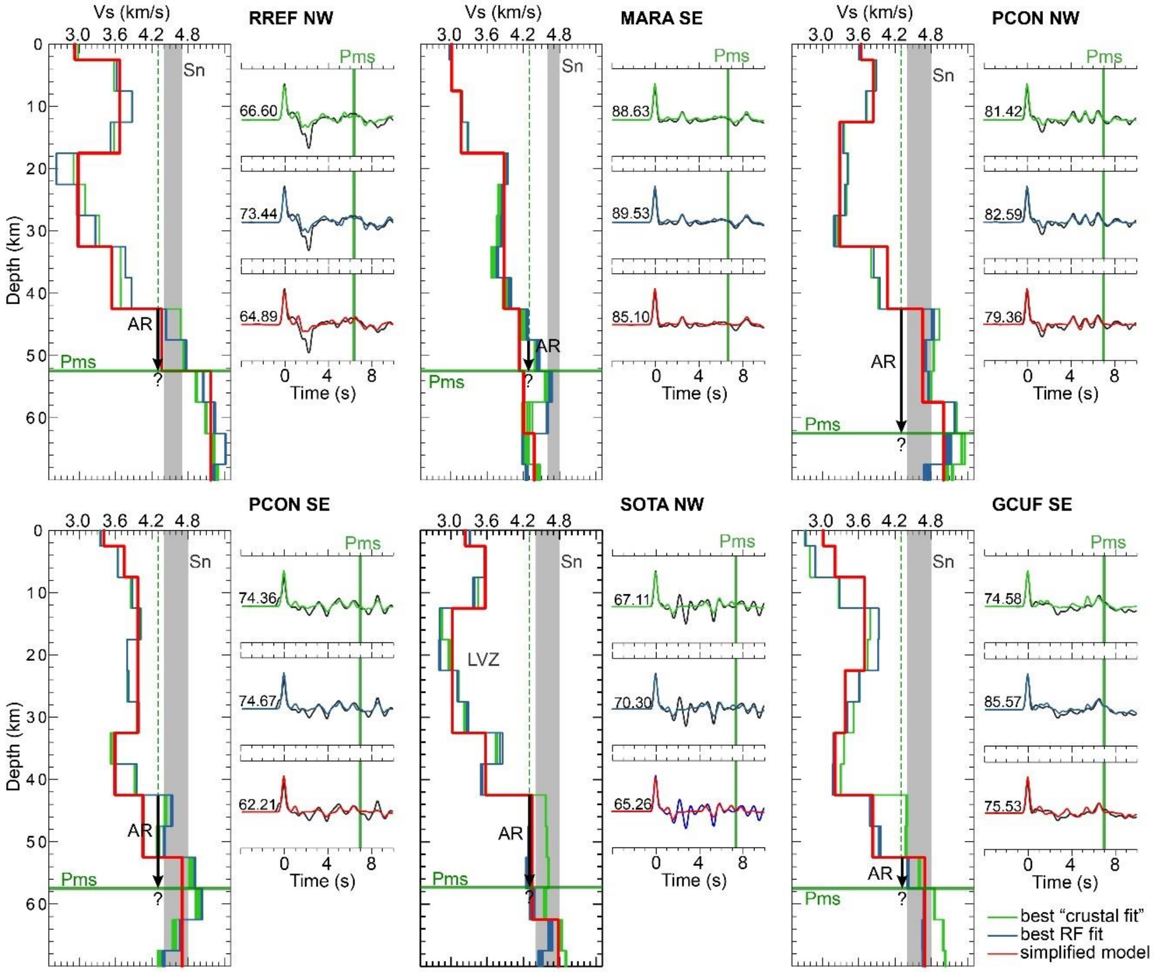

Figure 4-7. S-wave velocity inversion models beneath stations. A high-velocity (≥4.3 km/s) lower crustal section above the Pms (seismic Moho) is shown for all stations, referred to as the arc root (AR). Question marks at the base of the AR mean that no thickness considerations are derived from these models (see text for discussion). Vertical dashed lines in velocity-depth diagrams depict a 4.3 km/s velocity for reference, whereas the light gray field represents Sn estimates derived from chapter 3. In the receiver function traces diagram, the black line represents the mean receiver function from Figure 4-6, whereas colored receiver functions are synthetics associated with the models. The numbers above the traces are the fit percentages. Delay times for Pms are those from Figure 4-2.

Beneath MARA station, the models suggest a 17.5 km thick upper crust with a 3.0-3.3 km/s velocity, overlying a 25 km thick basement with velocities between 3.6-4.0 km/s. The lower crust is 5 km thick, showing high velocities of 4.1-4.3 km/s. The models with the best fit suggest an arc root (AR in Figure 4-7) with velocities of 4.3-4.5 km/s, resembling those of the uppermost mantle, but slower than available Sn estimates of 4.6-4.8 km/s (chapter 3). The simplified model suggests a velocity of around 4.15 km/s for the arc root (red line in Figure 4-7). Between ~52-57 km depth, the uppermost mantle shows a velocity of 4.5-4.7 km/s, resembling those constrained by Sn waves (chapter 3), at least based on the best crustal and receiver function fit models (Figure 4-7). Beneath this layer, the inversion suggests a slower velocity for the underlying mantle (4.15-4.6 km/s).

Modeled crustal structure beneath PCON shows differences depending on the back-azimuth. For the 12.5 km uppermost crust, both back-azimuths (NW, SE) suggest a velocity between 3.35-4.0 km/s. The underlying 20 km thick upper and middle crust shows low velocities (3.15-3.45 km/s) from the NW back-azimuth, and higher velocities (3.8-4.0 km/s) from the SE back-azimuth. Between 32.5-42.5 km depth, both back-azimuths yield a speed of 3.5-4.1 km/s (Figure 4-7). For the arc root, the models suggest velocities between 4.3-4.9 km/s from both back-azimuths, which resemble those of the Sn estimates for the uppermost mantle of 4.4-4.8 km/s (chapter 3). Similar velocities (4.3-4.9 km/s) are shown within the underlying mantle down to around 57.5 km depth; below this depth the velocity of the mantle is suggested to be faster from the NW back-azimuth (4.7-5.3 km/s) compared to the SE back-azimuth (4.3-5.0 km/s). As suggested for the inversion results beneath the RREF station, these extreme values are also interpreted to reflect the contribution of the multiple associated with the negative polarity at ~1.6 s and mantle anisotropy (chapter 3; Porritt et al., 2014).

Beneath SOTA, the crustal structure suggests a 3.2-3.3 km/s velocity for the shallowest layer (2.5 km thick), and 3.3-3.6 km/s for a 15 km thick upper crust. The middle crust is around 20 km thick with slower velocities (2.8-3.3 km/s), whereas the lower crust is 10 km thick and shows speeds between 3.2 and 3.9 km/s. For the arc root, the best receiver function fit model and the simplified model indicate a ~4.3 km/s S-wave velocity, whereas the best “crustal fit” model gives ~4.6 km/s. Only the “crustal fit” model resembles the Sn estimates of 4.4-4.8 km/s (chapter 3). Below 62.5 km depth, the underlying mantle shows velocities between 4.4-4.9 km/s, similar to the Sn estimates.

Crustal structure beneath GCUF consists of a 7.5 km thick uppermost crust with velocities between 2.7-3.2 km/s, overlying a 25 km thick basement with velocities ranging 3.3-3.9 km/s, and a 10 km thick lowermost middle crust with speeds between 3.2-3.4 km/s (Figure 4-7). A 10 km thick lower crust shows velocities of 3.65-4.0 km/s based on the best receiver function fit and the simplified model, and around 4.4 km/s based on the best "crustal fit" model. The arc root shows velocities between 4.4-4.7 km/s, resembling those from the underlying mantle constrained by Sn estimates of 4.4-4.8 km/s (chapter 3). Below 62.5 km, the suggested velocity is between 4.6-5.0 km/s, consistent with the Sn estimates.

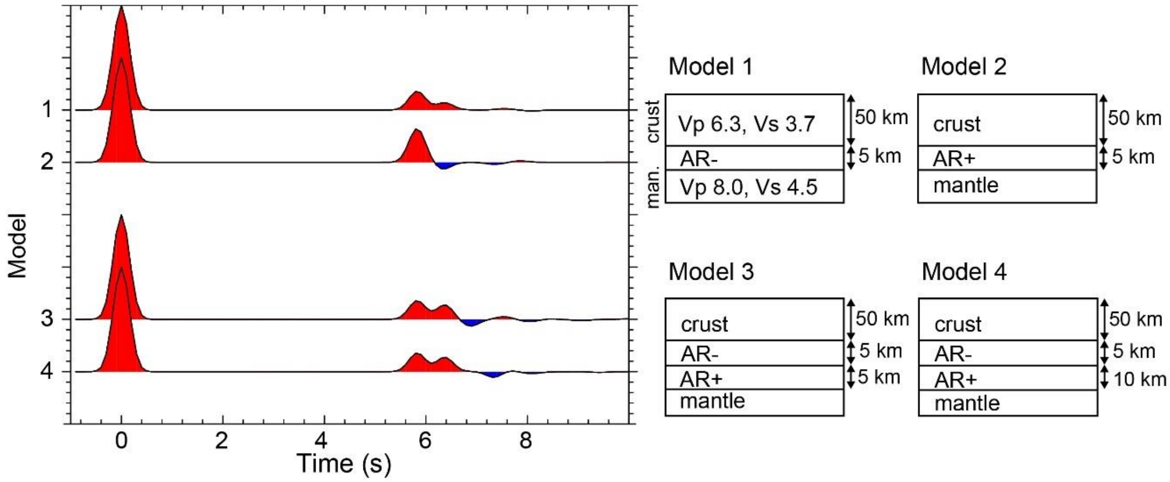

Figure 4-8. Synthetic receiver functions for different arc root architectures. Models 1 and 2 represent a simple structure with a single high-velocity layer. Models 3 and 4 are composed of arc root structures made by two layers with different high seismic speeds. AR- (or AR+) represents an arc root layer with a 5% slower (or 5% faster) velocity relative to the underlying mantle. The composed arc root (models 3 and 4) depicts the best structure for representing the volcanic arc. Notice that model 3 is composed of 5 km of AR- and 5 km of AR+ with a total arc root thickness of 10 km, whereas model 4 is composed of 5 km of AR- and 10 km of AR+ with a total arc root thickness of 15 km.

4.5 Discussion

4.5.1 The arc root architecture and its nature

It is clear from the inverted velocity models that beneath all stations, the deep crust requires high seismic velocities resembling those of the underlying mantle, to fit the synthetic receiver functions to the observed data (Figure 4-7). This high-velocity layer beneath the arc, informally referred to as the arc root in this work, represents crustal materials at the base of the arc since they are located above the Pms interface (seismic Moho; Figure 4-7), which was robustly constrained using the whole back-azimuth range (Figure 4-2). This is a very interesting finding since lower crustal materials capable of resembling seismic properties of the underlying mantle are few and very specific for this tectonic setting (Anderson, 2005; Erdman et al., 2016). However, before getting into the nature of this high-velocity layer I must address the architecture of the arc root, especially to recover the “double-peak Moho” signal (Figure 4-6). Such signal around the Pms time, is represented by a stretched peak (e.g. RREF and MARA stations), or an asymmetrical peak with a smaller amplitude (shoulder-peak) at slightly larger delay times (e.g. PCON and GCUF stations). This feature is better depicted at the receiver functions of RREF, PCON, and GCUF stations (Figure 4-6), which are located in the northern, central, and southern regions of the studied arc respectively (Figure 4-1); consequently, I consider it a consistent pattern.

In order to test for a feasible arc root architecture with a “double-peak seismic Moho” conversion, I calculated synthetic receiver functions focusing on different seismic structures beneath a 50 km thick crust (Figure 4-8). From these models, I argue that the pattern of double-positive peaks near the Pms interface can be solved by a single 5-10 km thick high-velocity layer at the base of the arc, with a 5% slower velocity relative to the underlying mantle (models 1 in Figure 4-8). However, this arc root structure fails in reflecting the negative polarity between 7.8-8.6 s shown beneath RREF, PCON, and GCUF stations (blue lines in Figure 4-2). Thus, a more complex arc root was considered by using two layers (the composed arc root model) showing an upper layer with a 5% slower velocity, and a lower layer with a 5% faster velocity relative to the underlying mantle (models 3-4 in Figure 4-8). These models, although more complex, are feasible architectures, as has been argued for continental arc settings (Ducea et al., 2021b, 2021a; Erdman et al., 2016; Lee and Anderson, 2015; Zandt et al., 2004). Their computation resulted in an improved synthetic signal that better resembles those of the observed receiver functions (Figure 4-8). Using a 5 km thick upper layer (5% slower than the underlying mantle), and a 5 to 10 km thick lower layer (5% faster velocity with respect to the underlying mantle), the synthetics reflect the double-positive peaks related to the seismic Moho and the negative polarity at higher delay times between 7.8 and 8.6 s (models 3-4 in Figure 4-8).

A possibility, however, regarding the negative polarity observed at 7.8-8.6 s, is that it might represent a multiple associated with the negative polarity at ~1.6-2.6 s (Figure 4-2), rather than an interface within the Moho vicinity. The reverberation analysis (Figures 4-4 and 4-5), suggests that the main difference between both hypotheses can be resolved at delay times between 25 and 30 s. If the negative peak at 7.8-8.6 s is associated with the negative polarity at ~1.6-2.6 s, it should show a single negative peak between 25 and 30 s. Conversely, if in addition to the negative polarity at ~1.6-2.6 s I include a composed arc root structure as described above, it not only shows a better-defined negative polarity at 7.8-8.6 s, but also shows a multiple negative peak pattern between 25 and 30 s. The analysis of the mean receiver functions beneath RREF, PCON, and GCUF, shows in fact a multiple negative peak pattern at delay times between 25 and 30 s (Figures 4-4 and 4-5), which is better explained by including a high-velocity arc root. These results support the idea that a composed model (two layers) for the arc root architecture can explain the major interfaces suggested by receiver functions along the Colombian volcanic arc.

Records at stations RREF, PCON, and GCUF are the ones that best represent the modern volcanic arc, not only because they are located to the north (RREF), the central portion (PCON), and the southern region (GCUF) (Figure 4-1), but also because they show the best back-azimuth coverage, the negative polarity interface at 7.8-8.6 s (Figure 4-2), and the best depicted double-peak pattern in the seismic Moho vicinity (Figure 4-6). To constrain the arc root structure beneath these stations, I further computed synthetics with the composed arc root model (two layers at the base of the arc), using the simplified velocity structure (red lines in Figure 4-7) beneath each station. Velocities and thicknesses were then modified to reduce the mismatch in delay times between the peaks in the synthetic receiver function and the ones associated with the major interfaces constrained from all back-azimuths in Figure 4-2.

Results suggest that a model with a ~13.5-20 km thick arc root, composed of a ~4-6 km thick upper domain with an S-wave speed 5% slower (4.275 km/s) than the underlying mantle (4.5 km/s), and a ~8.5-14 km thick deeper domain with an S-wave velocity 5% faster (4.725 km/s) than the uppermost mantle, can reproduce the major signals from the obtained receiver functions along the arc (Figure 4-9). The structure also suggests crustal thicknesses ranging ~64.5-72.5 km, which are greater than previously indicated by receiver functions (Poveda et al., 2015). This result is significant for crustal thickness estimations in areas of dense arc roots (Bowman et al., 2021; Ducea et al., 2021b, 2021a; Lee and Anderson, 2015), and is well supported by lower crust xenoliths from the Mercaderes suite, brought to the surface by Plio-Pleistocene volcanism (Bloch et al., 2017; Rodriguez-Vargas et al., 2005; Weber et al., 2002), and located between GCUF and SOTA stations (Figure 4-1).

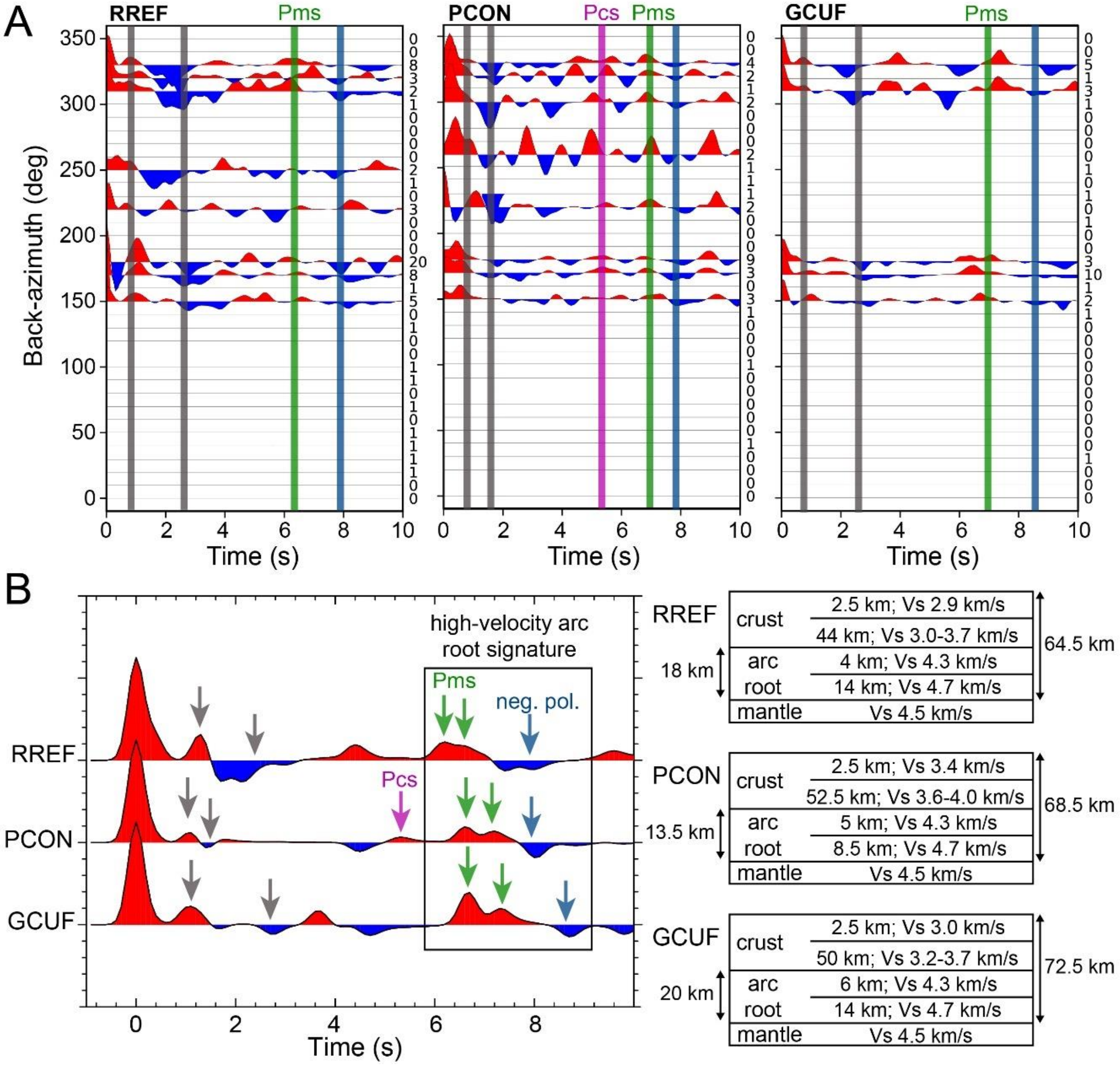

Figure 4-9. (A). Major interfaces beneath stations RREF, PCON, and GCUF from Figure 4-2. Notice the double-peak pattern surrounding the Pms, represented by a stretched or asymmetrical positive peak. (B). Synthetic receiver function modeling for a composed arc root architecture (based on models 3 and 4 in Figure 4-7). Stations RREF, PCON, and GCUF, are used since they are the ones that best represent the volcanic arc (see text). Crustal structures were initially set to the simplified model from Figure 4-7. Velocities and thicknesses were then manually modified to reduce the mismatch between the peaks in the synthetic receiver function and the major interfaces delay times (arrows in the station-time diagram).

Lower crustal xenoliths from this suite comprise an assemblage of granulites, hornblendites, pyribolites, pyroxenites, pyriclasites, pyrigarnites, and gneisses with a predominance of mafic compositions (Weber et al., 2002); some of them (pyribolites, pyroxenites, pyrigarnites) are considered to be proper arclogites (Ducea et al., 2021b). The best barometry estimates on pyribolites indicate pressures of 10-14 kbars (Weber et al., 2002), which suggests equilibrium depths between 36-50 km using a gradient of 3.6 km/kbar. However, because pyribolites contain more amphibole (hydrous phase) than pyroxene (Weber et al., 2002), they do not represent the deepest part of the arc root, which is composed of anhydrous garnet pyroxenites (Ducea et al., 2021b, and reference therein).

Equilibration depths from Bloch et al. (2017), which were derived majorly from garnet pyroxenites, are better constraints in this regard. Most of the samples show equilibrium depths between 60-80 km, which the authors used to propose a Moho boundary between 7 to 27 km below the available seismically defined Moho from receiver functions at that time (Poveda et al., 2015). Our synthetic models suggesting crustal thicknesses of around 64-73 km are, therefore, supported by these xenolithic data. Furthermore, from modeling of S-wave velocities using garnet pyroxenite xenoliths from the Mercaderes locality (Figure 4-1), I found that speeds for this type of rock are between 4.5 and 4.85 km/s (Supplementary Material S4-1). Such values support the feasibility of the considered velocity of 4.725 km/s for the arc root used in the synthetics (Figure 4-9), suggesting a ~5% faster speed with respect to the ~4.5 km/s underlying mantle. These constraints show the importance of evaluating the presence of high-velocity layers within arc roots when using seismic constraints in continental arc settings.

I interpret the high-velocity layer at the base of the Colombian volcanic arc as arclogite in nature. This interpretation is considered robust to the south of the study region, where the xenolith suite is located, whereas to the north, the lack of documented xenolith localities diminishes the robustness of this interpretation. Nevertheless, there is a consistent receiver function pattern that is depicted beneath RREF, PCON, and GCUF, which is characterized by a double positive peak in the Pms vicinity, followed by a negative polarity interface at 7.8-8.6 s (Figures 4-2 and 4-9). I suggest that this pattern provides evidence for a similarity in the nature and architecture of the arc root between the southern and northern regions, and thus, I interpret an arclogitic nature of the root in the northern part as well. Furthermore, I propose that this pattern can reflect a high-velocity arc root signature (Figure 4-9), which can be used for evaluating the possibility of having garnet pyroxenites at the base of modern continental magmatic arcs.

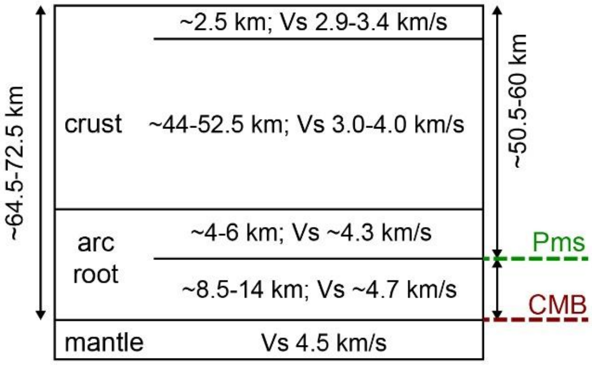

Figure 4-10. Proposed arc root architecture beneath the modern Colombian magmatic arc by integrating the thicknesses and velocities beneath RREF, PCON, and GCUF stations from Figure 4-9. Pms represents the seismic Moho (geophysical change), whereas CMB stands for crust-mantle boundary (geological change).

In summary, the model argues for a ~64.5-72.5 km crustal thickness beneath the Colombian modern arc, with a crust-mantle boundary at such depth (~64.5-72.5 km), and a shallower seismic Moho at ~50.5-60 km (Figure 4-10). The crust-mantle boundary in this regard is considered a petrologic Moho (geological change; Cook et al., 2010; Ducea et al., 2021b); whereas the seismic Moho is a receiver function geophysical interpretation above which the crustal rocks show dissimilar seismic properties with respect to the underlying mantle. If correct, the model argues for a depth mismatch between the seismic Moho and the crust-mantle boundary of around 8.5-14 km.

4.5.2 Insights into other interfaces within the crust

The Pcs interface is observed only beneath MARA and PCON stations (Figure 4-2). I interpret this discontinuity as a middle-lower crust transition beneath the central portion of the arc. The fact that the interface is well-depicted only beneath this portion, might suggest a linkage with the observed reduction in surface volcanism (Figure 4-1). I speculate that a diminished production of magmatism below this part of the arc allows the preservation of an existent sharp transition between the middle and the lower crust, which is less blurred by current magmatic intrusions (batholiths). Less magmatic supply in the middle-lower crust transition can be supported by the higher velocities suggested by inversion models, compared to the northern and southern stations (Figure 4-7). The reduction in magmatic influx at the central portion of the arc and its causes remain enigmatic though and are beyond the scope of this work. Further constraints are therefore required to validate this hypothesis.

Regarding shallower discontinuities, they are majorly negative in polarity, which can be explained, as suggested by inversion models, as the top of low-velocity zones within the upper to middle crust (Figure 4-7). I consider that these interfaces might be associated with magmatic chambers located at different depths beneath the active volcanoes. Based on available constraints on magma reservoirs through tomographic imaging (e.g. Londoño and Sudo, 2003; Vargas et al., 2012), and inferences from magmatic products and geochemistry (e.g. Correa-Tamayo et al., 2020; Monsalve-Bustamante, 2020 and reference therein), magma chambers within the mid-crust are plausible.

4.6 Conclusions

Receiver function analysis at five active volcanoes from the Colombian modern arc, is consistent with a ~64.5-72.5 km crustal thickness, with a depth mismatch between the seismic Moho and the crust-mantle boundary of around 8.5-14 km. The high-velocity arc root shows a latitudinal variable thickness, from 13.5 to 20 km, composed of a 4 to 6 km thick upper domain with seismic wave speeds 5% slower, and 8.5 to 14 km thick lower domain 5% faster, relative to the underlying uppermost mantle. This seismic lower crustal architecture coupled with documented lower crustal xenoliths supports an arclogite nature for the Colombian Andes arc root.

4.7 Publication or submission

This paper has been accepted for publication in *Tectonophysics*. Co-author of this paper is Monsalve, G.

Assigned doi to the accepted article is https://doi.org/10.1016/j.tecto.2022.229417.

4.8 Acknowledgments

Thanks to S. León and G. Posada for discussions about the Colombian magmatic arc, its evolution, and available geophysical and geological constraints within the area. Comments and suggestions by editor C. Currie and two anonymous reviewers improved the quality of this work. This work was supported by the Fundación para la Promoción de la Investigación y la Tecnología (Project 4.634).

5. Crustal underthrusting beneath the northwestern Eastern Cordillera plateau, Colombian Andes: Insights from a joint local earthquake arrival time – gravity inversion

5.1 Summary

The northern Eastern Cordillera in the Colombian Andes represents a wide (~200 km) highly-elevated (>2.5 km) subduction-related asymmetric plateau. It is currently subjected to shortening and magmatic additions, and yet, the nature of the lowermost crust and its transition to the underlying mantle remains poorly constrained. To improve our knowledge about the structure of the deep crust beneath the EC plateau, I conducted a joint inversion of arrival times of local earthquakes and gravity data. Along the latitudinal profile with the highest resolution (~5.7°N) two anomalies are identified at depths of 40-60 km beneath the plateau. A western slow velocity anomaly is interpreted as crustal materials eastwardly underthrusting beneath the northwestern EC. This process is thought to be prompting the abrupt change in topography between the adjacent low-elevated basin and the orogenic plateau. On the other hand, a fast velocity anomaly beneath the eastern flank of the EC is interpreted as reflecting metasomatic processes within the mantle wedge. The metasomatism is related to either mafic magma interaction with the uppermost mantle, or silica influx during past flat-slab subduction located further to the east.

5.2 Introduction

The seismic structure of the lowermost crust beneath an active subduction-related orogenic plateau can be complex when processes contributing to crustal thickening involve tectonic underthrusting and magmatic underplating (Armijo et al., 2010; Sippl et al., 2013; Sobolev and Babeyko, 2005; Thybo and Artemieva, 2013; Vietor and Oncken, 2005; Wang et al., 2013). These processes allow the deep crust to host high-velocity and high-density materials that resemble in physical properties of the underlying mantle, and thus, the structure of the lowermost crust is not always easy to image and interpret (Baumont et al., 2002; Beck and Zandt, 2002; Guerri et al., 2015; Myers et al., 1998; Thybo and Artemieva, 2013; Wang et al., 2013).

Understanding the structure of a lowermost crust subjected to those processes beneath an orogenic plateau is therefore challenging, but critical to argue for crustal thickness variations, the deformation style, and along-strike discrepancies, for the recognition of plausible rootless domains, and for the involvement of subcrustal mechanisms such as delamination and/or foundering tectonics (Armijo et al., 2010; Beck and Zandt, 2002; DeCelles et al., 2015; Lee, 2014; Schurr et al., 2006; Sobolev et al., 2006; Vietor and Oncken, 2005; Ward et al., 2016; Zandt et al., 2004).

Along the Colombian Andes, the northern part of the Eastern Cordillera (EC) represents a wide (~200 km) highly-elevated (>2.5 km) subduction-related asymmetric plateau (Mora et al., 2015, 2008; Siravo et al., 2021), which is subjected to crustal thickening due to shortening (Bayona et al., 2008; Mora et al., 2013, 2008; Siravo et al., 2018; Tesón et al., 2013; among others) and magmatic additions, some of them in the form of underplating (Monsalve et al., 2019). The amount of shortening is discrepant on both sides of the orogenic plateau, reaching up to 40 km at the western flank (Cortés et al., 2006; Mora et al., 2008; Sánchez et al., 2012), and 30 to 90 km, and possibly up to 100-150 km, at the eastern flank (Montes et al., 2019; Mora-Páez et al., 2016; Tesón et al., 2013).

The deformation style of the EC and the adjacent western Magdalena Valley (see Figure 5-1) has been widely addressed through integrated on-surface structural measurements and cross-section restoration, seismic profiling, thermochronology, and provenance constraints (Horton et al., 2020; Mora et al., 2020 and references therein). Yet, the structure of the deepest part of the crust and its transition to the underlying mantle remains poorly investigated and understood. Available geophysical approaches include teleseismic receiver functions at a few stations close to the axis of the EC plateau (Monsalve et al., 2019; Poveda et al., 2015), and regional-scale tomography (Chiarabba et al., 2015; Poveda et al., 2018; Syracuse et al., 2016; Vargas, 2020; among others).

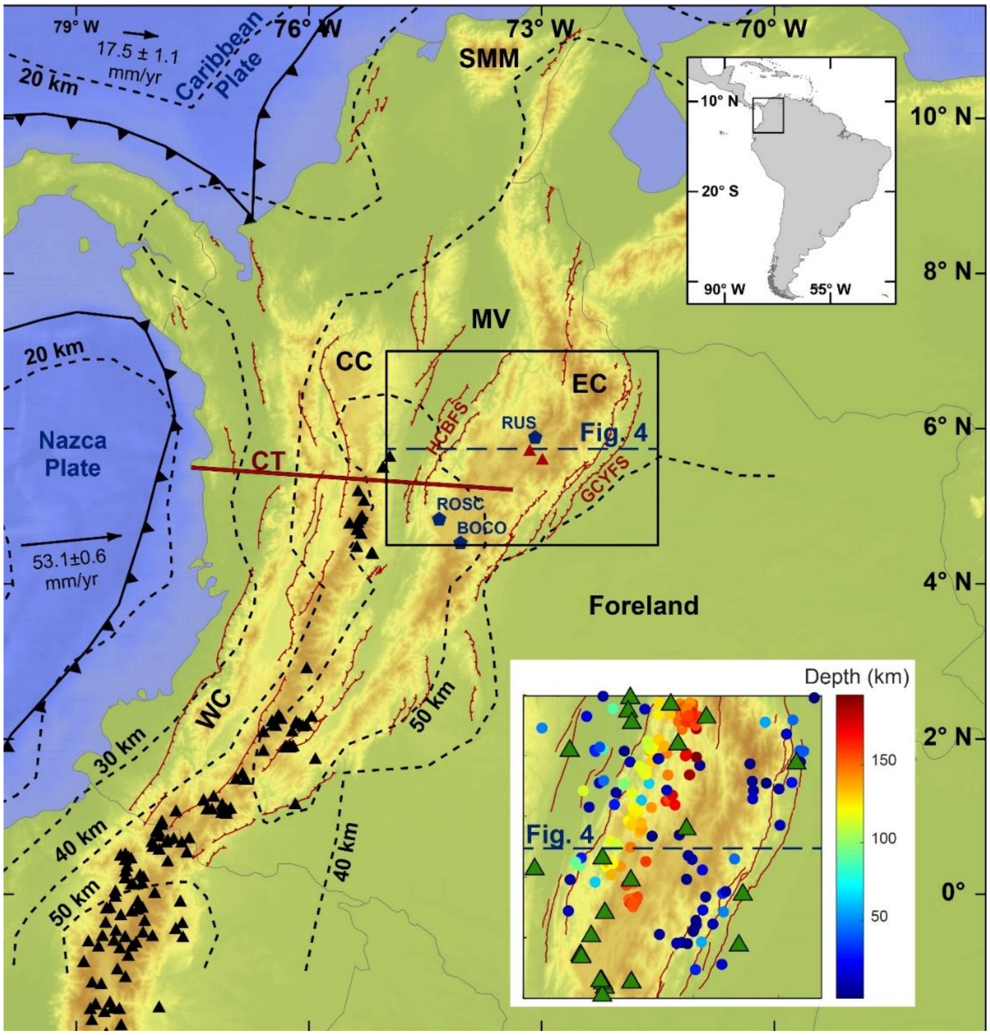

Figure 5-1. Map view of the northwestern Andes with the main tectonic features and the area for the inversion of seismic velocities (black box). Tomographic profile shown in Figure 5-4 is depicted as a dashed blue line. Three stations within the study area (RUS, ROSC, BOCO) with available receiver function analysis (Monsalve et al., 2019; Poveda et al., 2015) are shown as blue pentagons. Modern volcanic centers are represented by black triangles, and Mio-Pleistocene volcanism by red triangles (Bernet et al., 2016; Monsalve et al., 2019); red lines are active thrusting faults (Veloza et al., 2012), and dashed black lines are crustal thickness contours (Poveda et al., 2018). HCBFS: Honda-Cambao-Bituima fault system, GCYFS: Guicaramo-Cusiana-Yopal fault system. Caldas tear (CT) is represented by the solid red line after Vargas (2020). WC, CC, and EC, stand for Western, Central, and Eastern Cordilleras, whereas MV and SSM for Magdalena Valley and Santa Marta Massif, respectively. Convergence rate of the Caribbean and Nazca plate with respect to stable South America after Mora-Páez et al. (2019). Inset figure: Earthquakes (circles colored by depth) used for the tomographic inversion within the study area. Green triangles represent the 28 stations used for the inversion.

Receiver functions, on one hand, have been used to constrain crustal thicknesses, proposing a latitudinal dissimilarity along the EC, varying from ~60 km at ~4.5°-4.8°N (BOCO and ROSC stations in Figure 5-1) to ~46-53 km towards the north at ~5.9°N (RUS station in Figure 5-1) (Poveda et al., 2015). On the other hand, the analysis of receiver functions at the RUS station (see Figure 5-1) suggests a high-velocity layer at ~36 km depth, which has been interpreted as magmatic underplating, being consistent with Mio-Pleistocene volcanism of the Paipa-Iza volcanic complex (Figure 5-1; Bernet et al., 2016; Monsalve et al., 2019).

Regarding regional-scale tomography, most of the available images were built to elucidate the subduction geometries beneath the Colombian Andes (Chiarabba et al., 2015; Sun et al., 2022; Syracuse et al., 2016; Vargas, 2020; among others). Therefore, their resolution is insufficient to address the lowermost crust beneath the EC plateau. Furthermore, the ambient noise tomography reported by Poveda et al. (2018), addresses the upper and middle crust (above 40 km depth), and thus, it is quite limited for the understanding of the lower crust below the EC, which lies between ~45-60 km (chapter 2; Poveda et al., 2015).

Thereby, to improve our knowledge about the structure of the deep crust beneath the EC plateau I conducted a joint inversion of local earthquakes and gravity data. This approach is useful in disentangling complexities within the lowermost crust and across the crust-mantle boundary beneath subduction-related orogenic plateaus (Koulakov et al., 2006; Myers et al., 1998; Schurr et al., 2006; Ward et al., 2016). The joint tomography includes the arrival time from recorded P- and S-wave phases associated with local earthquakes, and total Bouguer anomaly data. Moreover, I included in the analysis the average uppermost mantle velocity based on Pn-wave speed estimates.

In this chapter, I present an analysis along the latitudinal profile (W-E) with the highest resolution (~5.7°N, Figure 1), in which tomographic results suggest the presence of two main features, a slow and a fast velocity anomaly. Both are placed at similar depths of 40-60 km, yet the slow anomaly lies beneath the western flank of the EC, while the fast one beneath the eastern flank. The slow anomaly is interpreted to represent crustal materials that are eastwardly underthrusting beneath the northwestern EC, whereas the fast anomaly likely reflects metasomatic processes within the mantle wedge.

5.3 Data and Methods

5.3.1 Seismic and gravity data

Within the study area, arrival times of recorded P- and S-wave phases associated with local earthquakes were gathered from the International Seismological Centre (ISC), at a total of 28 seismic stations (Figure 5-1). Earthquakes were filtered to consider events with hypocenters not deeper than 200 km (Figure 5-1) and a minimum magnitude of 3. Since the obtained arrival time data include a residual time with respect to global velocity models: *ak135* (Kennett et al., 1995) and *JB* (Jeffreys and Bullen, 1940) prior to January 2006, I filtered the data so that the absolute value of such residual time is $\leq$10 s. I used this criterion as a cutoff for removing some of the picked phases associated with high residuals. The resulted dataset was then subdivided into two subsets, one including only the P-wave arrival records, and the second one only the S-wave arrivals. For each subset, I removed data with arrival times outside the 5-95th percentile interval, aiming to reduce the complexity of the inverted model.

Because I intended to include the hypocentral location in the set of parameters to invert for, I only considered those earthquakes for which the P-wave arrival was recorded by at least 5 different stations. Conversely, because of the limited amount of the S-wave data, no filtering by the number of stations was considered for this wave. The latter means that the seismic event with the “poorest” number of recorded phases would include 5 arrival times associated with the P-wave and no S-wave data. A total of 1,378 seismic events between 2000 and 2022 were finally used, including 9,335 and 9,004 recorded phases for the P- and S-wave respectively.

Additionally, the input gravity data was obtained from a 5 mGal contoured Total Bouguer anomaly map built by the National Hydrocarbon Agency of Colombia (Graterol and Vargas, 2010). A spacing of 0.25° (~28 km) was chosen to extract the gravity data from the contoured map.

5.3.2 Inversion analysis

The inversion was computed through the Joint Tomography Software Package described in Roecker et al. (2006). The data set consists of P- and S-wave travel time arrivals using local earthquakes, and the Bouguer gravity anomaly. Epicentral distances of the considered earthquakes range between 0.05°-3.56°, with a mean value of 1.48°. The relationship between density and seismic velocity follows the equations given in Brocher (2005) (see Roecker et al., 2017).

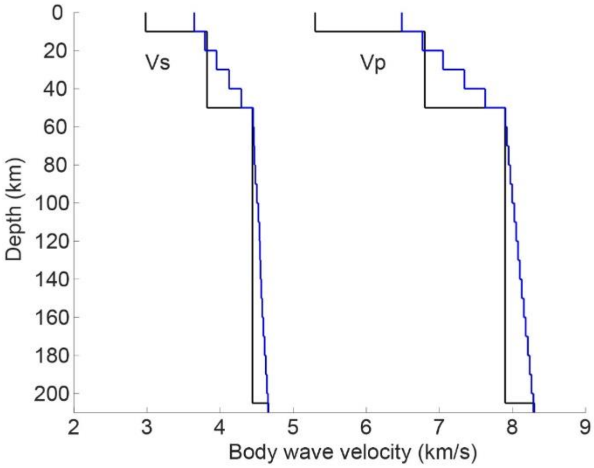

Figure 5-2. Initial velocity structures for final inversion. Black lines represent the 'starting velocity model', resulting from integrating a local P-wave tomographic inversion carried out to the north of the study region (Londoño et al., 2010), and a Vp/Vs ratio of 1.78 estimated by receiver functions (Poveda et al., 2015). Blue lines represent the improved 1D model after inverting the data for 5 iterations using the 'starting velocity model' as the initial structure. The blue lines are the reference model for the tomographic inversion shown in Figure 5-4.

The earth volume was parameterized using nodes with a known spacing along the latitude, longitude, and depth directions, setting a linear variation in seismic slowness in between the nodes. Travel times are computed through a finite-difference solution to the eikonal equation (Hole and Zelt, 1995; Vidale, 1990), increasing the accuracy in ray tracing within strongly heterogeneous media, and yielding less ambiguity in global travel time minima (see Roecker et al., 2006). The solution to the inverse problem is achieved by the LSQR algorithm of Paige and Saunders (1982). More details of the method are given in Roecker et al. (2017, 2006).

The tomographic volume for the study area is defined between 4.5°-7.0°N and 75.0°-71.5°W (Figure 5-1), and between -30 and 200 km in depth (negative values represent positive elevations). Node-spacing was set to 0.09° (~10 km) in the latitude and longitude directions (29-by-39 node-grid), and 10 km in the vertical direction (24 nodes).

To use a 1D initial velocity model suitable for the data, I took advantage of a local P-wave tomographic inversion carried out to the north of the study region (Londoño et al., 2010), and a Vp/Vs ratio of 1.78 estimated by the receiver functions (Poveda et al., 2015). The integration of those constraints permitted the construction of a 'starting velocity model' (black line in Figure 5-2). Given the ability of the code not only to update the 1D velocity model with each iteration, but also to interpolate velocity with depth, I invert the data for 5 iterations using the 'starting velocity model' as the initial structure. From this approach, an improved 1D velocity model was obtained at the final iteration (blue line in Figure 5-2), showing arrival time residuals between -2.15 and 1.87 s, with the highest frequency close to zero for both waves (Figure 5-3). Average hypocenter displacement after those iterations yield ~0.07° (~7.8 km) in the epicenter location, and ~13 km in depth. The above, coupled with good back-azimuth coverage by the data (Figure 5-3D), points to a promising inversion using the improved 1D velocity model as the initial structure.

Out-of-network events were considered for the tomographic inversion (Figure 5-1), which means no azimuthal gap filtering. The inclusion of this data improves the quality of reconstruction in local earthquake tomography (Koulakov, 2009), especially in deeper parts of the crust and upper mantle, where the discussion of this work focuses. A positive contribution of these events, by significantly increasing the number of earthquakes (amount of data) and wider coverage of the ray paths, compensates for any effect of the larger error in the location of the source (Koulakov, 2009). Nearly 80% of the used earthquakes have an azimuthal gap lower than 280°, whereas 10% of the events have gaps lower than 180° (Figure 5-3D).

Before running the final inversion, different dampers were tried for 10 iterations each. From all possibilities, I choose a damper of 500, as it showed a good trade-off in minimizing the data and model variances (Table 5-1). I used this damper to obtain the final inversion after 15 iterations, at which the reduction of the data variance stalled. The achieved percentage in the data variance reduction was ~58%, with a final data variance of 0.0915 s^2 and a model variance of 0.0071 $(km/s)^2$ (Table 5-1). The data variance was computed by the code, whereas the model variance was calculated using the equation given in Jones et al. (2014). Finally, for the final inversion, a moving window of 5 nodes in the latitude and longitude directions and 3 nodes in-depth was considered, as it showed a good trade-off between data variance reduction and less complexity of the model.

5.3.3 Resolution

The resolution of the tomographic inversion was evaluated by the conventional checkerboard test and ray path coverage (Figure 5-4), together with the recovery of synthetic prismatic geometries (Figure 5-5). For the checkerboard test, I considered alternating ± 5% velocity perturbations of the initial velocity model (blue line in Figure 5-2), in prisms composed of 4 nodes (~30 km) in the latitude and longitude directions, and 5 nodes (~40 km) in depth (Figure 5-4). Synthetic recoveries were individually inspected for all possible latitudinal profiles, obtaining the highest resolution at latitudes of ~5.5°-6.0°N. To avoid misinterpretation, I focused the discussion along the profile with the highest resolution (~5.7°N), taking advantage of its proximity to the RUS station (Figure 5-1), where some aspects of the lithospheric structure have been addressed using teleseismic receiver functions (Monsalve et al., 2019; Poveda et al., 2015).

As will be discussed, two main anomalies were observed along the ~5.7°N profile, a slow and a fast velocity anomaly (Figure 5-4). To assess their robustness, I further test the recovery at those sites by using prismatic synthetic geometries with a given velocity perturbation (Figure 5-5). The geometries were latitudinally defined between 5.38°-6.19°N for all the following cases. For the slow anomaly, the prismatic geometry was placed at depths of 40-60 km, within which two features were evaluated: The first one considers a longitudinally defined anomaly between 73.38°-74.37°W with a constant -5% velocity perturbation (Figure 5-5A), whereas the second feature consisted of a larger anomaly in between 72.30°-74.37°W and the same -5% velocity perturbation (Figure 5-5B). Those tests were done to evaluate the feasibility of a limited extension of the anomaly beneath the western flank of the EC rather than across the entire plateau. Furthermore, to evaluate the feasibility of the two anomalies (slow and fast velocity anomalies) lying at a similar depth but at different longitudes, a third synthetic geometry was placed at depths of 40-60 km and between 72.30°-74.37°W, describing a constant velocity perturbation of -5% to the west (slow velocity anomaly) and 5% to the east (fast velocity anomaly) (Figure 5-5C).

5.3.4 Uppermost mantle velocity using Pn waves

Pn waves are thought to travel just beneath the Moho and to be critically refracted at the crust-mantle boundary to reach the seismic stations (Storchak et al., 2003). This makes them very useful to constrain the uppermost mantle velocity just below the crust. To estimate an average Pn velocity beneath the northern EC I applied the two-station approach, which minimizes the effects of uncertainty in hypocentral location and the crustal heterogeneity at the source (Beghoul and Barazangi, 1989). An apparent velocity for the upper mantle, in between a pair of stations, can be estimated through the ratio of the distance between the stations and the arrival time difference for a recorded event. The used earthquakes were filtered to consider events with absolute residual arrival time not higher than 3 s with respect to the global velocity models (section 5.3.1). Moreover, for this kind of estimate, the epicenter of a given earthquake must be as colinear as possible with respect to the azimuth between stations, and thus, I set 6° as the maximum angle difference, following Beghoul and Barazangi (1989).

Finally, a correction was applied aiming at a better estimation of the Pn velocity in between stations. Since the seismic stations are located on the surface, while the Pn waves are traveling below the Moho, the distance between the pair of stations was multiplied by a correction factor of 0.992, derived from assuming a spherical Earth and an average crustal thickness. The correction factor was computed as $(Er - ct)/Er$, where Er is the Earth's radius (6,371 km; e.g. Shearer, 2009) and ct an average crustal thickness of 50 km along the EC plateau (chapter 2; Poveda et al., 2015). Velocity estimates are presented in Supplementary Material S5-1.

Damper	Data variance (s^2)	Model variance $(km/s)^2$	Iterations
200	0.0964	0.0095	10
300	0.0940	0.0068	10
400	0.0946	0.0054	10
500	0.0950	0.0045	10
700	0.0957	0.0034	10
1000	0.0978	0.0024	10
500	**0.0915**	**0.0071**	**15**

Table 5-1. Obtained data and model variances for different dampers after 10 iterations each. From this analysis I selected a damper of 500 since it showed a good trade-off in the minimization of both variances. Final variances associated with the inversion shown in Figure 5-4 are shown in bold (obtained after 15 iterations).

5.4 Results and Discussion

From our final inversion, a good minimization in the residuals of body wave travel times was achieved, whereas gravity residuals showed a more scattered pattern (Figure 5-6). P-wave residuals are between -2.03 and 1.65 s with a mean of 0.0019 s, whereas the S-wave residuals are between -2.30 and 1.82 s with a mean of -0.002 s (Figure 5-6A-C). The 25-75th percentile ranges between -0.11 and 0.12 s for the P-wave, and -0.22 and 0.22 s for the S-wave. On the other hand, gravity residuals vary between -76.34 and 45.02 mGal (Figure 5-6D). The 25-75th percentile interval of gravity residuals ranges between -13.60 and 15.58 mGal, with a median of 4.19 mGal.

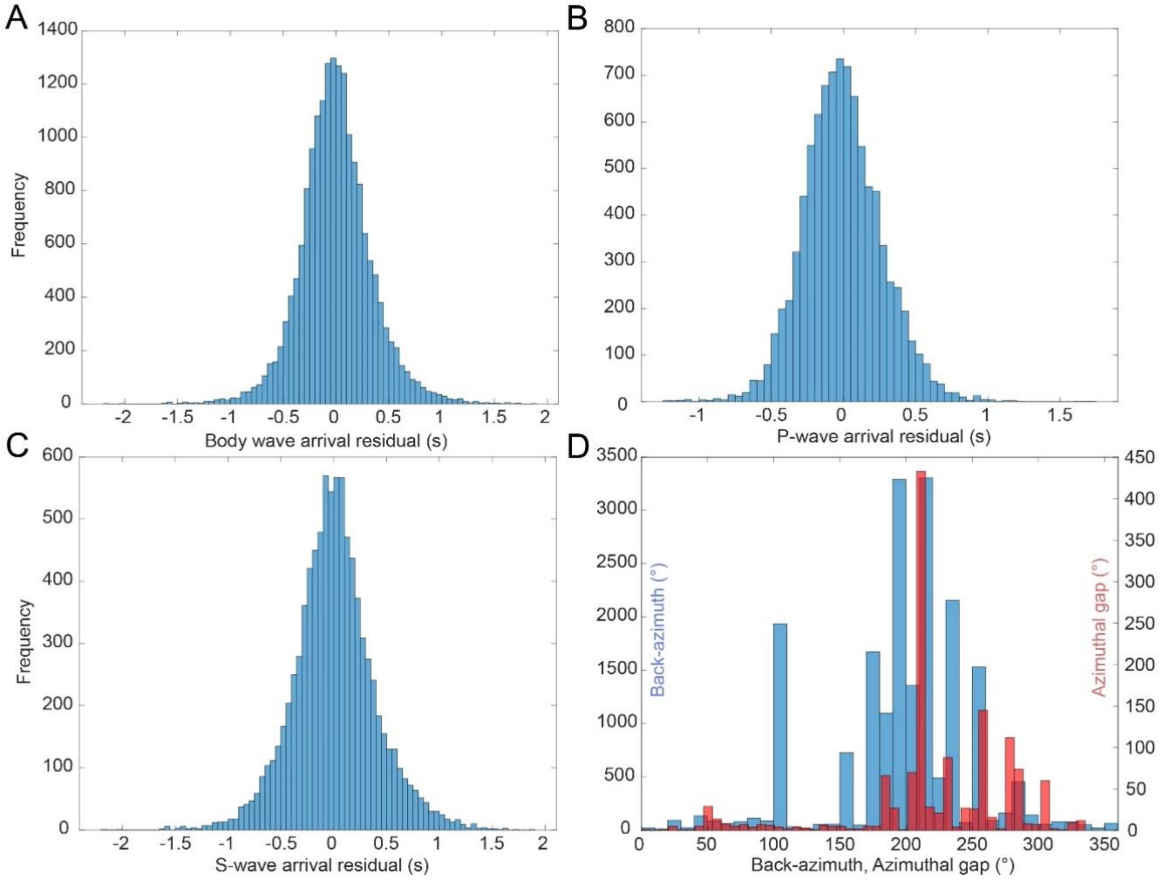

Figure 5-3. (A-C) Histograms of arrival time residuals for body wave after inverting the data for 5 iterations using the ‘starting velocity model’ (black lines in Figure 5-2) as the initial structure, to obtain the 1D model given by the blue lines in Figure 5-2. Body wave residuals in (A) include both, P- and S-wave data. (D) Histograms of back-azimuth (blue) and azimuthal gap (red), showing the coverage of seismic events used in the final inversion (see also Figure 5-1 inset).

I consider that the highest residuals in gravity are associated with those regions that are not well resolved due to the ray path coverage and the station array. Consequently, to avoid misinterpretations, I will discuss two well-imaged anomalies along the latitudinal profile with the highest resolution (~5.7°N). These two anomalies are considered to be well imaged, as suggested by the checkerboard test, the ray path coverage, and the synthetic tests (Figures 5-4 and 5-5). They include a slow velocity anomaly beneath the transition between the Magdalena Valley and the western EC, and a fast velocity anomaly beneath the eastern flank of the EC (Figures 5-4 and 5-5). I will refer to these features as the ‘slow’ and ‘fast’ anomalies for simplicity.

5.4.1 Underthrusting beneath the northwestern EC plateau (slow anomaly)

Beneath the western flank of the EC plateau, the slow anomaly is observed between 73.6°-74.2°W at depths of 40 to 80 km (Figure 5-4). The anomaly shows slower speeds with respect to the reference velocity structure (blue line in Figure 5-2) up to -3.8% in P-wave, up to -3.4% in S-wave, and up to -2.7% in the Vp/Vs ratio (Figure 5-4). As shown by the synthetic tests, a -5% perturbation of a prismatic geometry placed at depths of 40-60 km is recovered as a thicker anomaly down to ~80 km (Figure 5-5). Thus, I consider it feasible that the slow anomaly in Figure 5-4, between 40 and 80 km, represents a body that is placed between 40 and 60 km, rather than down to 80 km. At those depths, the highest differences with respect to the reference velocity model are retrieved: -3.8% in P-wave, and -3.4% in S-wave.

The underlying mantle, at depths of 60 to 80 km, shows differences with the reference model between -1.5 and -3.8% for Vp, and -1.2 to -3.4% for Vs. As previously mentioned, the retrieved slower velocities with respect to the reference structure, between 60 and 80 km, are a consequence of a “thicker” recovery of a body placed at 40-60 km. Therefore, these discrepancies with the reference velocity model between 60 and 80 km are not the ones characterizing the uppermost mantle. Consequently, uppermost mantle speeds might be better defined by the lowest differences with the reference model at depths of ~80 km. These values are -1.5 to -1.6% in Vp yielding a speed of ~7.9 km/s, and -1.2 to -1.6% in Vs suggesting a speed of ~4.4 km/s. The Vp value is consistent with the average Pn velocity between 7.8-8.2 km/s obtained from the two-station approach (Figure 5-7), which I considered as the representative speed for the uppermost mantle beneath the EC plateau.

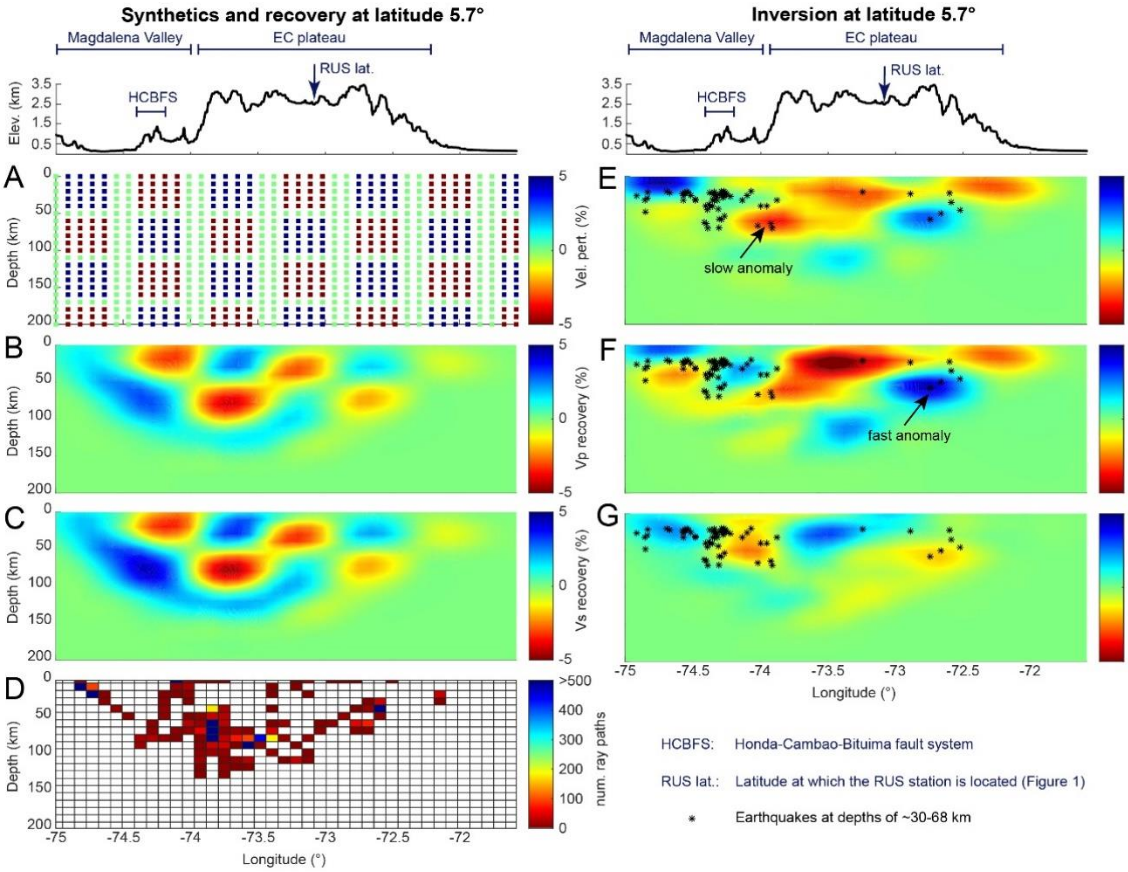

Figure 5-4. Results of tomographic inversion at ~5.7°N using the initial velocity structure in Figure 5-2 (blue lines). On top, the elevation profile is derived from the ETOPO1 model (Amante and Eakins, 2009). (A) Checkerboard test using nodes with alternated velocity perturbation of ± 5%. (B-C) Inversion recovery of the checkerboard structure in terms of Vp and Vs. (D) Ray path coverage. (E-G) Inversion results, with the two discussed anomalies (slow and fast anomaly). Notice the abrupt change in topography above the slow anomaly that describes the transition between the Magdalena Valley and the EC plateau.

The above suggests that the slow anomaly is associated with a body placed between 40-60 km, with speed anomalies up to -3.8% in P-wave, in reference to a mantle velocity of 7.6-7.9 km/s (Figure 5-2) that is consistent with Pn data (Vp 7.8-8.2 km/s; Figure 5-7). Consequently, I interpret the slow anomaly as representing crustal materials beneath the transition between the Magdalena Valley and the western flank of the northern EC plateau (Figure 5-4).

Using available earthquakes from the ISC, a total of 26 events are reported at depths between ~30-68 km, with epicenters between 5.69°-5.79°N (Figure 5-4). Although some hypocenters might be mislocated, it is very interesting how they seem to cluster within the location of the slow anomaly (Figure 5-4). Assuming that some of these earthquakes are well located, they might be suggesting some deformation or metamorphic reactions (Sippl et al., 2013) within a crustal fragment (slow anomaly).

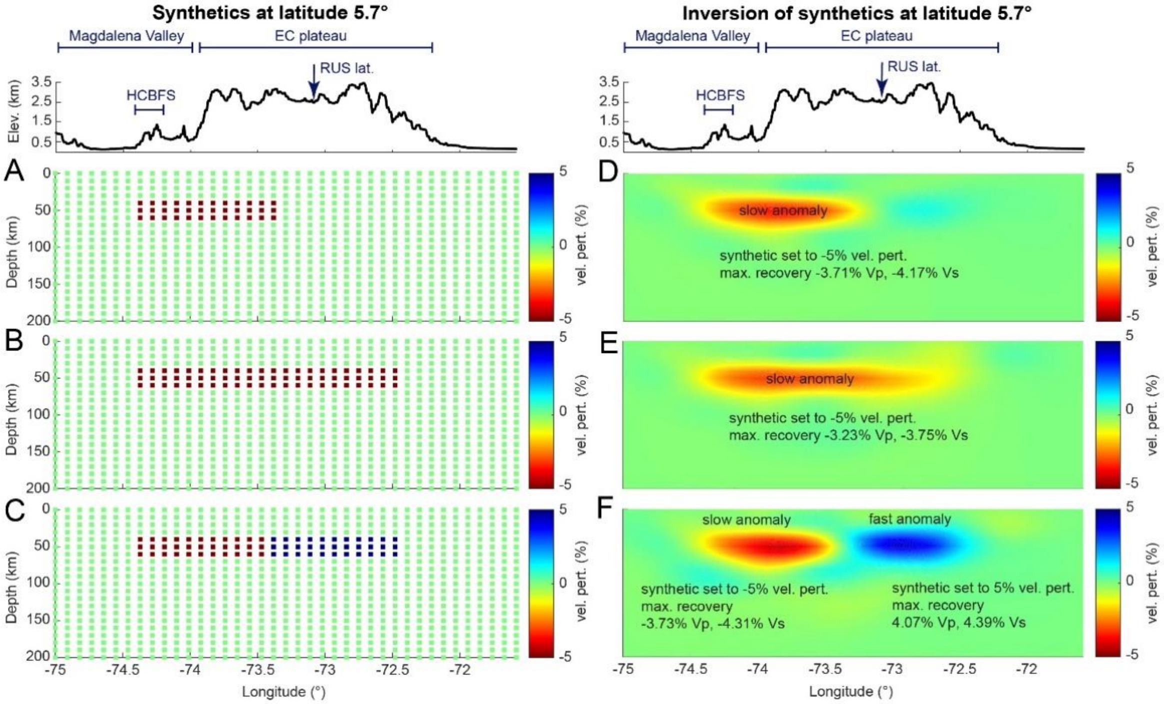

Figure 5-5. Synthetic tests: recovery of prismatic geometries. (A-C) Synthetic geometry based on velocity perturbation at different nodes. (D-F) Recovery of the synthetic geometries after inversion. For the description of the synthetic geometries see sub-section 5.3.3. Maximum recoveries are expressed as percentages related to the inversion: for instance, a -4.10% max. recovery with respect to a -5% velocity perturbation, represents a relative 82% retrieval of the considered velocity anomaly.

Regarding the extension of the anomaly, synthetic tests support a restricted extent beneath the abrupt change in topography defining the transition between the Magdalena Valley and the western flank of the EC plateau (Figures 5-4 and 5-5). Additionally, the tomographic image shows a shallowing pattern of slow velocities towards the east, at longitudes below the RUS station (Figure 5-4). I interpret these features as a crustal fragment that is spatially restricted beneath the transition between the Magdalena Valley and the EC, rather than representing a larger anomaly across the entire orogenic plateau.

Along the discussed latitude (~5.7°N), inversion of gravity data to recover Moho depths (chapter 2), is consistent with the spatial restriction and crustal materials representing the slow anomaly. Gravity inversion shows a deeper Moho (50-53 ± 4 km) where the slow anomaly is imaged, and in agreement with the tomographic suggestion of a shallowing pattern towards the east (magenta line in Figure 5-8). Additionally, regional-scale interpolation of crustal thickness contours, using receiver function constraints, also supports a thicker crust at the transition between the Magdalena Valley and the EC, and a thinning pattern towards the east (Figure 5-1; Poveda et al., 2018, 2015).

Regarding the upper crustal structure above the slow anomaly, the Honda-Cambao-Bituima fault system (HCBFS in Figures 5-4, 5-5, and 5-8) represents a west-verging thrusting system that has accommodated up to 40 km of shortening (e.g. Cortés et al., 2006). Structural analysis and cross-section restorations along the western flank of the EC have suggested a westward thrusting of the EC plateau above the basement beneath the Magdalena Valley (Cortés et al., 2006; Cortés and Angelier, 2005; Mora et al., 2013; Sánchez et al., 2012). Under this scenario, the crust beneath the Magdalena Valley and the Central Cordillera have likely been involved in the deformation style, defining an eastward underthrusting that has been referred to as intra-continental subduction (Cortés et al., 2006 and references therein).

A similar interpretation has been made along the Chilean Andes, for which Armijo et al. (2010) propose an eastward underthrusting (referred to as embryonic intra-continental subduction) of the Marginal block beneath the Principal Cordillera and the foreland region (see also Riesner et al., 2018). This deformation mechanism proposes thickening of the crust within the underthrusting domain, an abrupt change in topography (steep slopes), and a west-verging deformation style within the upper crust (Armijo et al., 2010; Riesner et al., 2018b).

I consider that such a mechanism is consistent with the interpretation and on-surface observations of (1) a spatially restricted crustal fragment beneath the transition between the Magdalena Valley and the western flank of the EC plateau; (2) a deeper Moho at the location of the imaged anomaly (magenta line in Figure 5-8; chapter 2); (3) the abrupt change in topography passing from heights less than 1.5 km at the Magdalena Valley to up to 2.8-3.2 km at the western EC plateau (see Figure 5-8); and (4) the west-verging structures of the Honda-Cambao-Bituima fault system (Cortés et al., 2006). Thus, I interpret the tectonic scenario as linked to the eastward underthrusting of the crust below the Magdalena Valley, underneath the northwestern EC plateau (Figure 5-8).

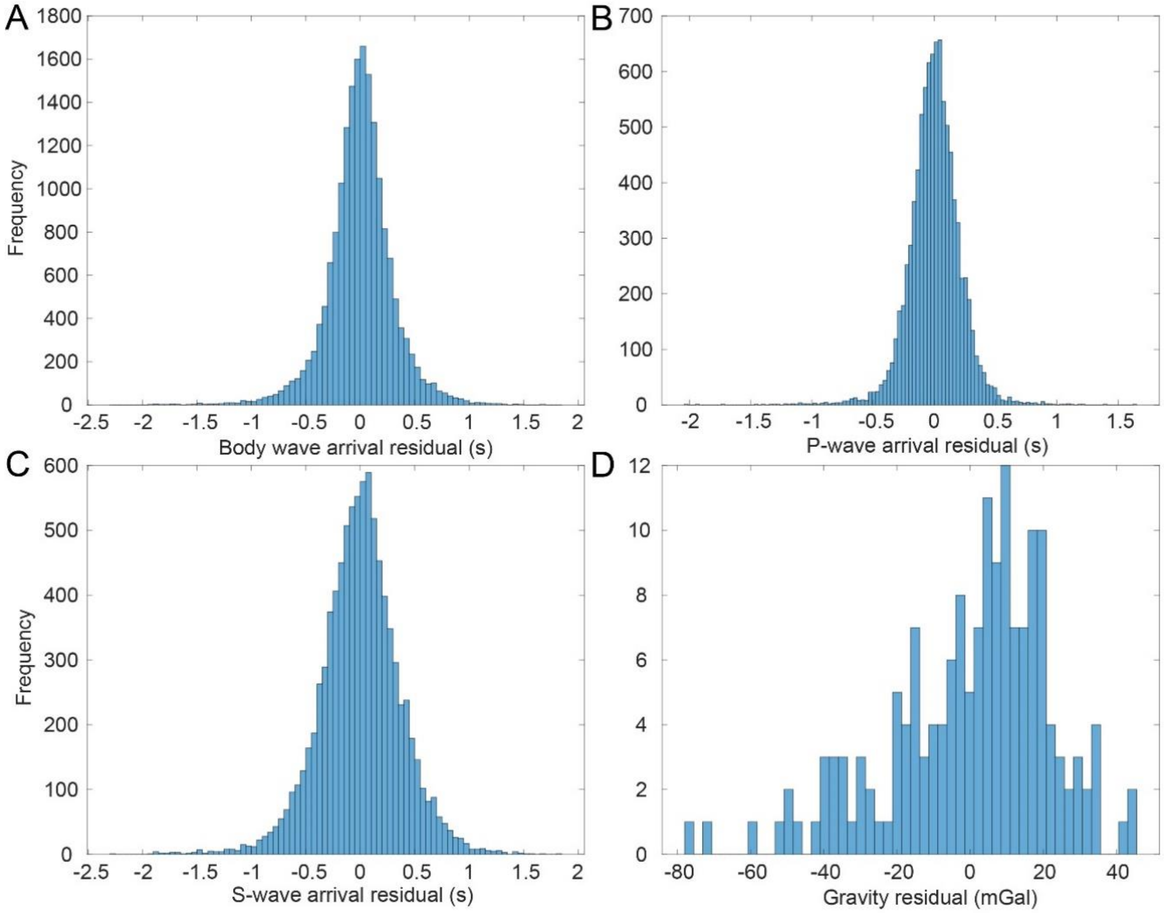

Figure 5-6. Residuals related to arrival times for body waves (A-C) and gravity (D) associated with the final inversion shown in Figure 5-4. Body wave residuals include both, P- and S-wave data as in Figure 5-3. See text for discussion.

5.4.2 Magmatic underplating beneath the northern EC

As previously mentioned, a high-velocity layer at ~36 km depth beneath the RUS station has been inferred from receiver functions (Monsalve et al., 2019). These authors characterized the layer as a high-velocity feature with respect to crustal velocities. In the tomographic inversion, I observed slow speeds beneath this station at similar depths, yet the retrieved values are in reference to mantle velocities (Figures 5-2 and 5-4). Therefore, slow speeds with respect to mantle velocities (tomography) are consistent with fast speeds with respect to crustal velocities (receiver functions), as previously documented (Monsalve et al., 2019). In fact, the inversion suggests at a depth of ~30-40 km beneath the RUS station, velocities between 7.1-7.3 km/s (Vp) and 4.0-4.1 km/s (Vs), which are similar to previous estimates of ~7.1 km/s (Vp) and ~4.1 km/s (Vs) based on receiver functions (Monsalve et al., 2019).

The retrieved velocities at the base of the crust beneath RUS are consistent with the properties of mafic granulites (Huang et al., 2013; Wang et al., 2013), yet, such a nature will fail to explain the presence of Mio-Pleistocene volcanism close to the station (Figure 5-1; Bernet et al., 2016; Monsalve et al., 2019). Moreover, as suggested by receiver functions, such a layer seems not to be anisotropic (Monsalve et al., 2019), which one might expect when considering a metamorphic origin for the lowermost crust. Finally, the inversion depicts the slow speeds beneath the RUS station latitudinally restricted between 5.3°-6.2°N, which is easier to reconcile with magmatic addition to the base of the crust. Hence, I support the idea of mafic melt ponding associated with magmatic underplating, as previously suggested, beneath the RUS station (Figure 5-8; Monsalve et al., 2019).

5.4.3 Hypotheses for the fast anomaly

Along the tomographic profile, a second anomaly between 72.4°-73.1°W is observed at depths of 40-70 km (Figure 5-4). Similar to the test done for the slow anomaly, the synthetics showed that a fast velocity body placed at 40-60 km is recovered as a thicker anomaly down to ~75 km (Figure 5-5). Therefore, I suggest that the fast anomaly represents a body lying between 40 and 60 km.

In that sense, the anomaly shows faster speeds with respect to the reference velocity model up to 2.9% in P-wave, up to 4.6% in S-wave, and lower Vp/Vs ratios up to -1.7% (Figure 5-4). These values indicate that the lowering of the Vp/Vs ratio is linked to a higher increase (positive perturbation) in the S-wave speed, compared to the P-wave, with respect to the reference velocity model (Figure 5-2). If correct, this relationship points to a compositional controlling factor (Hacker and Abers, 2012; Lee, 2003).

I consider that this anomaly can be related to a metasomatic process in the mantle wedge, in which orthopyroxene enrichment can explain the changes in Vs and Vp/Vs (e.g. Wagner et al., 2008). An increase in orthopyroxene content can be accomplished by the interaction between mafic magmas and the mantle wedge peridotite (Wang et al., 2021), or by silica influx associated with a flat subduction structure (Wagner et al., 2008, 2005).

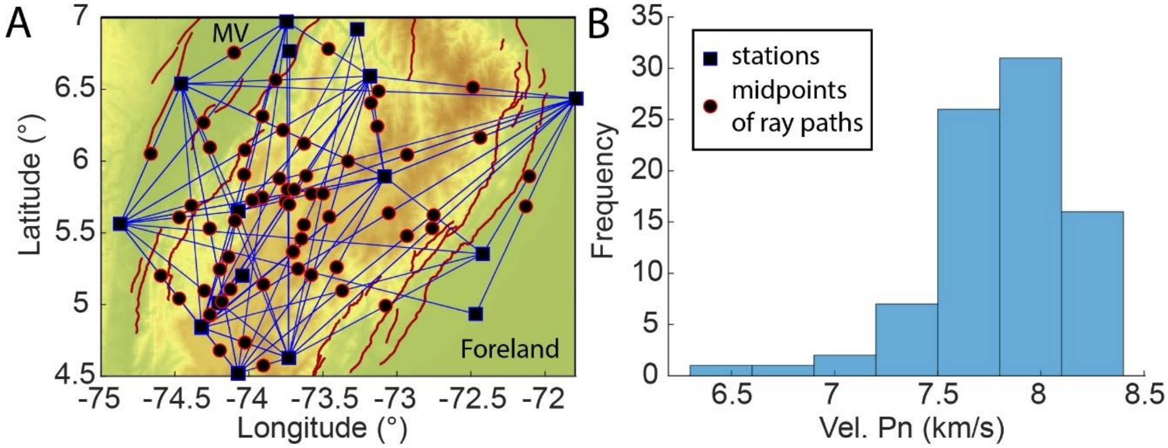

Figure 5-7. Pn-wave speed estimates beneath the northern EC. (A) ray paths between station pairs. MV: Magdalena Valley. (B) histogram with estimates of Pn velocity. An average Pn speed between 7.8-8.2 km/s is considered as representative for the study region.

I think that the first scenario (magma interaction) is consistent with the magmatic underplating model beneath the RUS station, which is located just to the west of the fast anomaly, and the presence of Mio-Pleistocene volcanism on the surface (Bernet et al., 2016; Monsalve et al., 2019). Thus, I consider this possibility the most feasible interpretation for the fast anomaly (Figure 5-8A).

The second scenario, where mantle metasomatism is associated with flat subduction, can be considered a possibility, given the current shallow geometry of the subducting slab at this latitude (Chiarabba et al., 2015; Sun et al., 2022; Syracuse et al., 2016; Vargas, 2020; Wagner et al., 2017). However, the inflection point of such a structure, where the flattened structure becomes a steeper slab, seems to be further to the west in reference to the location of the fast anomaly. Thus, if the anomaly is related to this mechanism, it requires the inflection point to be further to the east during the past. Based on an analysis of the eastward migration of magmatism during the last 14 Ma, Wagner et al. (2017) have suggested flattened subduction in which just to the south of the discussed profile (~5.5°N) the slab was torn due to roll-back tectonics since ~4 Ma. Thereby, I do not reject the hypothesis of flattened subduction reaching the position of the fast anomaly during the Miocene (Figure 5-8B).

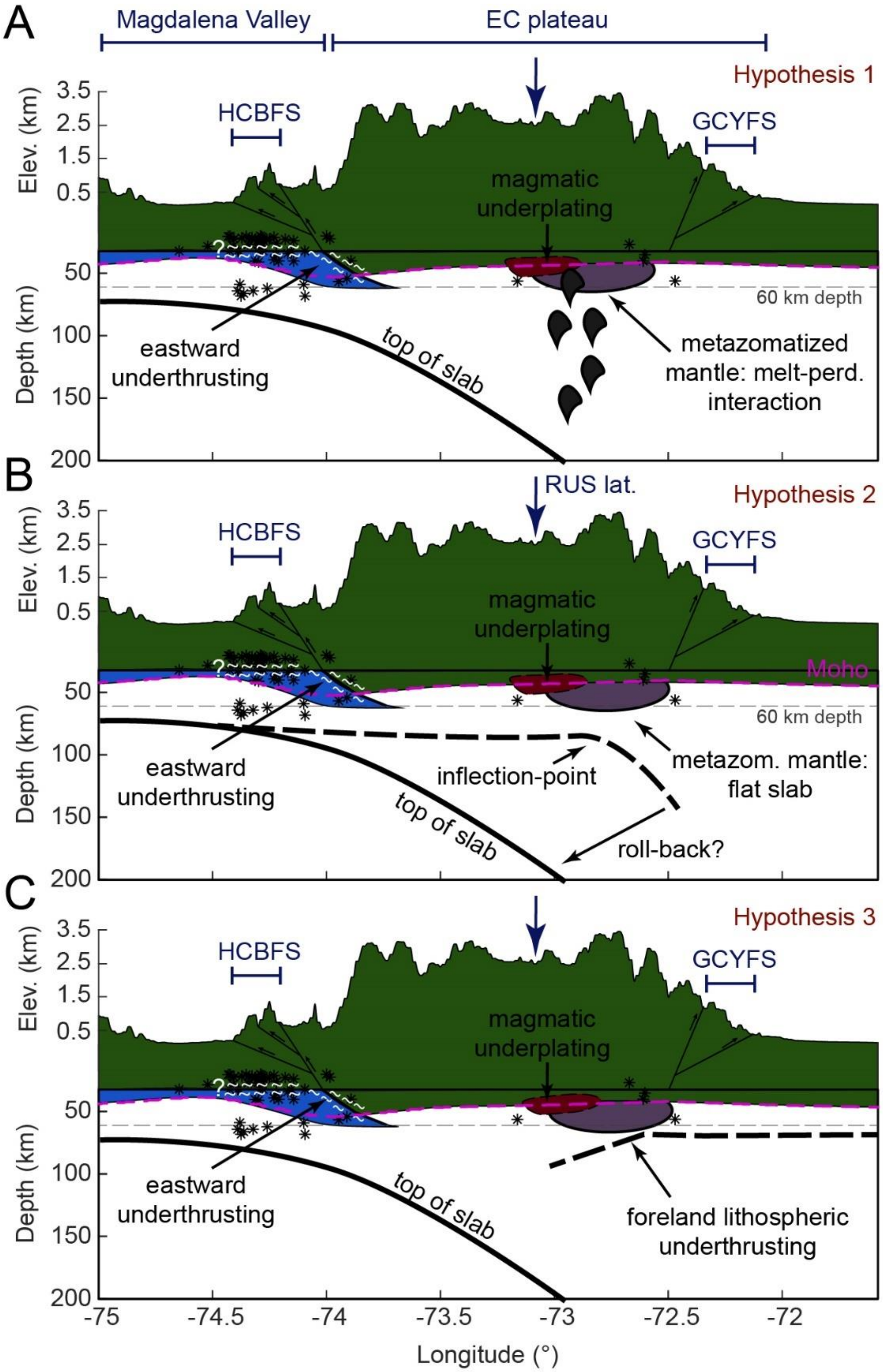

Figure 5-8. Interpretation of the identified anomalies. To the west, and associated with the slow anomaly, I interpret an eastward underthrusting of the crust beneath the Magdalena Valley and the northwestern EC plateau through the Honda-Cambao-Bituima fault system

(HCBFS). For the fast anomaly different hypotheses are proposed (see text for discussion). (A) Mantle metasomatism due to the interaction between mafic magmas and the mantle wedge peridotite (e.g. Wang et al., 2021). (B) Mantle metasomatism associated with a flat subduction setting (e.g. Wagner et al., 2008). (C) Westward underthrusting of the foreland lithosphere. Magenta dashed line represents the Moho depth derived from gravity inversion (chapter 2) showing a greater depth at the location of the slow anomaly and a shallowing pattern towards the east. The magmatic underplating shown beneath the RUS station (red polygon) is based on Monsalve et al. (2019) and consistent with our tomographic inversion. Top of the subducting plate after Hayes et al. (2018). Asterisks are earthquakes at depths of ~30-68 km.

In some instances, faster velocities beneath the transition between high-elevated plateaus and the foreland region have been interpreted as the underthrusting of the shield lithosphere beneath the plateau, as has been proposed in the Central Andes (Beck and Zandt, 2002; Sobolev et al., 2006; Ward et al., 2016). In those cases, the fast velocities are associated with the cold lithospheric mantle rather than crustal materials. Through numerical modeling, Vietor and Oncken (2005) have shown that the injection of crustal material to the base of the plateau, coming from an east-positioned foreland region, results in a topographic asymmetry of the plateau causing steep slopes at the western flank and smoother slopes at the eastern flank. Moreover, this type of deformation is consistent with a faster strain rate and higher shortening amounts along the eastern flank where the underthrusting takes place (Vietor and Oncken, 2005).

In our case, the only evidence I found for supporting this hypothesis, relies on the topographic asymmetry across the EC plateau, in which the slopes are much smoother at the eastern flank (Figure 5-8), and a higher amount of shortening and faster exhumation rates have been constrained to the east (Montes et al., 2019; Mora et al., 2015, 2008). Nevertheless, no major constraints on the deep crust and underlying mantle have been carried out to further support an underthrusting scenario. Consequently, although I do not neglect a possible underthrusting of the foreland lithosphere below the EC plateau to explain this anomaly (Figure 5-8C), I do not venture to favor this hypothesis with respect to the previous ones, given that the supporting evidence is too scarce.

In sum, I propose that the fast anomaly might be related to a metasomatic process in the mantle wedge, since it is a simpler explanation consistent with features like the presence of Mio-Pleistocene volcanism (Bernet et al., 2016; Monsalve et al., 2019) and the current flat slab structure (Vargas, 2020; Wagner et al., 2017). This metasomatism, therefore, might be explained as associated with mafic magma interaction, or silica influx during past flat subduction further to the east (Figure 5-8).

5.5 Conclusions

I have conducted a joint tomographic inversion beneath the northern EC plateau, which includes arrival times from recorded P- and S-wave phases associated with local earthquakes, and total Bouguer anomaly data. The inversion along the latitudinal profile with the highest resolution (~5.7°N) suggests the presence of two anomalies located at different longitudes yet at similar depths of 40-60 km. A slow anomaly is placed at the transition between the Magdalena Valley and the western EC plateau, interpreted as representing crustal materials that are eastwardly underthrusting beneath the northwestern EC. This process is thought to be prompting the abrupt change in topography between the Magdalena Valley and the orogenic plateau. On the other hand, a fast anomaly lies beneath the eastern flank of the EC plateau, for which I favor a metasomatic process within the mantle wedge. The metasomatism might be related to mafic magma interaction with the mantle peridotite or silica influx during past flat subduction further to the east.

5.6 Publication or submission

The paper associated with this chapter is in preparation.

5.7 Acknowledgments

Thanks to G. Posada and S. Roecker for their guidance in using the code and improving the tomographic inversion.

6. Summary and integrated conclusions

In this section, I summarized the most important findings from this thesis, which I think represent a significant contribution to the understanding of ongoing processes affecting the Moho vicinity in the northwestern Andes. From the integration of the entire work, I consider the following observations to be the most important findings:

- Two main regions with latitudinal variation in Moho depth are constrained along the Northern Andes: (1) the modern magmatic arc, showing a thickening pattern towards the south, and (2) the central-northern Eastern Cordillera, showing a thinning pattern towards the north.

- For the modern arc domain, gravity inversion, receiver functions, and xenolith constraints, point towards a thicker crust than previously thought, especially to the south of 2°N. The thickest part is feasible $\geq$70 km, something likely to be achieved in continental arcs.

- The thick expression of the arc domain is related to the accumulation of high-pressure garnet pyroxenites (arclogites), triggering a very fast and dense deep crust. For the southern section (south of 2°N), contributions to thicker anomalies of short wavelengths are linked to the interaction with the Carnegie ridge, a mechanism thought to drive deep crustal flow.

- The uppermost mantle beneath the modern arc exposes a well-defined anisotropic pattern. The fast-axis shows a NE-SW trend, consistent with the plate motion in such domain. The nature of the anisotropy is thought to be controlled by mineral alignment in which not only olivine, but also pyroxene, are contributing to the fabric.

- The uppermost mantle beneath the modern arc shows a variation in seismic speeds that seems to be related to a variation in the thermal state. The northern region (north of 4°N) shows the slowest speeds and warmest conditions, which might be influenced by the

Caldas tear and a possible hot buoyant asthenosphere influx. The fastest speeds and colder domain to the south (south of 2°N) seem to be affected by the interaction with the Carnegie ridge, prompting relatively shallow subduction.

- Compositional modeling of the uppermost mantle beneath the modern arc suggests a major role of pyroxene, which together with documented mantle xenoliths, supports the idea of a garnet websterite layer underlying the arc. Pn and Sn waves are thought to be traveling through this layer. From feasible amphibole contents, the websterite layer is hydrated rather than dry.

- For the northern Eastern Cordillera, the western flank of the orogenic plateau is being affected by an eastwardly underthrusting of the basement beneath the Magdalena Valley. This process is creating an abrupt change in topography, characterized by steep slopes with respect to the eastern flank of the cordillera, contributing to some degree to the asymmetry of the plateau.

- The upper crustal deformation, in terms of the amount of shortening and the western vergence of the thrusting faults along the western flank of the plateau, is consistent with an eastward underthrusting mechanism. A deeper expression of the Moho that spatially corresponds with the abrupt change in topography between the Magdalena Valley and the Eastern Cordillera plateau, supports as well the proposed underthrusting.

- Beneath the central part of the plateau, magmatic additions to the base of the crust are further supported, evidencing the occurrence of metasomatism in the mantle wedge. This is possibly the result of an interaction between magmatism pounded within the Moho vicinity and the mantle peridotite. This makes the magmatic underplating mechanism an important process in building the Eastern Cordillera plateau, not only by the interaction with the crust but also by affecting the underlying mantle. Although the metasomatic process could be associated with silica influx as well, it requires past flat subduction further to the east.

- Although the latitudinal extension of the eastward underthrusting and the magmatic underplating remains poorly constrained, this research opens the questions about the implications of these mechanisms working together to generate residual topography along the northern Eastern Cordillera plateau.

This thesis shows how a heterogenous Moho vicinity along an Andean-type orogen should be expected, encouraging further research on this topic. My work shows how this type of orogens can be contemporaneously being affected by magmatic additions to the base of the crust, not only below a well-developed arc, but also below orogenic plateaus with limited surface volcanic expressions. Furthermore, it shows how the uppermost mantle deformation (anisotropy) might be influenced by plate motion, ridge-margin interactions, and slab tears, creating latitudinal dissimilarities. Finally, it also shows how intra-continental underthrusting is playing an important role in the deformation of the lower crust along the flanks of an orogenic plateau. I hope this dissertation promotes further research on processes that were not addressed here, but certainly are affecting the crust-mantle transition in other regions of the Northwestern Andes.

What I think is important to mention as a concluding remark, is that I believe there is a connection between the inherited structure of the northwestern Andes, and the current processes affecting the Moho vicinity. For example, I believe that the inherited faulting of the North Andean belt, which controls the strike-slip tectonics within the magmatic arc domain, is an important contributor to the observed anisotropy of the underlying mantle. As another example, I also believe that the underthrusting in the western flank of the Eastern Cordillera is enhanced by inherited structures and rheological weaknesses that might reach deeper levels in the middle-lower crust.

Therefore, trying to answer the question of how these inherited structures such as regional-scale faults, slab geometries, or lithospheric weaknesses between docked blocks, are prompting processes such as mantle anisotropy, lower crustal flow, magmatic underplating, or intra-continental underthrusting (processes interpreted in this thesis), is the following step of my research.

References

Abers, G.A., Hacker, B.R., 2016. A MATLAB toolbox and Excel workbook for calculating the densities, seismic wave speeds, and major element composition of minerals and rocks at pressure and temperature. Geochemistry, Geophys. Geosystems 17, 616–624. https://doi.org/10.1002/2015GC006171

Abratis, M., Wörner, G., 2001. Ridge collision, slab-window formation, and the flux of Pacific asthenosphere into the Caribbean realm. Geology 29, 127–130. https://doi.org/10.1130/0091-7613

Afonso, J.C., Schutt, D.L., 2012. The effects of polybaric partial melting on density and seismic velocities of mantle restites. Lithos 134–135, 289–303. https://doi.org/10.1016/j.lithos.2012.01.009

Aitken, A.R.A., Salmon, M.L., Kennett, B.L.N., 2013. Australia's Moho: A test of the usefulness of gravity modelling for the determination of Moho depth. Tectonophysics 609, 468–479. https://doi.org/10.1016/j.tecto.2012.06.049

Amante, C., Eakins, B.W., 2009. ETOPO1 1 Arc-Minute Global Relief Model: Procedures, Data Sources and Analysis. NOAA Tech. Memo. NESDIS NGDC-24 19. https://doi.org/10.1594/PANGAEA.769615

Ammon, C.J., Randall, G.E., Zandt, G., 1990. On the Nonuniqueness of Receiver Function Inversions. J. Geophys. Res. 95. https://doi.org/10.1029/jb095ib10p15303

Anderson, D.L., 2005. Large Igneous Provinces, Delamination, and Fertile Mantle. Elements 1, 271–275. https://doi.org/10.2113/gselements.1.5.271

Armijo, R., Rauld, R., Thiele, R., Vargas, G., Campos, J., Lacassin, R., Kausel, E., 2010. The West Andean Thrust, the San Ramón Fault, and the seismic hazard for Santiago, Chile. Tectonics 29. https://doi.org/10.1029/2008tc002427

Avellaneda-Jiménez, D.S., Monsalve, G., León, S., Gómez-García, A.M., 2022. Insights into Moho depth beneath the northwestern Andean region from gravity data inversion. Geophys. J. Int. 229, 1964–1977. https://doi.org/https://doi.org/10.1093/gji/ggac041

Barthelmes, F., 2009. Definition of functionals of the geopotential and their calculation from spherical harmonic models: theory and formulas used by the calculation service of the International Centre for Global Earth Models (ICGEM). Dtsch. Geo-ForschungsZentrum GFZ 1–5. https://doi.org/10.2312/GFZ.b103-0902-26

Baumont, D., Paul, A., Zandt, G., Beck, S.L., Pedersen, H., 2002. Lithospheric structure of the central Andes based on surface wave dispersion. J. Geophys. Res. Solid Earth 107, ESE 18-1-ESE 18-13. https://doi.org/10.1029/2001jb000345

Bayona, G., Cortés, M., Jaramillo, C., Ojeda, G., Aristizabal, J.J., Reyes-Harker, A., 2008. An integrated analysis of an orogen-sedimentary basin pair: Latest Cretaceous-Cenozoic evolution of the linked Eastern Cordillera orogen and the Llanos foreland basin of Colombia. Bull. Geol. Soc. Am. 120, 1171–1197. https://doi.org/10.1130/B26187.1

Beck, S.L., Zandt, G., 2002. The nature of orogenic crust in the central Andes. J. Geophys. Res. Solid Earth 107, ESE 7-1-ESE 7-16. https://doi.org/10.1029/2000jb000124

Beghoul, N., Barazangi, M., 1989. Mapping high Pn velocity beneath the Colorado Plateau constrains uplift models. J. Geophys. Res. 94, 7083–7104. https://doi.org/10.1029/JB094iB06p07083

Bernal-Olaya, R., Mann, P., Vargas, C.A., 2015. Earthquake, tomographic, seismic reflection, and gravity evidence for a shallowly dipping subduction zone beneath the caribbean margin of Northwestern Colombia. AAPG Mem. 108, 247–269. https://doi.org/10.1306/13531939M1083642

Bernard, R.E., Schulte-Pelkum, V., Behr, W.M., 2021. The competing effects of olivine and orthopyroxene CPO on seismic anisotropy. Tectonophysics 814, 228954. https://doi.org/10.1016/j.tecto.2021.228954

Bernet, M., Urueña, C., Amaya, S., Peña, M.L., 2016. New thermo and geochronological constraints on the Pliocene-Pleistocene eruption history of the Paipa-Iza volcanic complex, Eastern Cordillera, Colombia. J. Volcanol. Geotherm. Res. 327, 299–309. https://doi.org/10.1016/j.jvolgeores.2016.08.013

Bishop, B.T., Beck, S.L., Zandt, G., Wagner, L., Long, M., Antonijevic, S.K., Kumar, A., Tavera, H., 2017. Causes and consequences of flat-slab subduction in southern Peru. Geosphere 13, 1392–1407. https://doi.org/10.1130/GES01440.1

Blanco, J.F., Vargas, C.A., Monsalve, G., 2017. Lithospheric thickness estimation beneath Northwestern South America from an S-wave receiver function analysis. Geochemistry, Geophys. Geosystems 18, 1376–1387. https://doi.org/10.1002/2016GC006785

Bloch, E., Ibañez-Mejia, M., Murray, K., Vervoort, J., Müntener, O., 2017. Recent crustal foundering in the Northern Volcanic Zone of the Andean arc: Petrological insights from the roots of a modern subduction zone. Earth Planet. Sci. Lett. 476, 47–58. https://doi.org/10.1016/j.epsl.2017.07.041

Borrero, C.A., Castillo, H., 2006. Vulcanitas del S-SE de Colombia: Retro-arco alcalino y su posible relacion con una ventana astenosferica. Boletín Geol. 28, 23–34.

Bowman, E.E., Ducea, M.N., Triantafyllou, A., 2021. Arclogites in the subarc lower crust: effects of crystallization, partial melting, and retained melt on the foundering ability of residual roots. J. Petrol. https://doi.org/10.1093/petrology/egab094/6424248

Brocher, T.M., 2005. Empirical relations between elastic wavespeeds and density in the

Earth’s crust. Bull. Seismol. Soc. Am. 95, 2081–2092. https://doi.org/10.1785/0120050077

Cardona, A., León, S., Jaramillo, J.S., Montes, C., Valencia, V., Vanegas, J., Bustamante, C., Echeverri, S., 2018. The Paleogene arcs of the northern Andes of Colombia and Panama: Insights on plate kinematic implications from new and existing geochemical, geochronological and isotopic data. Tectonophysics 749, 88–103. https://doi.org/10.1016/j.tecto.2018.10.032

Cardona, A., Montes, C., Ayala, C., Bustamante, C., Hoyos, N., Montenegro, O., Ojeda, C., Niño, H., Ramirez, V., Valencia, V., Rincón, D., Vervoort, J., Zapata, S., 2012. From arc-continent collision to continuous convergence, clues from Paleogene conglomerates along the southern Caribbean-South America plate boundary. Tectonophysics 580, 58–87. https://doi.org/10.1016/j.tecto.2012.08.039

Case, J.E., Duran S, L.G., Alfonso, L.R., Moore, W.R., 1971. Tectonic investigations in western Colombia and eastern Panama. Bull. Geol. Soc. Am. 82, 2685–2712. https://doi.org/10.1130/0016-7606(1971)82[2685:TIIWCA]2.0.CO;2

Castellanos, J.C., Clayton, R.W., Pérez-Campos, X., 2018. Imaging the Eastern Trans-Mexican Volcanic Belt With Ambient Seismic Noise: Evidence for a Slab Tear. J. Geophys. Res. Solid Earth 123, 7741–7759. https://doi.org/10.1029/2018JB015783

Chiarabba, C., De Gori, P., Faccenna, C., Speranza, F., Seccia, D., Dionicio, V., Prieto, G.A., 2015. Subduction system and flat slab beneath the Eastern Cordillera of Colombia. Geochemistry Geophys. Geosystems 17, 16–27. https://doi.org/10.1002/2015GC006048

Chiaradia, M., Müntener, O., Beate, B., Fontignie, D., 2009. Adakite-like volcanism of Ecuador: Lower crust magmatic evolution and recycling. Contrib. to Mineral. Petrol. 158, 563–588. https://doi.org/10.1007/s00410-009-0397-2

Christensen, N.I., 2004. Serpentinites, peridotites, and seismology. Int. Geol. Rev. 46, 795–816. https://doi.org/10.2747/0020-6814.46.9.795

Clark, M.K., Bush, J.W.M., Royden, L.H., 2005. Dynamic topography produced by lower crustal flow against rheological strength heterogeneities bordering the Tibetan Plateau. Geophys. J. Int. 162, 575–590. https://doi.org/10.1111/j.1365-246X.2005.02580.x

Collins, J.A., Molnar, P., 2014. Pn anisotropy beneath the South Island of New Zealand and implications for distributed deformation in continental lithosphere. AGU J. Geophys. Res. Solid Earth 119, 7745–7767. https://doi.org/doi:10.1002/2014JB011233

Connolly, J.A.D., 2005. Computation of phase equilibria by linear programming: A tool for geodynamic modeling and its application to subduction zone decarbonation. Earth Planet. Sci. Lett. 236, 524–541. https://doi.org/10.1016/j.epsl.2005.04.033

Cook, F.A., White, D.J., Jones, A.G., Eaton, D.W.S., Hall, J., Clowes, R.M., 2010. How the crust meets the mantle: Lithoprobe perspectives on the mohorovičić discontinuity and crust-mantle transition. Can. J. Earth Sci. 47, 315–351. https://doi.org/10.1139/E09-076

Correa-Tamayo, A.M., Pulgarín-Alzate, B.A., Ancochea-Soto, E., 2020. The Nevado del Huila Volcanic Complex, in: Gómez, J., Pinilla-Pachon, A.O. (Eds.), The Geology of Colombia, Volume 4 Quaternary. Servicio Geológico Colombiano, Publicaciones Geológias Especiales 38, Bogotá, pp. 227–265. https://doi.org/https://doi.org/10.32685/pub.esp.38.2019.06

Cortés, M., Angelier, J., 2005. Current states of stress in the northern Andes as indicated by focal mechanisms of earthquakes. Tectonophysics 403, 29–58. https://doi.org/10.1016/j.tecto.2005.03.020

Cortés, M., Colletta, B., Angelier, J., 2006. Structure and tectonics of the central segment of the Eastern Cordillera of Colombia. J. South Am. Earth Sci. 21, 437–465. https://doi.org/10.1016/j.jsames.2006.07.004

Crotwell, H.P., Owens, T.J., Ritsema, J., 1999. The TauP Toolkit: Flexible Seismic Travel-time and Ray-path Utilities. Seismol. Res. Lett. 70, 154–160. https://doi.org/10.1785/gssrl.70.2.154

Currie, C.A., Ducea, M.N., DeCelles, P.G., Beaumont, C., 2015. Geodynamic models of Cordilleran orogens: Gravitational instability of magmatic arc roots. Mem. Geol. Soc. Am. 212, 1–22. https://doi.org/10.1130/2015.1212(01)

DeCelles, P.G., Zandt, G., Beck, S.L., Currie, C.A., Ducea, M.N., Kapp, P., Gehrels, G.E., Carrapa, B., Quade, J., Schoenbohm, L.M., 2015. Cyclical orogenic processes in the Cenozoic central Andes. Mem. Geol. Soc. Am. 212, 459–490. https://doi.org/10.1130/2015.1212(22)

Delph, J.R., Ward, K.M., Zandt, G., Ducea, M.N., Beck, S.L., 2017. Imaging a magma plumbing system from MASH zone to magma reservoir. Earth Planet. Sci. Lett. 457, 313–324. https://doi.org/10.1016/j.epsl.2016.10.008

Ducea, M.N., Chapman, A.D., Bowman, E., Balica, C., 2021a. Arclogites and their role in continental evolution; part 2: Relationship to batholiths and volcanoes, density and foundering, remelting and long-term storage in the mantle. Earth-Science Rev. 214. https://doi.org/10.1016/j.earscirev.2020.103476

Ducea, M.N., Chapman, A.D., Bowman, E., Triantafyllou, A., 2021b. Arclogites and their role in continental evolution; part 1: Background, locations, petrography, geochemistry, chronology and thermobarometry. Earth-Science Rev. 214. https://doi.org/10.1016/j.earscirev.2020.103375

Erdman, M.E., Lee, C.T.A., Levander, A., Jiang, H., 2016. Role of arc magmatism and lower crustal foundering in controlling elevation history of the Nevadaplano and Colorado Plateau: A case study of pyroxenitic lower crust from central Arizona, USA. Earth Planet. Sci. Lett. 439, 48–57. https://doi.org/10.1016/j.epsl.2016.01.032

Feng, M., An, M., Dong, S., 2017. Tectonic history of the Ordos Block and Qinling Orogen inferred from crustal thickness. Geophys. J. Int. 210, 303–320. https://doi.org/10.1093/gji/ggx163

Ferrari, L., Orozco-Esquivel, T., Manea, V., Manea, M., 2012. The dynamic history of the Trans-Mexican Volcanic Belt and the Mexico subduction zone. Tectonophysics 522–523, 122–149. https://doi.org/10.1016/j.tecto.2011.09.018

Fontaine, F.R., Tkalčić, H., Kennett, B.L.N., 2013. Imaging crustal structure variation across southeastern Australia. Tectonophysics 582, 112–125. https://doi.org/10.1016/j.tecto.2012.09.031

Förste, C., Bruinsma, S., Abrikosov, O., Lemoine, J.M., Marty, J.C., Flechtner, F., Balmino, G., Barthelmes, F., Biancale, R., 2014. EIGEN-6C4 The latest combined global gravity field model including GOCE data up to degree and order 2190 of GFZ Potsdam and GRGS Toulouse. GFZ Data Serv. https://doi.org/https://doi.org/10.5880/icgem.2015.1

Furlong, K.P., Fountain, D.M., 1986. Continental crustal underplating: Thermal considerations and seismic-petrologic consequences. J. Geophys. Res. 91, 8285. https://doi.org/10.1029/jb091ib08p08285

Gao, X., Sun, S., 2019. Comment on “3DINVER.M: A MATLAB program to invert the gravity anomaly over a 3D horizontal density interface by Parker-Oldenburg’s algorithm.” Comput. Geosci. 127, 133–137. https://doi.org/10.1016/j.cageo.2019.01.013

Gómez-García, A.M., Le Breton, E., Scheck-Wenderoth, M., Monsalve, G., Anikiev, D., 2021. The preserved plume of the Caribbean Large Igneous Plateau revealed by 3D data-integrative models. Solid Earth 12, 275–298. https://doi.org/10.5194/se-12-275-2021

Gómez-Ortiz, D., Agarwal, B.N.P., 2005. 3DINVER.M: A MATLAB program to invert the gravity anomaly over a 3D horizontal density interface by Parker-Oldenburg’s algorithm. Comput. Geosci. 31, 513–520. https://doi.org/10.1016/j.cageo.2004.11.004

Gómez-Ortiz, D., Tejero-López, R., Babín-Vich, R., Rivas-Ponce, A., 2005. Crustal density structure in the Spanish Central System derived from gravity data analysis (Central Spain). Tectonophysics 403, 131–149. https://doi.org/10.1016/j.tecto.2005.04.006

Graterol, V., Vargas, A., 2010. Mapa de anomalia de Bouguer total de la Republica de Colombia. ANH (Agencia Nac. Hidrocarburos Colomb. Bogota Magna/Colombia-Magna Bogota Zo. 1850000.

Green, E., Holland, T., Powell, R., 2007. An order-disorder model for omphacitic pyroxenes in the system jadeite-diopside-hedenbergite-acmite, with applications to eclogitic rocks. Am. Mineral. 92, 1181–1189. https://doi.org/10.2138/am.2007.2401

Green, E., White, R.W., Diener, J.F.A., Powell, R., Holland, T.J.B., Palin, R.M., 2016. Activity–composition relations for the calculation of partial melting equilibria in metabasic rocks. J. Metamorph. Geol. 34, 845–869. https://doi.org/10.1111/jmg.12211

Griffin, W.L., O'Reilly, S.Y., Afonso, J.C., Begg, G.C., 2009. The composition and evolution of lithospheric mantle: A re-evaluation and its tectonic implications. J. Petrol. 50, 1185–1204. https://doi.org/10.1093/petrology/egn033

Guerri, M., Cammarano, F., Connolly, J.A.D., 2015. Geochemistry, Geophysics, Geosystems. Geochemistry Geophys. Geosystems 18, 1541–1576. https://doi.org/10.1002/2015GC005746.Dynamics

Gutscher, M.A., Malavieille, J., Lallemand, S., Collot, J.Y., 1999. Tectonic segmentation of the North Andean margin: Impact of the Carnegie Ridge collision. Earth Planet. Sci. Lett. 168, 255–270. https://doi.org/10.1016/S0012-821X(99)00060-6

Gutscher, M.A., Maury, F., Eissen, J.P., Bourdon, E., 2000. Can slab melting be caused by flat subduction? Geology 28, 535–538. https://doi.org/10.1130/0091-7613

Hacker, B.R., Abers, G.A., 2012. Subduction Factory 5: Unusually low Poisson's ratios in subduction zones from elastic anisotropy of peridotite. J. Geophys. Res. Solid Earth 117, 1–15. https://doi.org/10.1029/2012JB009187

Hacker, B.R., Abers, G.A., Peacock, S.M., 2003. Subduction factory 1. Theoretical mineralogy, densities, seismic wave speeds, and H2O contents. J. Geophys. Res. Solid Earth 108, 1–26. https://doi.org/10.1029/2001jb001127

Hammond, J.O.S., Kendall, J.M., Wookey, J., Stuart, G.W., Keir, D., Ayele, A., 2014. Differentiating flow, melt, or fossil seismic anisotropy beneath Ethiopia. Geochemistry, Geophys. Geosystems 15, 1878–1894. https://doi.org/10.1002/2013GC005185

Hammond, W.C., Humphreys, E.D., 2000. Upper mantle seismic wave velocity: Effects of realistic partial melt geometries. J. Geophys. Res. Solid Earth 105, 10975–10986. https://doi.org/https://doi.org/10.1029/2000JB900041

Hayes, G.P., Moore, G.L., Portner, D.E., Hearne, M., Flamme, H., Furtney, M., Smoczyk, G.M., 2018. Slab2, a comprehensive subduction zone geometry model. Science (80- .). 362(6410), 58–61.

Herrmann, R.B., 2013. Computer programs in seismology: An evolving tool for instruction and research. Seismol. Res. Lett. 84, 1081–1088. https://doi.org/10.1785/0220110096

Hole, J.A., Zelt, B.C., 1995. 3-D finite-difference reflection traveltimes. Geophys. J. Int. 121, 427–434. https://doi.org/https://doi.org/10.1111/j.1365-246X.1995.tb05723.x

Holland, T.J.B., Powell, R., 2003. Activity-compositions relations for phases in petrological calculations: An asymetric multicomponent formulation. Contrib. to Mineral. Petrol. 145, 492–501. https://doi.org/10.1007/s00410-003-0464-z

Holland, T.J.B., Powell, R., 1998. An internally consistent thermodynamic data set for phases of petrological interest. J. Metamorph. Geol. 16, 309–343. https://doi.org/10.1111/j.1525-1314.1998.00140.x

Horton, B.K., Parra, M., Mora, A., 2020. Insights from the Sedimentary Record Chapter 3. Geol. Colomb. 3, 1–22.

Huang, Y., Chubakov, V., Mantovani, F., Rudnick, R.L., McDonough, W.F., 2013. A reference Earth model for the heat-producing elements and associated geoneutrino flux. Geochemistry, Geophys. Geosystems 14, 2003–2029. https://doi.org/10.1002/ggge.20129

Hyndman, R.D., Peacock, S.M., 2003. Serpentinization of the forearc mantle. Earth Planet. Sci. Lett. 212, 417–432. https://doi.org/10.1016/S0012-821X(03)00263-2

Idárraga-García, J., Kendall, J.M., Vargas, C.A., 2016. Shear wave anisotropy in northwestern South America and its link to the Caribbean and Nazca subduction geodynamics. Geochemistry Geophys. Geosystems 17, 3655–3673. https://doi.org/doi:10.1002/2016GC006323

Ince, E.S., Barthelmes, F., Reißland, S., Elger, K., Förste, C., Flechtner, F., Schuh, H., 2019. ICGEM - 15 years of successful collection and distribution of global gravitational models, associated services and future plans. Earth Syst. Sci. Data Discuss. 1–61. https://doi.org/10.5194/essd-2019-17

Jeffreys, H., Bullen, K.E., 1940. Seismological Tables, British Association for the Advancement of Science, London.

Jennings, E.S., Holland, T.J.B., 2015. A simple thermodynamic model for melting of peridotite in the system NCFMASOCr. J. Petrol. 56, 869–892. https://doi.org/10.1093/petrology/egv020

Jones, C.H., Reeg, H., Zandt, G., Gilbert, H., Owens, T.J., Stachnik, J., 2014. P-wave tomography of potential convective downwellings and their source regions, Sierra Nevada, California. Geosphere 10, 505–533. https://doi.org/10.1130/GES00961.1

Julià, J., Ammon, C.J., Herrmann, R.B., Correig, A.M., 2000. Joint inversion of receiver function and surface wave dispersion observations. Geophys. J. Int. 143, 99–112. https://doi.org/10.1046/j.1365-246X.2000.00217.x

Karabulut, H., Paul, A., Erg, T.A., Hatzfeld, D., Childs, D.M., Aktar, M., 2013. Long-wavelength undulations of the seismic Moho beneath the strongly stretched Western Anatolia 450–464. https://doi.org/10.1093/gji/ggt100

Kay, S.M., Mpodozis, C., Gardeweg, M., 2014. Magma sources and tectonic setting of Central Andean andesites (25.5-28°S) related to crustal thickening, forearc subduction erosion and delamination. Geol. Soc. Spec. Publ. 385, 303–334. https://doi.org/10.1144/SP385.11

Kellogg, J.N., Camelio, G.B.F., Mora-Páez, H., 2019. Cenozoic tectonic evolution of the North Andes with constraints from volcanic ages, seismic reflection, and satellite geodesy, Andean Tectonics. https://doi.org/10.1016/b978-0-12-816009-1.00006-x

Kennett, B.L.N., Engdahl, E.R., 1991. Traveltimes for global earthquake location and phase identification. Geophys. J. Int. 105, 429–465. https://doi.org/10.1111/j.1365-246X.1991.tb06724.x

Kennett, B.L.N., Engdahl, E.R., Buland, R., 1995. Constraints on seismic velocities in the

Earth from traveltimes. Geophys. J. Int. 122, 108–124. https://doi.org/10.1111/j.1365-246X.1995.tb03540.x

Koch, C.D., Delph, J., Beck, S.L., Lynner, C., Ruiz, M., Hernandez, S., Samaniego, P., Meltzer, A., Mothes, P., Hidalgo, S., 2021. Crustal thickness and magma storage beneath the Ecuadorian arc. J. South Am. Earth Sci. 110, 103331. https://doi.org/10.1016/j.jsames.2021.103331

Koulakov, I., 2009. Out-of-network events can be of great importance for improving results of local earthquake tomography. Bull. Seismol. Soc. Am. 99, 2556–2563. https://doi.org/10.1785/0120080365

Koulakov, I., Sobolev, S. V., Asch, G., 2006. P - And S-velocity images of the lithosphere-asthenosphere system in the Central Andes from local-source tomographic inversion. Geophys. J. Int. 167, 106–126. https://doi.org/10.1111/j.1365-246X.2006.02949.x

Larkin, S.P., Levander, A., Henstock, T.J., Pullammanappallil, S., 1997. the northern Basin and Range Is the Moho flat ? Seismic evidence for a rough crust-mantle interface beneath the northern Basin and Range 7613. https://doi.org/10.1130/0091-7613(1997)025<0451

Laske, G., Masters, G., Ma, Z., Pasyanos, M., 2013. Update on CRUST1.0 - A 1-degree Global Model of Earth’s Crust. EGU Gen. Assem. 2013 15, 2658.

Lee, C.. T.A., 2003. Compositional variation of density and seismic velocities in natural peridotites at STP conditions: Implications for seismic imaging of compositional heterogeneities in the upper mantle. J. Geophys. Res. Solid Earth 108. https://doi.org/10.1029/2003jb002413

Lee, C.T.A., 2014. Physics and Chemistry of Deep Continental Crust Recycling, 2nd ed, Treatise on Geochemistry: Second Edition. Elsevier Ltd. https://doi.org/10.1016/B978-0-08-095975-7.00314-4

Lee, C.T.A., Anderson, D.L., 2015. Continental crust formation at arcs, the arclogite “delamination” cycle, and one origin for fertile melting anomalies in the mantle. Sci. Bull. 60, 1141–1156. https://doi.org/10.1007/s11434-015-0828-6

Lee, C.T.A., Cheng, X., Horodyskyj, U., 2006. The development and refinement of continental arcs by primary basaltic magmatism, garnet pyroxenite accumulation, basaltic recharge and delamination: Insights from the Sierra Nevada, California. Contrib. to Mineral. Petrol. 151, 222–242. https://doi.org/10.1007/s00410-005-0056-1

León, S., Cardona, A., Parra, M., Sobel, E.R., Jaramillo, J.S., Glodny, J., Valencia, V.A., Chew, D., Montes, C., Posada, G., Monsalve, G., Pardo-Trujillo, A., 2018. Transition From Collisional to Subduction-Related Regimes: An Example From Neogene Panama-Nazca-South America Interactions. Tectonics 37, 119–139. https://doi.org/10.1002/2017TC004785

León, S., Monsalve, G., Bustamante, C., 2021. How Much Did the Colombian Andes Rise by the Collision of the Caribbean Oceanic Plateau? Geophys. Res. Lett. 48, 1–11. https://doi.org/10.1029/2021gl093362

Ligorría, J.P., Ammon, C.J., 1999. Iterative deconvolution and receiver-function estimation. Bull. Seismol. Soc. Am. 89, 1395–1400. https://doi.org/10.1785/bssa0890051395

Londoño, J.M., Bohorquez, O.P., Ospina, L.F., 2010. Tomografía Sísmica 3D Del Sector De Cúcuta, Colombia. Bol. Geol. 32, 107–124.

Londoño, J.M., Sudo, Y., 2003. Velocity structure and a seismic model for Nevado del Ruiz Volcano (Colombia). J. Volcanol. Geotherm. Res. 119, 61–87. https://doi.org/10.1016/S0377-0273(02)00306-2

Lonsdale, P., 2005. Creation of the Cocos and Nazca plates by fission of the Farallon plate. Tectonophysics 404, 237–264. https://doi.org/10.1016/j.tecto.2005.05.011

Mahan, K.H., Schulte-Pelkum, V., Blackburn, T.J., Bowring, S.A., Dudas, F.O., 2012. Seismic structure and lithospheric rheology from deep crustal xenoliths, central Montana, USA. Geochemistry, Geophys. Geosystems 13. https://doi.org/10.1029/2012GC004332

Mainprice, D., 2015. Seismic Anisotropy of the Deep Earth from a Mineral and Rock Physics Perspective, in: Schubert, G. (Ed.), Treatise on Geophysics. Oxford: Elsevier, pp. 487–538.

Manea, V.C., Manea, M., 2011. Flat-slab thermal structure and evolution beneath central Mexico. Pure Appl. Geophys. 168, 1475–1487. https://doi.org/10.1007/s00024-010-0207-9

Marín-Cerón, M.I., Leal-Mejía, H., Bernet, M., Mesa-García, J., 2019. Late Cenozoic to modern-day volcanism in the Northern Andes: A geochronological, petrographical, and geochemical review, Frontiers in Earth Sciences. https://doi.org/10.1007/978-3-319-76132-9_8

Marot, M., Monfret, T., Gerbault, M., Nolet, G., Ranalli, G., Pardo, M., 2014. Flat versus normal subduction zones: A comparison based on 3-D regional traveltime tomography and petrological modelling of central Chile and western Argentina (29°-35°S). Geophys. J. Int. 199, 1633–1654. https://doi.org/10.1093/gji/ggu355

McKenzie, D., Jackson, J., 2002. Conditions for flow in the continental crust. Tectonics 21, 5-1-5–7. https://doi.org/10.1029/2002tc001394

Meissnar, R.O., Flueh, E.R., Stibane, F., Berg, E., 1976. Dynamics of the active plate boundary in southwest colombia according to recent geophysical measurements. Tectonophysics 35, 115–136. https://doi.org/10.1016/0040-1951(76)90032-9

Monsalve-Bustamante, M.L., 2020. The volcanic front in Colombia: Segmentation and recent and historical activity, in: Gómez, J., Pinilla-Pachon, A.O. (Eds.), The Geology of Colombia, Volume 4 Quaternary. Servicio Geológico Colombiano, Publicaciones Geológicas Especiales, Bogotá, pp. 97–159. https://doi.org/10.32685/pub.esp.38.2019.03

Monsalve-Bustamante, M.L., Gómez-Tapias, J., Núñez-Tello, A., 2020. Rear–arc small–

volume basaltic volcanism in Colombia: Monogenetic volcanic fields. The Geology of Colombia, Volume 4 Quaternary. Servicio Geológico Colombia- no, Publicaciones Geológicas Especiales, Bogotá. https://doi.org/https://doi.org/10.32685/pub.esp.38.2019.10

Monsalve, G., Jaramillo, J.S., Cardona, A., Schulte-Pelkum, V., Posada, G., Valencia, V., Poveda, E., 2019. Deep Crustal Faults, Shear Zones, and Magmatism in the Eastern Cordillera of Colombia: Growth of a Plateau From Teleseismic Receiver Function and Geochemical Mio-Pliocene Volcanism Constraints. J. Geophys. Res. Solid Earth 124, 9833–9851. https://doi.org/10.1029/2019JB017835

Monsalve, H., Pacheco, J.F., Vargas, C.A., Morales, Y.A., 2013. Crustal velocity structure beneath the western Andes of Colombian using receiver-function inversion. J. South Am. Earth Sci. 48, 106–122. https://doi.org/10.1016/j.jsames.2013.09.001

Monsalve, M.L., Correa-Tamayo, A.M., Arcila, M., Dixon, J., 2015. Firma Adakítica en los productos recientes de los volcanes Nevado del Huila y Puracé, Colombia. Boletín Geológico 23–40. https://doi.org/10.32685/0120-1425/boletingeo.43.2015.27

Montes, C., Rodriguez-Corcho, A.F., Bayona, G., Hoyos, N., Zapata, S., Cardona, A., 2019. Continental margin response to multiple arc-continent collisions: The northern Andes-Caribbean margin. Earth-Science Rev. 198, 102903. https://doi.org/10.1016/j.earscirev.2019.102903

Mooney, W.D., 2021. The Moho Discontinuity, 2nd ed, Encyclopedia of Geology. Elsevier Inc. https://doi.org/10.1016/b978-0-08-102908-4.00049-7

Mora-Páez, H., Kellogg, J.N., Frymueller, J.T., Mencin, D., Fernandes, R.M.S., Diederix, H., LaFemina, P., Cardona-Piedrahita, L., Lizarazo, S., Peláez-Gaviria, J.R., Díaz-Mila, F., Bohórquez-Orozco, O., Giraldo-Londoño, L., Corchuelo-Cuervo, Y., 2019. Crustal deformation in the northern Andes - A new GPS velocity field. J. South Am. Earth Sci. 89, 76–91. https://doi.org/10.1016/j.jsames.2018.11.002

Mora-Páez, H., Mencin, D.J., Molnar, P., Diederix, H., Cardona-Piedrahita, L., Peláez-Gaviria, J.R., Corchuelo-Cuervo, Y., 2016. GPS velocities and the construction of the Eastern Cordillera of the Colombian Andes. Geophys. Res. Lett. 43, 8407–8416. https://doi.org/10.1002/2016GL069795

Mora, A., Parra, M., Rodriguez Forero, G., Blanco, V., Moreno, N., Caballero, V., Stockli, D., Duddy, I., Ghorbal, B., 2015. What drives orogenic asymmetry in the northern Andes?: A case study from the apex of the northern Andean orocline. AAPG Mem. 108, 547–586. https://doi.org/10.1306/13531949M1083652

Mora, A., Parra, M., Strecker, M.R., Sobel, E.R., Hooghiemstra, H., Torres, V., Jaramillo, J. V., 2008. Climatic forcing of asymmetric orogenic evolution in the Eastern Cordillera of Colombia. Bull. Geol. Soc. Am. 120, 930–949. https://doi.org/10.1130/B26186.1

Mora, A., Reyes-Harker, A., Rodriguez, G., Tesón, E., Ramirez-Arias, J.C., Parra, M., Caballero, V., Mora, J.P., Quintero, I., Valencia, V., Ibañez, M., Horton, B.K., Stockli, D.F., 2013. Inversion tectonics under increasing rates of shortening and sedimentation: Cenozoic example from the Eastern Cordillera of Colombia. Geol.

Soc. Spec. Publ. 377, 411–442. https://doi.org/10.1144/SP377.6

Mora, A., Villagómez, D., Parra, M., Caballero, V.M., Spikings, R., Horton, B.K., Mora-Bohórquez, J.A., Ketcham, R.A., Arias-Martínez, J.P., 2020. Late Cretaceous to Cenozoic Uplift of the Northern Andes: Paleogeographic Implications, in: Gómez, J., Mateus-Zabala, D. (Eds.), The Geology of Colombia, Volume 3 Paleogene-Neogene. Servicio Geológico Colombiano, Publicaciones Geológias Especiales 37, Bogotá, pp. 89–121. https://doi.org/htpps://doi.org/10.32685/pub.exp.37.2019.04

Motaghi, K., Shabanian, E., Kalvandi, F., 2017. Underplating along the northern portion of the Zagros suture zone, Iran. Geophys. J. Int. 210, 375–389. https://doi.org/10.1093/gji/ggx168

Myers, S.C., Beck, S., Zandt, G., Wallace, T., 1998. Lithospheric-scale structure across the Bolivian Andes from tomographic images of velocity and attenuation for P and S waves. System 103, 21,233-21,252.

Ojeda, A., Havskov, J., 2001. Crustal structure and local seismicity in Colombia. J. Seismol. 5, 575–593. https://doi.org/10.1023/A:1012053206408

Oldenburg, D.W., 1974. The inversion and interpretation of gravity anomalies. Geophysics 39, 526–536.

Owens, T., Zandt, G., 1985. The response of the continental crust-Mantle boundary observed on broadband teleseismic receiver functions. Geophys. Res. Lett. 12, 705–708. https://doi.org/https://doi.org/10.1029/GL012i010p00705

Paige, C.C., Saunders, M.A., 1982. LSQR: An Algorithm for Sparse Linear Equations and Sparse Least Squares. ACM Trans. Math. Softw. 8, 43–71. https://doi.org/10.1145/355993.356000

Pardo-Trujillo, A., Cardona, A., Giraldo, A.S., León, S., Vallejo, D.F., Trejos-Tamayo, R., Plata, A., Ceballos, J., Echeverri, S., Barbosa-Espitia, A., Slattery, J., Salazar-Ríos, A., Botello, G.E., Celis, S.A., Osorio-Granada, E., Giraldo-Villegas, C.A., 2020. Sedimentary record of the Cretaceous–Paleocene arc–continent collision in the northwestern Colombian Andes: Insights from stratigraphic and provenance constraints. Sediment. Geol. 401, 105627. https://doi.org/10.1016/j.sedgeo.2020.105627

Parker, R.L., 1973. The Rapid Calculation of Potential Anomalies. Geophys. J. R. Astron. Soc. 31, 447–455. https://doi.org/10.1111/j.1365-246X.1973.tb06513.x

Parra, M., Mora, A., Lopez, C., Rojas, L.E., Horton, B.K., 2012. Detecting earliest shortening and deformation advance in thrust belt hinterlands: Example from the Colombian Andes. Geology 40, 175–178. https://doi.org/10.1130/G32519.1

Pavlis, N.K., Holmes, S.A., Kenyon, S.C., Factor, J.K., 2012. The development and evaluation of the Earth Gravitational Model 2008 (EGM2008). J. Geophys. Res. Solid Earth 117, 1–38. https://doi.org/10.1029/2011JB008916

Pedraza-Garcia, P., Vargas, C.A., Monsalve, H., 2007. Geometric model of the Nazca plate subduction in Southwest Colombia. Earth Sci. Res. J. 11, 118–131.

Pennington, W.D., 1981. Subduction of the Eastern Panama Basin and Seismotectonics of Northwestern South America 86, 10753–10770. https://doi.org/doi:10.1029/JB086iB11p10753

Porritt, R.W., Becker, T.W., Monsalve, G., 2014. Seismic anisotropy and slab dynamics from SKS splitting recorded in Colombia. Geophys. Res. Lett. 41, 8775–8783. https://doi.org/10.1002/2014GL061958

Poveda, E., 2013. Discontinuidades sísmicas en la litósfera bajo la zona andina y el occidente colombianos a partir de formas de onda de sismos distantes. Universidad Nacional de Colombia.

Poveda, E., Julià, J., Schimmel, M., Perez-Garcia, N., 2018. Upper and Middle Crustal Velocity Structure of the Colombian Andes From Ambient Noise Tomography: Investigating Subduction-Related Magmatism in the Overriding Plate. J. Geophys. Res. Solid Earth 123, 1459–1485. https://doi.org/10.1002/2017JB014688

Poveda, E., Monsalve, G., Vargas, C.A., 2015. Receiver functions and crustal structure of the northwestern Andean region, Colombia. J. Geophys. Res. Solid Earth 120, 2408–2425. https://doi.org/10.1002/2014JB011304

Prasanna, H.M.I., Chen, W., Iz, H.B., 2013. High resolution local Moho determination using gravity inversion: A case study in Sri Lanka. J. Asian Earth Sci. 74, 62–70. https://doi.org/10.1016/j.jseaes.2013.06.005

Reguzzoni, M., Sampietro, D., 2015. GEMMA: An Earth crustal model based on GOCE satellite data. Int. J. Appl. Earth Obs. Geoinf. 35, 31–43. https://doi.org/10.1016/j.jag.2014.04.002

Riesner, M., Lacassin, R., Simoes, M., Carrizo, D., Armijo, R., 2018a. Revisiting the Crustal Structure and Kinematics of the Central Andes at 33.5°S: Implications for the Mechanics of Andean Mountain Building. Tectonics 37, 1347–1375. https://doi.org/10.1002/2017TC004513

Riesner, M., Lacassin, R., Simoes, M., Carrizo, D., Armijo, R., 2018b. Revisiting the Crustal Structure and Kinematics of the Central Andes at 33.5°S: Implications for the Mechanics of Andean Mountain Building. Tectonics 37, 1347–1375. https://doi.org/10.1002/2017TC004513

Rodriguez-Vargas, A., Koester, E., Mallmann, G., Conceição, R. V., Kawashita, K., Weber, M.B.I., 2005. Mantle diversity beneath the Colombian Andes, Northern Volcanic Zone: Constraints from Sr and Nd isotopes. Lithos 82, 471–484. https://doi.org/10.1016/j.lithos.2004.09.027

Roecker, S., Ebinger, C., Tiberi, C., Mulibo, G., Ferdinand-Wambura, R., Mtelela, K., Kianji, G., Muzuka, A., Gautier, S., Albaric, J., Peyrat, S., 2017. Subsurface images of the Eastern Rift, Africa, from the joint inversion of body waves, surface waves and gravity: Investigating the role of fluids in early-stage continental rifting. Geophys. J. Int. 210, 931–950. https://doi.org/10.1093/gji/ggx220

Roecker, S., Thurber, C., Roberts, K., Powell, L., 2006. Refining the image of the San

Andreas Fault near Parkfield, California using a finite difference travel time computation technique. Tectonophysics 426, 189–205. https://doi.org/10.1016/j.tecto.2006.02.026

Rondenay, S., Montési, L.G.J., Abers, G.A., 2010. New geophysical insight into the origin of the Denali volcanic gap. Geophys. J. Int. 182, 613–630. https://doi.org/10.1111/j.1365-246X.2010.04659.x

Saeid, E., Bakioglu, K.B., Kellogg, J., Leier, A., Martinez, J.A., Guerrero, E., 2017. Garzón Massif basement tectonics: Structural control on evolution of petroleum systems in upper Magdalena and Putumayo basins, Colombia. Mar. Pet. Geol. 88, 381–401. https://doi.org/10.1016/j.marpetgeo.2017.08.035

Sahoo, S.D., Pal, S.K., 2021. Crustal structure and Moho topography of the southern part (18° S–25° S) of Central Indian Ridge using high-resolution EIGEN6C4 global gravity model data. Geo-Marine Lett. 41. https://doi.org/10.1007/s00367-020-00679-z

Sánchez, J., Horton, B.K., Tesón, E., Mora, A., Ketcham, R.A., Stockli, D.F., 2012. Kinematic evolution of Andean fold-thrust structures along the boundary between the Eastern Cordillera and Middle Magdalena Valley basin, Colombia. Tectonics 31, 1–24. https://doi.org/10.1029/2011TC003089

Sarmiento-Rojas, L.F., 2019. Cretaceous stratigraphy and paleo-facies maps of northwestern South America, Frontiers in Earth Sciences. https://doi.org/10.1007/978-3-319-76132-9_10

Schreiber, D., Lardeaux, J.M., Martelet, G., Courrioux, G., Guillen, A., 2010. 3-D modelling of Alpine Mohos in Southwestern Alps. Geophys. J. Int. 180, 961–975. https://doi.org/10.1111/j.1365-246X.2009.04486.x

Schulte-Pelkum, V., Mahan, K.H., 2014. Imaging Faults and Shear Zones Using Receiver Functions. Pure Appl. Geophys. 171, 2967–2991. https://doi.org/10.1007/s00024-014-0853-4

Schurr, B., Rietbrock, A., Asch, G., Kind, R., Oncken, O., 2006. Evidence for lithospheric detachment in the central Andes from local earthquake tomography. Tectonophysics 415, 203–223. https://doi.org/10.1016/j.tecto.2005.12.007

Shearer, P.M., 2009. Introduction to Seismology, 2nd ed. Cambridge University Press, New York.

Shi, Z., Gao, R., Li, W., Lu, Z., Li, H., 2020. Tectonophysics Cenozoic crustal-scale duplexing and flat Moho in southern Tibet: Evidence from reflection seismology. Tectonophysics 790, 228562. https://doi.org/10.1016/j.tecto.2020.228562

Sippl, C., Schurr, B., Tympel, J., Angiboust, S., Mechie, J., Yuan, X., Schneider, F.M., Sobolev, S. V., Ratschbacher, L., Haberland, C., 2013. Deep burial of Asian continental crust beneath the Pamir imaged with local earthquake tomography. Earth Planet. Sci. Lett. 384, 165–177. https://doi.org/10.1016/j.epsl.2013.10.013

Siravo, G., Faccenna, C., Gérault, M., Becker, T.W., Fellin, M.G., Herman, F., Molin, P.,

2019. Slab flattening and the rise of the Eastern Cordillera, Colombia. Earth Planet. Sci. Lett. 512, 100–110. https://doi.org/10.1016/j.epsl.2019.02.002

Siravo, G., Fellin, M.G., Faccenna, C., Bayona, G., Lucci, F., Molin, P., Maden, C., 2018a. Constraints on the Cenozoic Deformation of the Northern Eastern Cordillera, Colombia. Tectonics 37, 4311–4337. https://doi.org/10.1029/2018TC005162

Siravo, G., Fellin, M.G., Faccenna, C., Bayona, G., Lucci, F., Molin, P., Maden, C., 2018b. Constraints on the Cenozoic Deformation of the Northern Eastern Cordillera, Colombia. Tectonics 37, 4311–4337. https://doi.org/10.1029/2018TC005162

Siravo, G., Molin, P., Sembroni, A., Fellin, M.G., Faccenna, C., 2021. Tectonically driven drainage reorganization in the Eastern Cordillera, Colombia. Geomorphology 389, 107847. https://doi.org/10.1016/j.geomorph.2021.107847

Sjöberg, L.E., Bagherbandi, M., 2011. A method of estimating the Moho density contrast with a tentative application of EGM08 and CRUST2.0. Acta Geophys. 59, 502–525. https://doi.org/10.2478/s11600-011-0004-6

Sobolev, S. V., Babeyko, A.Y., 2005. What drives orogeny in the Andes? Geology 33, 617–620. https://doi.org/10.1130/G21557.1

Sobolev, S. V., Babeyko, A.Y., Koulakov, I., Oncken, O., 2006. Mechanism of the Andean Orogeny: Insight from Numerical Modeling, in: The Andes. Springer, Berlin, Heidelberg, pp. 513–535. https://doi.org/10.1007/978-3-540-48684-8_25

Spada, M., Bianchi, I., Kissling, E., Agostinetti, N.P., Wiemer, S., 2013. Combining controlled-source seismology and receiver function 1050–1068. https://doi.org/10.1093/gji/ggt148

Steffen, R., Strykowski, G., Lund, B., 2017. High-resolution Moho model for Greenland from EIGEN-6C4 gravity data. Tectonophysics 706–707, 206–220. https://doi.org/10.1016/j.tecto.2017.04.014

Storchak, D.A., Schweitzer, J., Bormann, P., 2003. The IASPEI standard seismic phase list. Seismol. Res. Lett. 74, 761–772. https://doi.org/10.1785/gssrl.74.6.761

Sun, M., Bezada, M.J., Cornthwaite, J., Prieto, G.A., Niu, F., Levander, A., 2022. Overlapping slabs: Untangling subduction in NW South America through finite-frequency teleseismic tomography. Earth Planet. Sci. Lett. 577, 117253. https://doi.org/10.1016/j.epsl.2021.117253

Syracuse, E.M., Maceira, M., Prieto, G.A., Zhang, H., Ammon, C.J., 2016. Multiple plates subducting beneath Colombia, as illuminated by seismicity and velocity from the joint inversion of seismic and gravity data. Earth Planet. Sci. Lett. 444, 139–149. https://doi.org/10.1016/j.epsl.2016.03.050

Tang, M., Lee, C.T.A., Chen, K., Erdman, M., Costin, G., Jiang, H., 2019. Nb/Ta systematics in arc magma differentiation and the role of arclogites in continent formation. Nat. Commun. 10. https://doi.org/10.1038/s41467-018-08198-3

Tesón, E., Mora, A., Silva, A., Namson, J., Teixell, A., Castellanos, J., Casallas, W., Julivert, M., Taylor, M., Ibáñez-Mejía, M., Valencia, V.A., 2013. Relationship of

Mesozoic graben development, stress, shortening magnitude, and structural style in the Eastern Cordillera of the Colombian Andes. Geol. Soc. Spec. Publ. 377, 257–283. https://doi.org/10.1144/SP377.10

Thybo, H., Artemieva, I.M., 2013. Moho and magmatic underplating in continental lithosphere. Tectonophysics 609, 605–619. https://doi.org/10.1016/j.tecto.2013.05.032

Tirel, C., Gueydan, F., Tiberi, C., Brun, J.P., 2004. Aegean crustal thickness inferred from gravity inversion. Geodynamical implications. Earth Planet. Sci. Lett. 228, 267–280. https://doi.org/10.1016/j.epsl.2004.10.023

Tkalčić, H., Chen, Y., Liu, R., Zhibin, H., Sun, L., Chan, W., 2011. Multistep modelling of teleseismic receiver functions combined with constraints from seismic tomography: Crustal structure beneath southeast China. Geophys. J. Int. 187, 303–326. https://doi.org/10.1111/j.1365-246X.2011.05132.x

Uieda, L., Barbosa, V.C.F., 2017. Fast nonlinear gravity inversion in spherical coordinates with application to the South American Moho. Geophys. J. Int. 208, 162–176. https://doi.org/10.1093/gji/ggw390

van der Meijde, M., Julià, J., Assumpção, M., 2013. Gravity derived Moho for South America. Tectonophysics 609, 456–467. https://doi.org/10.1016/j.tecto.2013.03.023

Vargas, C.A., 2020. Subduction Geometries in Northwestern South America. Geol. Colomb. Vol. 4 Quat. 4, 397–422.

Vargas, C.A., Mann, P., 2013. Tearing and breaking off of subducted slabs as the result of collision of the panama arc-indenter with Northwestern South America. Bull. Seismol. Soc. Am. 103, 2025–2046. https://doi.org/10.1785/0120120328

Vargas, C.A., Ochoa, L.H., Caneva, A., 2019. Estimation of the Thermal Structure Beneath the Volcanic Arc of the Northern Andes by Coda Wave Attenuation Tomography. Front. Earth Sci. 7, 1–13. https://doi.org/10.3389/feart.2019.00208

Vargas, C.A., Pujades, L., Caneva, A., 2012. Attenuation structure of the Galeras volcano, Colombia. Bol. Geol. 34, 149–161.

Vargas, C.A., Pujades, L.G., Montes, L., 2007. Seismic structure of South-Central Andes of Colombia by tomographic inversion. Geofis. Int. 46, 117–127. https://doi.org/10.22201/igeof.00167169p.2007.46.2.21

Vauchez, A., Tommasi, A., Mainprice, D., 2012. Faults (shear zones) in the Earth's mantle. Tectonophysics 558–559, 1–27. https://doi.org/10.1016/j.tecto.2012.06.006

Veloza, G., Styron, R., Taylor, M., 2012. Open-source archive of active faults for northwest South America. GSA Today 22, 4–10. https://doi.org/10.1130/GSAT-G156A.1

Vidale, J.E., 1990. Finite-difference calculation of traveltimes in three dimensions. Geophysics 55, 521–526. https://doi.org/10.1190/1.1442863

Vietor, T., Oncken, O., 2005. Controls on the shape and kinematics of the Central Andean plateau flanks: Insights from numerical modeling. Earth Planet. Sci. Lett. 236, 814–827. https://doi.org/10.1016/j.epsl.2005.06.004

Villagómez, D., Spikings, R., 2013. Thermochronology and tectonics of the Central and Western Cordilleras of Colombia: Early Cretaceous-Tertiary evolution of the Northern Andes. Lithos 160–161, 228–249. https://doi.org/10.1016/j.lithos.2012.12.008

Wagner, L.S., Anderson, M.L., Jackson, J.M., Beck, S.L., Zandt, G., 2008. Seismic evidence for orthopyroxene enrichment in the continental lithosphere. Geology 36, 935–938. https://doi.org/10.1130/G25108A.1

Wagner, L.S., Beck, S., Zandt, G., 2005. Upper mantle structure in the south central Chilean subduction zone (30° to 36°S). J. Geophys. Res. Solid Earth 110, 1–20. https://doi.org/10.1029/2004JB003238

Wagner, L.S., Jaramillo, J.S., Ramírez-Hoyos, L.F., Monsalve, G., Cardona, A., Becker, T.W., 2017. Transient slab flattening beneath Colombia. Geophys. Res. Lett. 44, 6616–6623. https://doi.org/10.1002/2017GL073981

Wang, C., Liang, Y., Xu, W., 2021. Formation of Amphibole-Bearing Peridotite and Amphibole-Bearing Pyroxenite Through Hydrous Melt-Peridotite Reaction and In Situ Crystallization: An Experimental Study. J. Geophys. Res. Solid Earth 126, 1–22. https://doi.org/10.1029/2020JB019382

Wang, Q., Bagdassarov, N., Ji, S., 2013. The Moho as a transition zone: A revisit from seismic and electrical properties of minerals and rocks. Tectonophysics 609, 395–422. https://doi.org/10.1016/j.tecto.2013.08.041

Ward, K.M., Zandt, G., Beck, S.L., Wagner, L.S., Tavera, H., 2016. Lithospheric structure beneath the northern Central Andean Plateau from the joint inversion of ambient noise and earthquake-generated surface waves. J. Geophys. Res. Solid Earth 121, 8217–8238. https://doi.org/10.1002/2016JB013237

Weber, M.B., 1998. The Mercaderes-Rio Mayo xenoliths, Colombia: their bearing on mantle and crustal processes in the Northern Andes PhD Thesis.

Weber, M.B., Tarney, J., Kempton, P.D., Kent, R.W., 2002. Crustal make-up of the Northern Andes: Evidence based on deep crustal xenolith suites, Mercaderes, SW Colombia. Tectonophysics 345, 49–82. https://doi.org/10.1016/S0040-1951(01)00206-2

White, R.W., Powell, R., Johnson, T.E., 2014. The effect of Mn on mineral stability in metapelites revisited: new a–x relations for manganese-bearing minerals. J. Metamorph. Geol. 32, 809–828. https://doi.org/10.1111/jmg.12

Whitman, D., 1994. Moho geometry beneath the eastern margin of the Andes, northwest Argentina, and its implications to the effective elastic thickness of the Andean foreland. J. Geophys. Res. 99, 15277–15289.

Xuan, S., Jin, S., Chen, Y., 2020. Determination of the isostatic and gravity Moho in the East China Sea and its implications. J. Asian Earth Sci. 187, 104098. https://doi.org/10.1016/j.jseaes.2019.104098

Yarce, J., Monsalve, G., Becker, T.W., Cardona, A., Poveda, E., Alvira, D., Ordoñez-Carmona, O., 2014. Seismological observations in Northwestern South America: Evidence for two subduction segments, contrasting crustal thicknesses and upper mantle flow. Tectonophysics 637, 57–67. https://doi.org/10.1016/j.tecto.2014.09.006

Ydri, A., Idres, M., Ouyed, M., Samai, S., 2020. Moho geometry beneath northern Algeria from gravity data inversion. J. African Earth Sci. 168, 103851. https://doi.org/10.1016/j.jafrearsci.2020.103851

Zandt, G., Gilbert, H., Owens, T.J., Ducea, M., Saleeby, J., Jones, C.H., 2004. Active foundering of a continental arc root beneath the southern Sierra Nevada in California. Nature 431, 41–46. https://doi.org/10.1038/nature02847